

**MODELLING OF AN IMPACT RESISTANT
NAVIGATION SYSTEM FOR GUN PROJECTILES
BASED ON LOW COST MEMS SENSORS**

A Thesis Submitted to
the Graduate School of
İzmir Institute of Technology
in Partial Fulfillment of the Requirements for the Degree of
MASTER OF SCIENCE
in Mechanical Engineering

by
Selahattin Can İNEL

May 2021
IZMIR

ACKNOWLEDGMENTS

I would like to thank my esteemed advisor Prof.Dr.Serhan ÖZDEMİR who led my studies by always welcoming me with understanding and patience during my thesis studies. I wish to extend my special thanks to Prof.Dr.Mustafa Güden and Mesut BAYHAN from the Dynamic Test and Modelling Laboratory for their collaboration in Hopkinson Bar experiments. I would also like to thank praiseworthy members of Artificial Intelligence and Design Lab for great cooperation.

Most especially I want to express my endless gratitude to my parents and my family, which have supported and encouraged me throughout my life.

ABSTRACT

MODELLING OF AN IMPACT RESISTANT NAVIGATION SYSTEM FOR GUN PROJECTILES BASED ON LOW COST MEMS SENSORS

In this thesis, guided projectiles are studied in three aspects: a navigation system design, CFD analysis of a guided projectile for low launch velocities and durability of electronic components under extreme firing conditions. During the thesis progress, MATLAB & Simulink, FlightGear and Ansys-Fluent software are used for simulations and 3D object modelling. Basic Finner Reference Projectile is chosen as a test bed for navigation simulation, since the dimensions and some of the flight parameters are already available as open source. However, a missile state-space model which is given by Raytheon is used for navigation simulations instead of a guided projectile model due to inaccessibility of some critical aerodynamic parameters for 6-DoF model.

Navigation system is designed using preset guidance methodology which uses built-in inertial sensors to correct the course for given targets which location are loaded prior to launching. CFD calculations of the Basic Finner Reference Projectile are conducted for low launching velocities to light the way for the aerodynamic conditions of non-explosive firing equipments such as catapults and airguns. Furthermore, the durability of common electronic components under extreme projectile firing conditions are visualized up to 20,000g and the functionality of regular off the shelf microcontrollers and sensors are tested using Hopkinson Bar test equipment. A navigation model simulation of a guided munition is created combining FlightGear and MATLAB & Simulink satisfying the given different criteria for pole placement method, LQR controller and observer design.

Keywords: Navigation, Guidance, Guided Projectile, High-g Force Durability, CFD Analysis.

ÖZET

DÜŞÜK MALİYETLİ MEMS SENSÖRLÜ TOP MERMİLERİ İÇİN DARBE DAYANIMLI NAVİGASYON SİSTEMİ MODELLEMESİ

Bu tez çalışması; güdümlü bir top mermisi için navigasyon sistemi tasarıımı, düşük fırlatma hızlarında CFD analizi ve elektronik devre elemanlarının şiddetli ateşleme koşulları altındaki dayanımları olmak üzere üç ana başlık altında toplanmıştır. Tez çalışmalarını süresince simülasyon ve 3 boyutlu modelleme için MATLAB & Simulink, FlightGear ve Ansys Fluent yazılımları kullanılmıştır. Temel Kanatçık Referans Mermisi, ölçülerinin ve bazı uçuş parametrelerinin açık kaynak olarak verilmiş olması nedeniyle navigasyon simülasyonu için test numunesi olarak seçilmiştir. Ancak son derece gelişmiş bir mühimmat olan güdümlü top mermilerinin 6 serbestlik dereceli model kapsamında kullanılması gerekliliği, bazı kritik aerodinamik parametrelere erişim imkanı olmaması nedeniyle uçuş parametreleri güdümlü top mermisine yakın olan Raytheon firması tarafından açık kaynak olarak sunulan bir güdümlü füzenin durum-uzay modeli, güdümlü top mermisi modeli yerine simülasyon için kullanılmıştır.

Navigasyon sistemi, ateşleme öncesinde mevkisi yüklenen hedeflere karşı rota düzeltmek amacıyla dahili ataletsel sensörlerin kullanıldığı önceden ayarlanmış güdüm metodolojisi kullanılarak tasarlanmıştır. Temel Kanatçık Referans Mermisinin CFD hesaplamaları, mancınik ve havalı tüfek gibi patlayıcı olmayan ateşleme ekipmanlarının aerodinamik koşullarına ışık tutması amacıyla düşük fırlatma hızları için yapıldı. Ayrıca, elektronik devre elemanlarının aşırı mermi ateşleme koşulları altında dayanıklılığı Hopkinson Bar test ekipmanı kullanılarak $20.000g$ 'ye kadar görselleştirildi ve mikrodenetleyicilerin ve sensörlerin işlevselliği test edildi. Güdümlü bir mühimmat için FlightGear ve MATLAB & Simulink'i birleştirerek, direk yerleştirme yöntemi, LQR kontrolör ve gözlemci tasarıımı için verilen farklı kriterleri karşılayan bir navigasyon model simülasyonu oluşturuldu.

Anahtar Kelimeler: Navigasyon, Güdüm, Güdümlü Mermiler, Yüksek-g Kuvveti Dayanıklılığı, CFD Analizi.

TABLE OF CONTENTS

| | |
|--|------|
| LIST OF FIGURES | viii |
| LIST OF TABLES | xii |
| LIST OF SYMBOLS | xii |
| LIST OF ABBREVIATIONS | xiv |
| CHAPTER 1. INTRODUCTION | 1 |
| 1.1. History of Guided Projectiles | 3 |
| 1.2. Ballistics | 5 |
| 1.3. Guidance..... | 7 |
| 1.3.1. Phases of Guidance | 7 |
| 1.3.2. Types of Guidance | 8 |
| 1.3.2.1. Guidance Systems that Use Man-Made Electromagnetic Devices..... | 8 |
| 1.3.2.2. Self-Contained Guidance Systems | 10 |
| 1.4. Navigation Methods | 11 |
| 1.4.1. Inertial Navigation (Dead Reckoning) | 12 |
| 1.4.2. Terrestrial Navigation | 12 |
| 1.4.3. Celestial Navigation..... | 12 |
| 1.4.4. Electronic Navigation | 13 |
| 1.4.5. Advantages and Drawbacks of Inertial Navigation | 13 |
| 1.5. Model Based Simulation | 15 |
| 1.6. CFD Analysis of Munitions..... | 16 |
| 1.7. High-g Ruggedization of Electronic Boards | 18 |
| CHAPTER 2. DYNAMIC ANALYSIS OF GUIDED PROJECTILES | 20 |
| 2.1. Reference Frames | 20 |
| 2.2. Forces and Moments | 21 |

| | | |
|--------------------|---|-----------|
| 2.2.1. | Longitudinal Forces and Moments | 21 |
| 2.2.2. | Lateral Forces and Moments..... | 24 |
| 2.2.3. | Six Degree of Freedom Equations of Motion..... | 26 |
| 2.2.3.1. | Earth Axis Position Equations | 27 |
| 2.2.3.2. | Body Axis Rotation Angle Equations | 28 |
| 2.2.3.3. | Body Axis Translational Velocity Equations | 29 |
| 2.2.3.4. | Body Axis Angular Velocity Equations | 31 |
| 2.3. | Control Input Combination | 33 |
| 2.4. | Summary of Six Degree of Freedom Equations of Motions | 34 |
| CHAPTER 3. | CONTROL SYSTEM DESIGN OF GUIDED PROJECTILES | 36 |
| 3.1. | State Space Model..... | 36 |
| 3.1.0.1. | Step Response of the Open-Loop Model | 38 |
| 3.2. | Navigation System Design..... | 39 |
| 3.2.1. | Controllability Analysis..... | 41 |
| 3.2.2. | Observability Analysis | 42 |
| 3.2.3. | Navigation System with Pole Placement Method | 43 |
| 3.2.4. | Navigation System with Linear Quadratic Regulator..... | 49 |
| 3.2.5. | Navigation System with Observer | 53 |
| 3.2.6. | Navigation System Simulation with FlightGear and Simulink.. | 57 |
| CHAPTER 4. | COMPUTATIONAL FLUID ANALYSIS OF REFERENCE MODEL | 60 |
| 4.1. | Geometry and Computational Domain | 61 |
| 4.2. | Theory | 62 |
| 4.3. | Meshing..... | 63 |
| 4.4. | Solutions and Results | 64 |
| CHAPTER 5. | SHOCK SURVIVABILITY CAPABILITY OF ELECTRONIC CIR- | |
| CUITS | 67 | |
| 5.1. | High-g Environment and Ruggedization | 67 |
| 5.2. | High-g Testing Methods | 70 |
| 5.2.1. | High-g Test of PCBs at Hopkinson Bar | 71 |

| | |
|---|------------|
| 5.2.1.1. Results of Hopkinson Bar Test and Discussion | 72 |
| CHAPTER 6. CASE STUDIES, SIMULATION AND EXPERIMENTS | 77 |
| 6.1. Inertial Navigation Car, Case Study-1..... | 77 |
| 6.2. Aircraft Autopilot Control System, Case Study-2 | 79 |
| 6.3. Analog-Digital Conversion (ADC), Case Study-3..... | 82 |
| 6.3.1. Cross-talk Between SDIO and ADC Channels | 85 |
| 6.3.2. Comparison of ADCs | 86 |
| CHAPTER 7. CONCLUSIONS | 93 |
| APPENDICES | |
| APPENDIX A. HIGH-G EXPERIMENT PCB PINOUTS AND SCHEMATIC | 95 |
| APPENDIX B. HOPKINSON BAR EXPERIMENT IMAGES | 97 |
| APPENDIX C. SIMULINK BLOCK DIAGRAM FOR AIRCRAFT AUTOPILOT CONTROL SYSTEM | 100 |
| APPENDIX D. CODE FOR LQR GAIN CALCULATION | 101 |
| APPENDIX E. COMBINED AERODYNAMIC COEFFICIENTS AND MOMENT OF INERTIA | 103 |
| APPENDIX F. HOPKINSON BAR EXPERIMENT VIDEOS AND SIMULA- TION SOFTWARE | 104 |
| REFERENCES | 106 |

LIST OF FIGURES

| <u>Figure</u> | <u>Page</u> |
|--|-------------|
| Figure 1.1 USS Mason and Strait of Bab El-Mandeb. | 2 |
| Figure 1.2 Examples of Guided Munitions. | 3 |
| Figure 1.3 Fin-Stabilized and Spin-Stabilized Guided Projectiles. | 4 |
| Figure 1.4 M1156 Course Correction Fuse (Source: Mönch Publishing Group (2021)) | 5 |
| Figure 1.5 Greek Ballista (Source: Farrar and Leeming (1983)) | 6 |
| Figure 1.6 Guidance Phases | 7 |
| Figure 1.7 Guidance System Categories (Source: Frieden (1985)) | 9 |
| Figure 1.8 Simple Beam-Rider Guidance System (Source: Frieden (1985)) | 10 |
| Figure 1.9 Illustration of Homing Guidance Types (Source: Frieden (1985)) | 10 |
| Figure 1.10 Displacement Measurement with MPU6050. | 15 |
| Figure 1.11 Example Model Based Simulation Block Diagrams. | 17 |
| Figure 1.12 Comparison of Turbulence Models (Source: (ANSYS, 2014). | 18 |
| Figure 1.13 Examples of High-G Ruggedization Methods (Source: Burd (1999)) ... | 19 |
| Figure 2.1 Earth, Body and Wind Frames. | 20 |
| Figure 2.2 TLongitudinal Forces and Moment. | 22 |
| Figure 2.3 Lateral Force and Moments. | 25 |
| Figure 2.4 Six Degree of Freedom Variables. | 27 |
| Figure 2.5 Fin Deflection Directions. | 34 |
| Figure 3.1 Open Loop Model. | 38 |
| Figure 3.2 Open Loop Responses. | 39 |
| Figure 3.3 Phugoid Mode. | 39 |
| Figure 3.4 Guidance Path for Simulation. | 40 |
| Figure 3.5 Poles of Open Loop and Desired Close Loop. | 44 |
| Figure 3.6 Full State Feedback Controller Block Diagram. | 47 |
| Figure 3.7 Responses of Pole Placement Method. | 48 |
| Figure 3.8 Pitch Rate Responses of Different Penalizing Matrices. | 51 |
| Figure 3.9 Responses of LQR. | 52 |
| Figure 3.10 Full-state Observer Block Diagram. | 54 |

| <u>Figure</u> | <u>Page</u> |
|---|-------------|
| Figure 3.11 Results of Designed Observer | 56 |
| Figure 3.12 Error Convergence Designed Observer. | 56 |
| Figure 3.13 Complete System Block Diagram. | 58 |
| Figure 3.14 Simulation Block Subsystem. | 59 |
| Figure 4.1 Basic Finner Reference Model. | 60 |
| Figure 4.2 Geometry of Basic Finner Reference (Dimensions are inches) (Source: Dupuis and Hathaway (1997)). | 61 |
| Figure 4.3 Boundary Conditions and Mesh Domain. | 62 |
| Figure 4.4 Meshing Around The Basic Finner (511,139 mesh element). | 64 |
| Figure 4.5 Velocity Contours and Vectors at 0 ° Fin Angle | 65 |
| Figure 4.6 Velocity Contours and Vectors at 2 ° Fin Angle | 66 |
| Figure 4.7 Velocity Contours and Vectors at 4 ° Fin Angle | 66 |
| Figure 5.1 1/4W THT Resistor Dimensions (Source: Vishay (2019)). | 67 |
| Figure 5.2 Firing Accelerations. | 68 |
| Figure 5.3 Setback Acceleration of Projectiles. | 68 |
| Figure 5.4 Prepared Specimens for Hopkinson Bar Experiment. | 71 |
| Figure 5.5 Prepared Specimens (Source: Inel and Özdemir (2021)). | 73 |
| Figure 5.6 Experiment Setup (Source: Inel and Özdemir (2021)). | 74 |
| Figure 5.7 Acceleration and Stress Data (Source: Inel and Özdemir (2021)). | 75 |
| Figure 5.8 Distorted Output Signals of Specimen-5. | 76 |
| Figure 6.1 Designed Inertial Car. | 78 |
| Figure 6.2 IYTE Mechanical Engineering Department Atrium (Source: Hükmü Peker A.Ş.). | 78 |
| Figure 6.3 Magnetic Flux Density Measurements (Date: 04 November 2019). | 79 |
| Figure 6.4 Working Angles of Navigation Functions. | 79 |
| Figure 6.5 Full State Feedback Controller Block Diagram for A-7A Aircraft. | 83 |
| Figure 6.6 Measured ADC Values. | 86 |
| Figure 6.7 APB2 Data Bus of STM32F429 (Source: STMicroelectronics (2016)) . | 87 |
| Figure 6.8 ADC Test Mission. | 88 |
| Figure 6.9 Test Results of STM32F429 ADC. | 89 |
| Figure 6.10 Test Results of ADS8320 ADC. | 90 |

| <u>Figure</u> | <u>Page</u> |
|---|-------------|
| Figure 6.11 Test Results of MCP3201 ADC. | 91 |
| Figure 6.12 Test Results of Square Wave Analog Input. | 92 |
| Figure A.1 Pin Configuration of STM32L052K6. | 95 |
| Figure A.2 Schematic of Designed PCBs for Hopkinson Bar Experiments. | 96 |
| Figure B.1 Experiment Number-1 (Source: (Inel and Özdemir, 2021)). | 97 |
| Figure B.2 Experiment Number-2 (Source: (Inel and Özdemir, 2021)). | 97 |
| Figure B.3 Experiment Number-3 (Source: (Inel and Özdemir, 2021)). | 98 |
| Figure B.4 Experiment Number-4 (Source: (Inel and Özdemir, 2021)). | 98 |
| Figure B.5 Experiment Number-5 (Source: (Inel and Özdemir, 2021)). | 99 |
| Figure B.6 Experiment Number-6 (Source: (Inel and Özdemir, 2021)). | 99 |
| Figure C.1 Aircraft Autopilot Control System Block Diagram. | 100 |

LIST OF TABLES

| <u>Table</u> | <u>Page</u> |
|--|-------------|
| Table 1.1 Comparison of Satellite Systems (Source: (ESA, 2018; IAC, 2021; NOAA, 2021; Kahveci and Yıldız, 2017)) | 14 |
| Table 1.2 Munition Firing Environment (Source: Brown et al. (2001)) | 18 |
| Table 3.1 Design Criteria for Guided Munitions in Reference Studies. | 41 |
| Table 4.1 Properties of Basic Finner (Source: (Dupuis and Hathaway, 1997)). | 62 |
| Table 4.2 Mesh Independence Test. | 64 |
| Table 4.3 Calculated Aerodynamic Coefficients. | 65 |
| Table 5.1 1/4W THT Resistor Dimensions (Source: (Vishay, 2019)). | 67 |
| Table 5.2 Specifications of STML052K6T6 (Source: (STMicroelectronics, 2021)). 72 | 88 |
| Table 5.3 Functionality of PCBs After Experiments. | 76 |
| Table 6.1 Comparison of ADCs. | 88 |

LIST OF SYMBOLS

| | |
|-----------|-------------------------------------|
| a_r | Angular acceleration (rad/s^2) |
| A_z | z-axis acceleration (m/s^2) |
| A_{x_0} | Axial Acceleration Positive Forward |
| V | Translational velocity vector (m/s) |
| V_{m_0} | Total missile velocity |
| \bar{q} | Dynamic pressure (N/m^2) |
| S | Surface reference area (m^2) |
| m | Projectile mass (kg) |
| g | Gravity |
| d | Reference length |
| θ | Pitch angle (deg) |
| ϕ | Roll angle (deg) |
| ψ | Yaw angle (deg) |
| α | Angle of attack (deg) |
| β | Angle of sideslip (deg) |
| C_D | Drag coefficient |
| C_L | Lift coefficient |
| C_M | Pitching moment coefficient |
| C_{Yw} | Sideforce coefficient (wind frame) |
| l | Rolling moment |
| m | Pitching moment |
| n | Yawing moment |
| C_l | Roll moment coefficient |
| C_m | Pitch moment coefficient |
| C_n | Yaw moment coefficient |

| | |
|---------------------|---|
| $C_{z\alpha_0}$ | Pitch Force Coefficient due to Angle of Attack |
| $C_{m\alpha_0}$ | Pitch Moment Coefficient due to Angle of Attack |
| $C_{z\delta_{p_0}}$ | Pitch Force Coefficient due to Fin Deflection |
| $C_{m\delta_{p_0}}$ | Pitch Moment Coefficient due to Fin Deflection |
| p | Roll rate (deg/s) |
| q | Pitch rate (deg/s) |
| r | Yaw rate (deg/s) |
| δ_e, η | Elevator deflection angle (deg) |
| δ_a, ξ | Aileron deflection angle (deg) |
| δ_r, ζ | Rudder deflection angle (deg) |
| I_x | Moment of inertia in the x-axis ($k.m^2$) |
| I_y | Moment of inertia in the y-axis ($k.m^2$) |
| I_z | Moment of inertia in the z-axis ($k.m^2$) |
| T_s | Settling time (second) |
| \bar{x} | Distance from CG to IMU Positive Forward |
| x_E | x-axis position coordinate in earth frame |
| y_E | y-axis position coordinate in earth frame |
| z_E | z-axis position coordinate in earth frame |
| x_b | x-axis position coordinate in body frame |
| y_b | y-axis position coordinate in body frame |
| z_b | z-axis position coordinate in body frame |
| x_w | x-axis position coordinate in wind frame |
| y_w | y-axis position coordinate in wind frame |
| z_w | z-axis position coordinate in wind frame |

LIST OF ABBREVIATIONS

| | |
|-------|--|
| BGA | Ball Grid Array |
| DNS | Direct Numerical Simulation |
| ERGM | Extended-Range Guided Munition |
| IC | Integrated Circuit |
| LORAN | Long Range Navigation |
| MEMS | Micro Electro Mechanical System |
| LES | Large Eddy Simulation |
| PCB | Printed Circuit Board |
| RANS | Reynolds-Averaged Navier-Stokes Simulation |
| RF | Radio Frequency |
| P.O. | Percent Overshoot |
| SMD | Surface Mount Device |
| THT | Through-Hole Technology |

CHAPTER 1

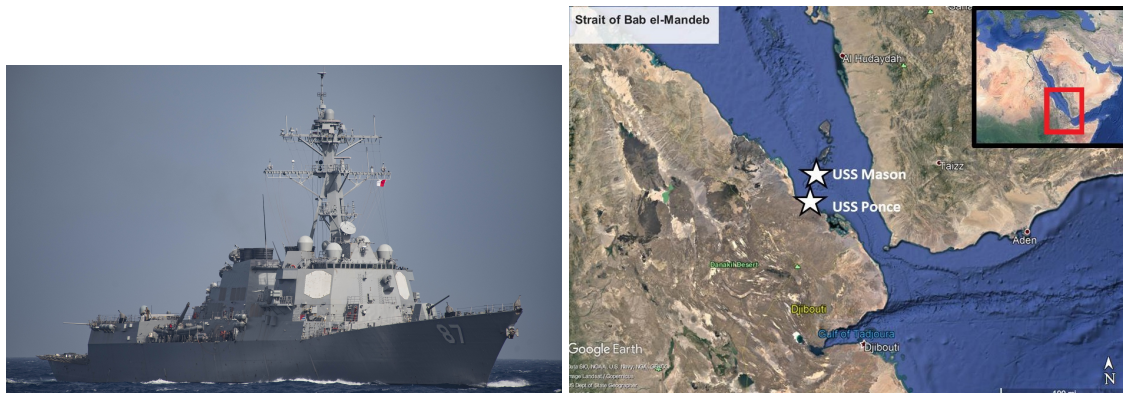
INTRODUCTION

Conventionally, artillery units on sea and on land had been the battle-ram of armed forces for centuries all around the world. The gravity of artillery units looms large as never before on the battlefield. Compelled by this growing trend, major arm developer countries had been focused on the artilleries to transform into even more effective fighting instruments/machine for years/decades. The research prioritized some of the important aspects of this weapon such as guidance, cost, fire power, precision, etc.

Advances in micro-electro-mechanical systems (MEMS) in recent decades enabled weapon developers to place high sensitive guidance kits inside the munitions under harsh conditions. (Brown et al., 2001; Sheard et al., 2008) Bursting out forces during firing, energy consumption, power supply of guidance kit and selection of highly critical electronic components such as microprocessors, microcontrollers, sensors and crystals are some of the important elements that guided munition developing engineers must pay attention carefully to. On the other hand, low profile, hard to detect asymmetric threats are developing their capabilities everyday and requirements of defense systems are also building up. Intercontinental ballistic missiles and long range high altitude defense missiles had been developed by many countries during the cold war. However, small in size but highly effective unmanned aerial vehicles are using for reconnaissance and offense even by countries which have minor defense budgets. Therefore, defense demands of nations are also changing against these new, small in size but threatening high-tech weapons (Digby, 1974).

High unit cost of the enhanced missile defense systems is another drawback even for prosperous countries (Wells, 2000). In 2016, USS Mason was attacked by Houthi rebels while operating in international waters north of the strait of Bab el-Mandeb. Houthi rebels fired two anti-ship cruise missile and USS Mason defended herself and nearby amphibious warship USS Ponce with two SM-2 (Standart Missile-2) missiles and one ESSM (Evolved Sea Sparrow Missile)(LaGrone, 2016). Navy warships have to use every possible options to defend herself and nearby units. However, when the cost of the intercept

guided missiles is considered, some other solutions can be more economical (unit prices of SM-2 Block IV and ESSM are \$2.7M and \$972K respectively (Naval Sea Systems Command Office of Corporate Communication, 2019).



(a) USS Mason (DDG-87) (Source: (LaGrone, 2016)) (b) Strait of Bab El-Mandeb (Source: (Google-Maps, 2020))

Figure 1.1. USS Mason and Strait of Bab El-Mandeb

At shorter ranges smart gun projectiles are emerging as an option, which come up with point accuracy (Morrison and Amberntson, 1977; Digby, 1974; Wells, 2000). Traditionally, conventional gun projectiles have always been in the arsenal of many navy and army over the centuries. Thanks to the developing technologies; size, type, mobility, weight, range and accuracy of the guns inherently have changed. However, accuracy of a gun did not advance as dramatically as range, mobility to name a few. Owing to harsh firing conditions, controlling a projectile after firing was not even possible up until a few decades ago. Technological breakthrough in the field of Micro-Electro-Mechanical Systems (MEMs) has enabled designers to install gun-hardened electronic control circuits inside the projectile shells. When compared with guided missiles, smart gun projectiles have some advantages as below (Morrison and Amberntson, 1977; Digby, 1974; Sheard et al., 2008),

- Low unit cost
- High firing rate
- Ease of storage
- Hard to detect and destroy

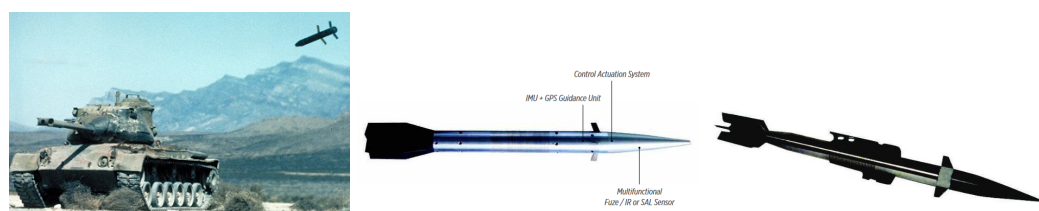
However smart gun projectiles have also some drawbacks such as (Wells, 2000);

- Limited maneuverability
- Light warhead capacity
- Less operation range
- Extreme firing conditions

Limited maneuverability and light warhead capacity can be compensated partly by high firing rate. On the other hand, ranges of conventional munitions can be improved by using special propellants which can provide additional thrust after firing.

1.1. History of Guided Projectiles

First examples of the guided projectiles emerged into battlefields under shadow of the Vietnam War at 70's (Digby, 1974). This new weapon was called as "smart bomb" during the Vietnam War (Morrison and Amberntson, 1977). First guided munitions were used by land forces. Laser guided 155mm M712 Copperhead which is developed at 1975, can be considered as the first combatant guided projectile. By the help of GPS integration to the guidance system, enhanced accuracy capable 155mm M982 Excalibur follows its predecessor. On the other hand 152mm Russian made Krasnopol laser guided projectile and Chinese NORINCO GP-1 and GP-6 are the answers to the west block (Theodoulis and Wernert, 2017).

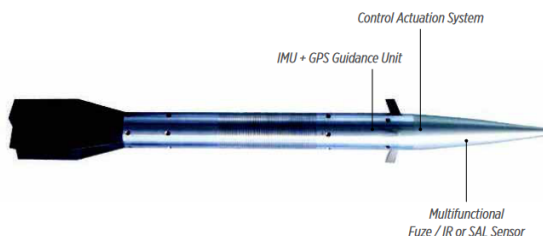


(a) M712 Copperhead (Source: Lockheed Martin BAE Systems (2020)) (b) VULCANO (Source: Leonardo Company (2020)) (c) DART Munition (Source: Leonardo Company (2020))

Figure 1.2. Examples of Guided Munitions.

After the significance of guided projectiles was understood in the battlefield, they started to be used not only in land forces but also in navy. BAE Systems/Leonardo Company made VULCANO, DART munition of Leonardo Company and Extended Range Guided Munition (ERGM) of US Navy are the recognized leading guided munitions in the naval forces. Guided Projectiles can be used in air defense as they are commonly used against land targets. Especially at shorter ranges, quick response capability and high firing rate take them one step forward of guided missiles.

Guided projectiles can be examined under two main groups fin-stabilized and spin-stabilized (Theodoulis and Wernert, 2017). Main difference of two group is the approach to flight stability. Stability is achieved by large and stationary control surfaces in the fin stabilized category. Spin-stabilized guided munitions are more similar to common projectile airframe. Spin-stabilized guided munitions use angular momentum principle to achieve stability.



(a) Fin Stabilized Guided Munition VULCANO
(Source: Lockheed Martin (2020))



(b) BAE Systems Spin Stabilized Munition
(Source: Leonardo Company (2020))

Figure 1.3. Fin-Stabilized and Spin-Stabilized Guided Projectiles.

Examples of fin-stabilized and spin-stabilized guided munitions are shown in figure 1.3. Most of the fin stabilized guided projectiles are similar to guided missiles. VULCANO is one of the fin stabilized guided projectiles. As seen in the figure 1.3a VULCANO has larger control surfaces both at the end and the tip of the munition. On the contrary, spin-stabilized guided munitions use course correction fuses in general. Unlike fin-stabilized guided munitions, course correction fuses can be implemented easily

to the conventional munitions (Theodoulis and Wernert, 2017). Another feature of the spin-stabilized guided munitions is that munition body and course correction fuse are spin-decoupled. Hence, guidance of rapidly spinning munition can be achieved by small canards at the nose of the munition.



Figure 1.4. M1156 Course Correction Fuse (Source: Mönch Publishing Group (2021))

Advantages of course correction fuses can be listed as follows (Theodoulis and Wernert, 2017).

- Low cost guidance kit
- Easy to upgrade conventional munition
- Reduced drag

However, due to limited space for guidance equipments, it is difficult to integrate all required components inside the course correction fuse. Secondly, maneuverability of course correction fuse fitted guided munitions is less than fin-stabilized due to small control surfaces.

1.2. Ballistics

The science of ballistics deals with the procedure of meeting the munition with a desired target. When the prehistoric man hurled first stone to an animal, first step of the ballistic science is also launched (Farrar and Leeming, 1983). The name of ballistics comes from ancient Greek weapon ballista (Farrar and Leeming, 1983).

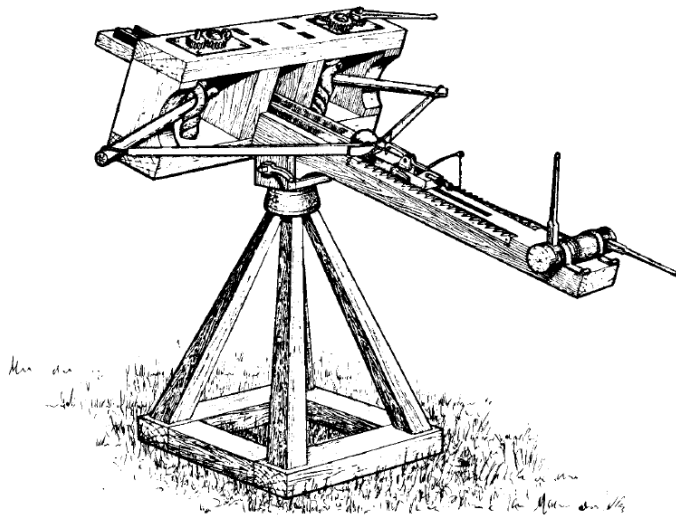


Figure 1.5. Greek Ballista (Source:Farrar and Leeming (1983))

Ballistics is the heart of the artillery firing for centuries. Starting from Aristotle, Galileo, Newton and Leonardo da Vinci many famous scientist interested in ballistics (Farrar and Leeming, 1983). After invention of firearms weapon developer engineers always took ballistics science one step further over time. The science of ballistics is studied under four main topics (Carlucci and Jacobson, 2018; McCoy, 2009).

- Internal Ballistics
- Intermediate Ballistics
- Exterior Ballistics
- Terminal Ballistics

Internal ballistics study area is the relation between barrel, projectile body and propellant before ignition. Internal ballistics consists rifling, burning mechanism of propellant, etc. (Carlucci and Jacobson, 2018).

Intermediate ballistics deals with the first motion of the projectile until it leaves muzzle. Flash suppression, sabot discard, etc. are the field of intermediate ballistics (Carlucci and Jacobson, 2018).

External ballistics comprises the period after projectile leaves muzzle until the time of impact. Projectile stability, flight path prediction and angle of attack, etc. are included in external ballistics (McCoy, 2009).

Terminal ballistics is related with after impact effects such as penetration mechanism and fragmentation methodologies (Carlucci and Jacobson, 2018).

1.3. Guidance

The point of impact for conventional munitions is determined by initial firing conditions such as elevation and train angle of barrel, gun powder inside the shell and wind direction and speed. Therefore, to adjust the trajectory of an conventional munition after firing is not possible. On the other hand, guided munitions modify the flight path continuously during the time of flight. Different techniques can be used in order to meet operational prerequisites (Frieden, 1985).

1.3.1. Phases of Guidance

Munition guidance can be divided into three phases; launch (boost), midcourse guidance and terminal guidance (Frieden, 1985; Bureau of Naval Personnel, 1966).

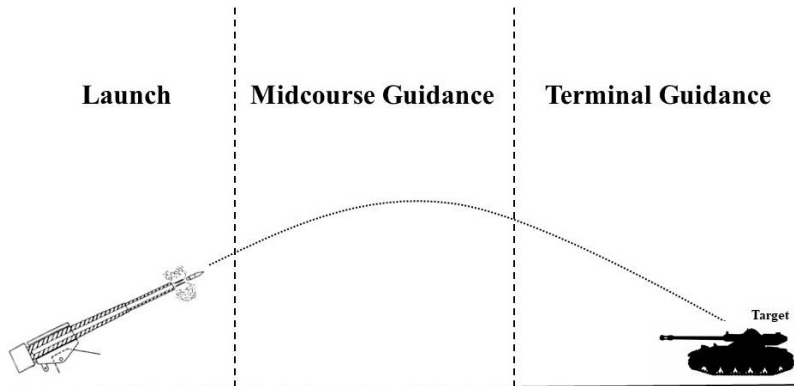


Figure 1.6. Guidance Phases

The objective of the launch phase is to provide required initial velocity and altitude for the rest of the guidance sequence. Since extreme firing conditions during the launch phase, control surfaces of the majority of guided munition are locked in position to ensure survivability of the components.

Midcourse guidance phase is mostly the longest period of the whole time of flight

in both distance and time. Throughout the midcourse guidance phase, autopilot of the guided munition is active and main objective of the control system is to bring the munition near the target by using navigation instruments.

Terminal guidance phase is the most momentous part of the whole process. Guidance system of the munition must have high accuracy and be fast enough to respond guidance commands. Depending on the potential target maneuverability, terminal phase of the guidance system has to satisfy the final maneuvers for interception.

1.3.2. Types of Guidance

Guidance of munitions can be summarized under two main groups (Frieden, 1985; Bureau of Naval Personnel, 1966),

- Guidance systems that use man-made electromagnetic devices
- Self-contained guidance systems

In the first category, munitions are controlled by external devices such as radars and electromagnetic radiation of the target. In the latter, munitions use internal sensor systems or celestial and terrestrial sources such as stars and topography.

1.3.2.1. Guidance Systems that Use Man-Made Electromagnetic Devices

Munition guidance systems that depend on man-made electromagnetic devices operate on the basis of direct electromagnetic radiation contact. If a guided munition is directly controlled by a friendly radar source, this guidance is categorized as control guidance (radar control guidance). In general, connection between control point and guided munition is carried out by the use of radar or radio link (Frieden, 1985). Radar control of a guided munition can be performed in two ways. If all guidance instructions are calculated by control point and then send them to the munition, this method known as command control. On the other hand, if the munition can calculate its own correction signals depend on radar scan axis, this method is grouped as beam-rider control.

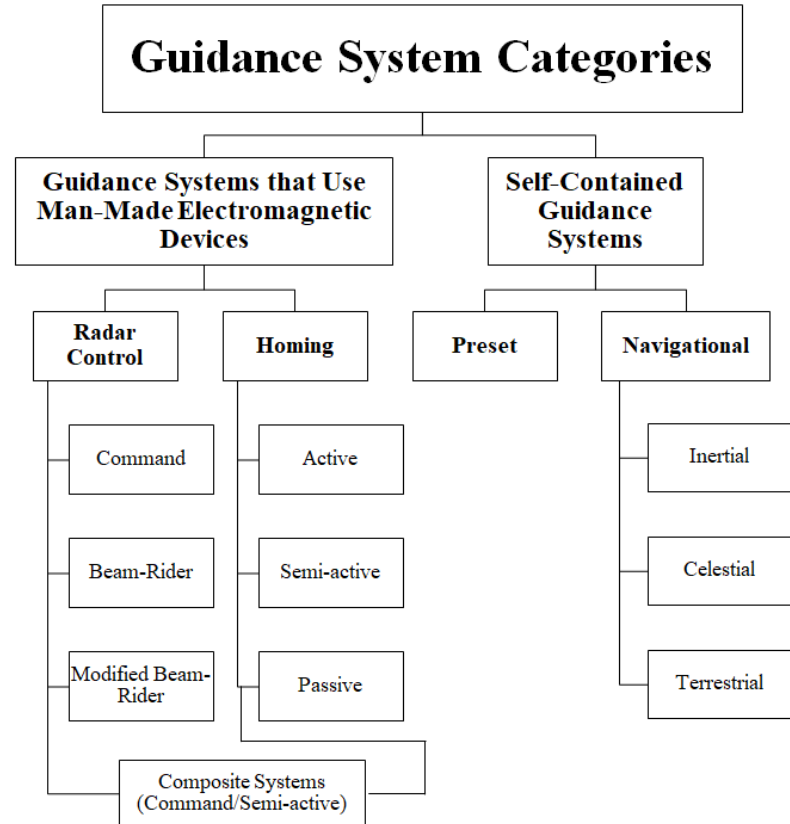


Figure 1.7. Guidance System Categories (Source: Frieden (1985))

Beam-rider and command control methods have some advantages over each other (Frieden, 1985). Due to the guidance correction commands calculated within the body of munition, more than one munition can be ridden in beam-rider method. However accuracy of the beam-rider method decreases with the range because radar beam spreads out and it is more difficult to position the missile.

Homing guidance is another approach of guidance systems that depends on man-made electromagnetic devices. Homing munitions are sensitive to one or more specific feature of the target such as infrared, reflected RF or laser beam, sound and visible light. Homing guidance may be divided into three groups (Frieden, 1985; Bureau of Naval Personnel, 1966),

- Active homing
- Semi-active homing
- Passive homing

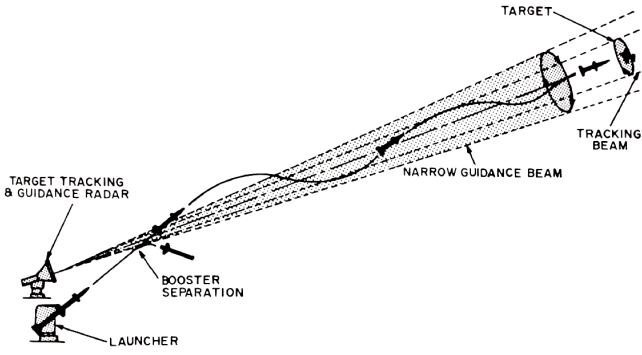


Figure 1.8. Simple Beam-Rider Guidance System (Source:Frieden (1985))

Guided munition has both of transmitter and receiver in active guidance method. External guidance computers are not involved in active homing and all signal transmission, acquisition and evaluation are executed within the munition.

Semiaactive homing munitions requires at least one external RF source that illuminates the target. Target tracking is carried out with the help of internal receiver and guidance path correction is performed by internal guidance computer. Semiaactive munitions are not suited with a transmitter unit.

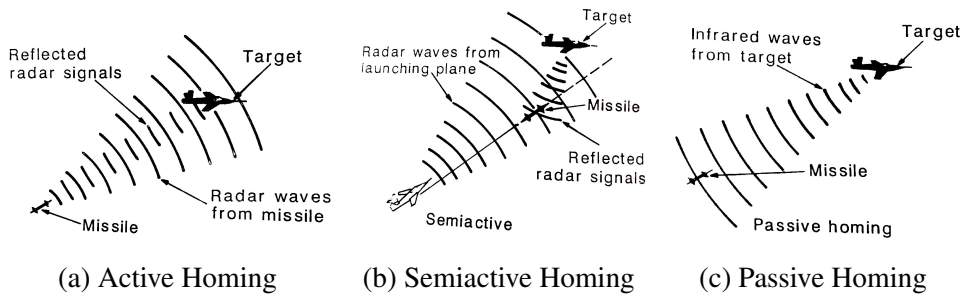


Figure 1.9. Illustration of Homing Guidance Types (Source: Frieden (1985)).

Passive homing munitions only depend on a specific emitted signal from a target which can be RF, infrared or visible light. Passive homing devices have only receiver unit as semiaactive homing munitions. However, there is no need to any external target illuminator radar. Passive homing munitions generate own guidance path corrections on the basis of emitted signal from the target.

1.3.2.2. Self-Contained Guidance Systems

If all guidance system is within the munition body and guided munition does not depend on any external RF or any kind of source it is named as self-contained guidance. Self-contained guidance systems can be grouped under preset guidance, inertial guidance, celestial guidance and terrestrial guidance (Frieden, 1985; Bureau of Naval Personnel, 1966).

In preset guidance all trajectory calculations are done before firing and guidance data are transferred to the guidance computer inside the munition. Preset guided munition follows the given trajectory by internal sensors such as gyroscopes and accelerometers. Firing unit is not able to modify the trajectory of munition after firing. Therefore, preset guided munitions are not useful against mobile targets such as aircrafts.

Guided munitions which have inertial guidance system has similar hardware with preset guided munitions. Main difference of inertial guidance is that guidance path calculation is carried out continuously by guidance computer after firing inside the munition using inertial measurement units such as accelerometers, gyroscopes and magnetometers.

Celestial guidance by other words stellar guidance system uses stars as reference. Navigation system continuously measures the elevation angles of stars and compares with pre-loaded star chart. Celestial navigation is highly dependent on visibility conditions of reference stars. Therefore, munitions which are equipped with celestial navigation system have to cruise above clouds.

Terrestrial guidance systems depends on comparison of in-flight recorded pictures and previously embedded terrain photos. Due to complexity the system is effective against only large area target such as industrial zones.

1.4. Navigation Methods

The art and science of navigation involves charting a path between two any desired points or more optimally. Navigation process considers position, course and distance that are traveled by the craft. It should be noted that as long as the progress of a vehicle from one point to another is carried out deliberately, it could only then named as navigation. Otherwise, all else could not considered navigation such as drifting. Specified destination,

course and speed are always considered by navigators. Throughout the history navigators used different navigation techniques such as; inertial navigation (dead reckoning), terrestrial navigation, celestial navigation and electronic navigation.

1.4.1. Inertial Navigation (Dead Reckoning)

Inertial navigation is one of the most commonly used techniques before the invention of satellite navigation. To determine the current position, inertial navigation technique incrementally integrates the distance traveled and the direction of travel relative to a known reference point (Edelkamp and Schrödl, 2012). Magnetic compasses (magnetometers), gyroscopes, accelerometers, high accuracy clocks are used to determine course and distances according to known position. Inertial or dead reckoning navigation systems have several advantages such as relatively low cost equipments, basic principles and compact size. On the other hand position estimation errors increase by the time and it is called “drift error”. Even though, high performance sensors are used in inertial navigation systems, erratic external forces such as sudden gust of wind induce the calculated trajectory. The key advantage of inertial navigation is the independence from external electronic equipments. Inertial navigation systems are standalone structures that all measurement are done inside the system (Frieden, 1985).

1.4.2. Terrestrial Navigation

Terrestrial, in other words visual navigation, calculate positions with respect to a known and visible landmarks by using maps and optical instruments (Bernhard et al., 2003). This navigation method is highly dependent on visibility conditions of benchmark objects and weather. On the other hand, because of high reliability, seafarers mostly prefer terrestrial navigation methods especially in narrow water channels like Çanakkale and İstanbul Straits.

1.4.3. Celestial Navigation

The origins of celestial navigation could be traces back to ancient world. Long before the seafarers managed to cross the oceans in 15th century, celestial navigation had been used as one of the main navigation method. Interestingly, despite the cutting edge technology and precise electronic navigation equipments, celestial navigation techniques are been taught in almost every maritime schools. Position of stars and planets such as Polaris (north star) and Jupiter are using as a reference in celestial navigation method. Specific instruments such as sextant and almanac are using to calculate position (Bernhard et al., 2003). Although it is not preferred because of low accuracy, complex instruments for calculating position, celestial navigation method must be known well by every seafarer as a backup. However if there is not any other solution to identify the position as in a spacecraft, celestial navigation inevitably is the first preference.

1.4.4. Electronic Navigation

There are many electronic navigation methods such as Gee, LORAN, Decca and so on. However after establishing of Global Navigation Satellite Systems (GNSS), the methods other than satellite navigation lost its appeal in some fields. Global Positioning System (GPS) of United States, Global'naya Navigatsionnaya Sputnikovaya Sistema (GLONASS) of Russia, Gallileo Positioning system of European Union, BeiDou Navigation Satellite System of China, Navigation with Indian Constellation (NAVIC) of India and Quasi-Zenith Satellite System (QZSS) of Japan are the already in use main satellite positioning systems (ESA, 2018; Kahveci and Yıldız, 2017). Although satellite systems are very expensive, due to security issues countries are going to establish their own satellite systems. Comparison of each satellite system is shown in the table 1.1 below.

GNSS signals cover wide areas and can be received by multiple user antennas. However, accuracy of GNSS for civilian usage is not better than 10 meters (Kahveci and Yıldız, 2017). In addition to that, due to errors such as signal reflections and phase shifting, satellite navigation is not feasible for indoor navigation and other critical operations (Kahveci and Yıldız, 2017).

Table 1.1. Comparison of Satellite Systems (Source: (ESA, 2018; IAC, 2021; NOAA, 2021; Kahveci and Yıldız, 2017)).

| Parameter | GLONASS (Russia) | GPS (United States) | GALILEO (European Union) |
|--------------------------------------|----------------------------------|--------------------------|-----------------------------|
| Satellite Number | 23 | 31 | 24 |
| Orbit Number | 3 | 6 | 3 |
| Orbit Angle (Degree) | 64.8 | 55 | 56 |
| Orbit Radius (km) | 19100 | 20200 | 29599.8 |
| Frequency (Mhz) | L1:1602-161505 L2:1246-1256.2 | L1:1575.42 L2:1227.60 | L1:1554-1596 |
| Navigation Message Duration (minute) | 2.5 | 12.5 | F/NAV:10 I/NAV:720 |

1.4.5. Advantages and Drawbacks of Inertial Navigation

Inertial navigation method stands out from other navigation techniques where they are not applicable in some conditions such as indoor navigation problems and under extreme dynamic conditions. Compact sizes, low cost measurement units, independence from external signals, robust design opportunities can be stated as the main advantages of inertial navigation systems. However, inertial navigation systems are using body frame of the vehicle and magnetic field of earth as reference. Hereby, measurement errors of sensors cause incrementally increasing an error which is named drift error. An example of drift error is illustrated in the figure 1.10.

Figure 1.10 shows the measured acceleration and calculated velocity and displacement data from MPU6050 during a simple up and down movement. Velocity and displacement data is calculated with numerical integration method, trapezoid rule. It is clearly seen in the figure 1.10 that after every up and down motion a constant error is observed in velocity data and time dependent error occurs in displacement data.

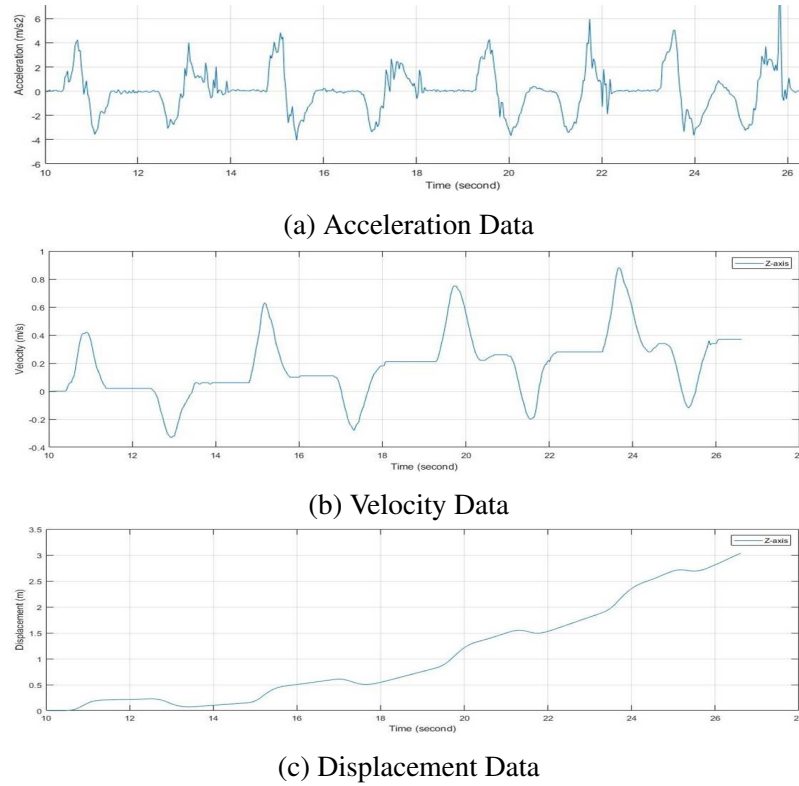


Figure 1.10. Displacement Measurement with MPU6050.

Combination of inertial and GNSS is can be a solution for eliminating “drift error”. Nevertheless, additional components for other navigation systems are increasing size and complexity of inertial navigation system.

1.5. Model Based Simulation

Model based simulation techniques are widely used to validate, verify and develop hardware and software for many application areas from a kitchen toasters to embedded avionic systems for aircrafts (Garousi et al., 2018). These techniques are popular for easily changeable test parameters, low cost equipments with respect to live tests and infinite repeatability. Therefore, before the live field experiments, hardware and software of the critical systems such as guided projectiles or missiles, can be tested using model based simulations methods.

Some of the commonly used model based simulations can be listed as below.

- Software in the Loop (SIL)

- Processor in the Loop (PIL)
- Hardware in the Loop (HIL)

All model based simulations aim to conduct the desired process under a condition as close to the real operation as possible. They distinguish in the area of where the code is tested and execution method (MathWorks, d,a,f).

In SIL, the code is generated only for development computer and tested as a separate process in the development computer and code execution is nonreal time (MathWorks, d).

The code in PIL is compiled for both development computer and target hardware. A file such as “.hex” or any format that can be executable in hardware is generated. A part of the model is executed in the development computer and target hardware interacts with development computer (MathWorks, a). Code execution is also nonreal time as in SIL.

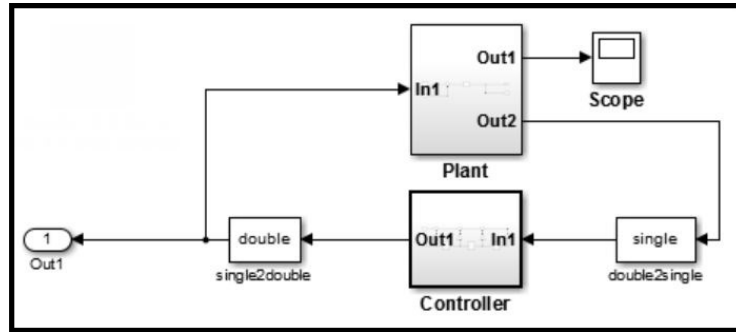
The most independent case from the development computer is the HIL. An executable proper file such as “.hex” is generated as in PIL, however all of the computation is carried out inside the target hardware and a controller hardware supplies external simulated signals such as wind speed, fuel injection rate etc. to the target hardware (MathWorks, f). Code is executed real time in contrast to SIL and PIL.

Example SIL, PIL and HIL block diagrams for MATLAB Simulink models are shown in the figure 1.11.

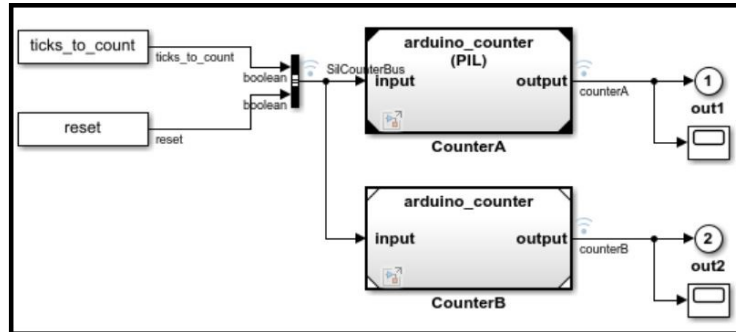
1.6. CFD Analysis of Munitions

The aerodynamic parameters of guided munitions are critical for designing navigation system. These parameters can be calculated using computer software, besides live field experiments. One of the significant advantage of the computer software in determining the aerodynamic parameters is the infinite repeatability. Therefore, CFD analysis of the munitions can be conducted easily, using different boundary and initial conditions many times until design criteria are satisfied.

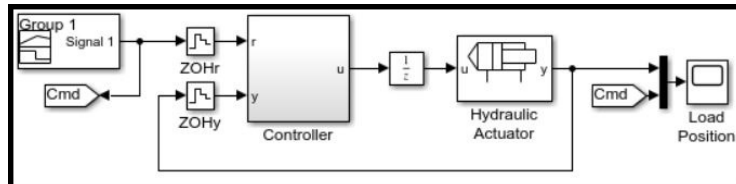
Since the air flow around the munition air-frame is turbulent in general, there is several appropriate CFD models for determining desired aerodynamic coefficients. The



(a) Example SIL Block Diagram (Source:(MathWorks, e)).



(b) Example PIL Block Diagram (Source:(MathWorks, b)).



(c) Example HIL Block Diagram (Source:(MathWorks, c)).

Figure 1.11. Example Model Based Simulation Block Diagrams.

turbulent CFD models can be listed as below (Versteeg and Malalasekera, 2007).

- Reynolds-averaged navier-stokes (RANS) based turbulence models
- Large Eddy simulations (LES)
- Direct numerical simulations (DNS)

Since the RANS based models are the most straightforward turbulence, they preferred at the initial validation of the parameters. However, the RANS based models require two more equations and in some cases such as rotating flow the solution may not be accurate enough (Versteeg and Malalasekera, 2007).

LES based models are used when the magnitude of the turbulence in the flow is more important. However, LES models require more computational time than RANS

based model (Versteeg and Malalasekera, 2007).

Required time for solving the flow is the highest in DNS models, since complete unsteady navier-stokes equations are solved. Examples of mentioned solution models are shown in the figure 1.12.

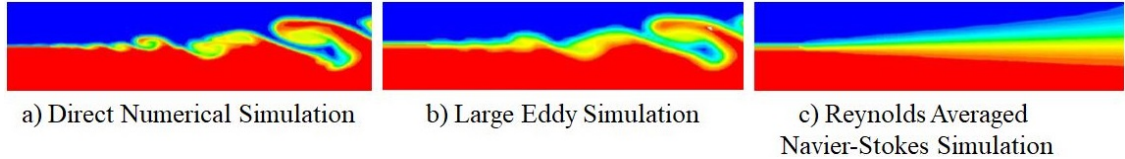


Figure 1.12. Comparison of Turbulence Models (Source:(ANSYS, 2014)).

1.7. High-g Ruggedization of Electronic Boards

Projectile firing generates extreme physical conditions just within microseconds. Therefore, the guided projectiles which are consist of many sensitive electronic components have to be designed to endure these severe impacts during the launch. The acceleration environments of some munitions are shown in the table 1.2.

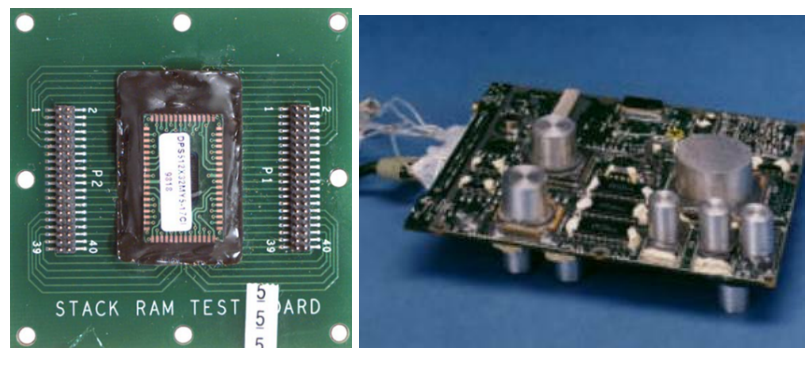
Table 1.2. Munition Firing Environment (Source: (Brown et al., 2001)).

| Launch Parameter | Unit | Tank Munition (120mm) | Artillery Munition (155mm) | Mortar Munition (4,2") |
|--------------------------|-------------|----------------------------------|---------------------------------------|-----------------------------------|
| Max. Axial Acceleration | g | 100K | 20K | 10K |
| Max. Radial Acceleration | g | 10K | 2K | 1K |
| Time in Bore | ms | 710 | 1020 | 5 |

High-g ruggedization methods have to be applied to the electronic components inside the shell for protection against extreme firing conditions. However, there is very limited source in the literature for ruggedization applications and importance for guided projectiles and munition. The study of (Burd, 1999) can be considered as one of the valuable study in the literature. Burd explains some of the key points of high-g ruggedization

applications and specimen test methods. Major ruggedizations methods for projectile electronics can be listed as below (Burd, 1999);

- Smallest and lowest weight parts must be preferred
- Air gap capacitor must be avoided
- Ball Grid Array (BGA) package IC's must be preferred
- Epoxy molding is a good solution to hold components tight
- Circuit boards can be fixed to the structure by using metal pins



(a) Example Test Board (b) Demonstration of GPS board showing metal pins to hold IC's in place.

Figure 1.13. Examples of High-G Ruggedization Methods (Source: Burd (1999)).

CHAPTER 2

DYNAMIC ANALYSIS OF GUIDED PROJECTILES

2.1. Reference Frames

Every object whether in the air, on land or under the sea requires a reference frame to describe the motion. In the literature there is various defined reference frames. For instance heliocentric frame is used to define the motion of earth around the sun, geocentric or inertial frame takes the origin as a center of earth, earth frame uses greenwich and equatorial plane as a reference to measure longitude and latitude respectively (Zipfel, 2007).

On the other hand, body frame and wind frame are mainly used for aircrafts to define the forces and moments that are acting on the object (Zipfel, 2007). Base points of both reference frames are the same the center of mass of the object. However direction of the base vectors are different in both frames.

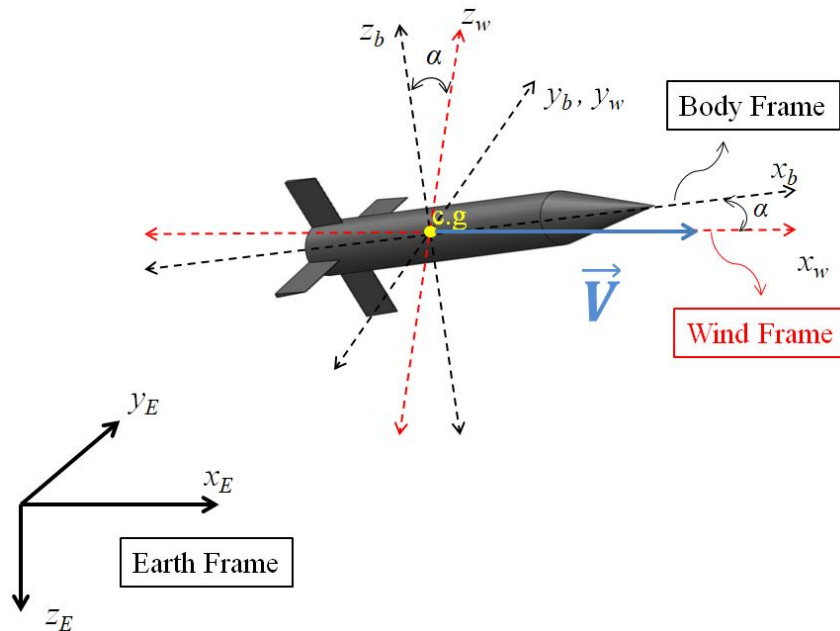


Figure 2.1. Earth, Body and Wind Frames.

While the positive x-direction is the nose of the aircraft in body frame, the positive x-direction is the velocity vector of the aircraft in wind frame. Both reference frame are used in the literature depending on the desired analysis of the motion (Cook, 2007).

2.2. Forces and Moments

Aircraft dynamics are studied usually in terms of longitudinal and lateral for symmetric aircrafts, since the forces and moments influence more dominantly one than other. For instance, elevator deflection changes the pitch angle, however sideslip angle does not change considerably much. It is also same for other control inputs such as rudder and aileron. Last of all, this kind of analyses named as decoupled longitudinal and lateral motion equations (Cook, 2007).

2.2.1. Longitudinal Forces and Moments

In longitudinal aerodynamics three basis forces lift, drag and gravitational force and pitching moment act on the objects. Since the lift and drag force occur in the wind axis, they need to be transformed to the body axis for better motion analysis.

Firstly, lift and drag forces and pitching moment are defined as follows (Beard and McLain, 2012; Cook, 2007).

$$F_{lift} = \frac{1}{2}\rho V^2 S C_L \quad (2.1)$$

$$F_{drag} = \frac{1}{2}\rho V^2 S C_D \quad (2.2)$$

$$m = \frac{1}{2}\rho V^2 S c C_m \quad (2.3)$$

Body axis components of lift and drag forces in wind axis can be written as follows.

$$F_{lift} = F_{lift} \sin \alpha - F_{lift} \cos \alpha$$

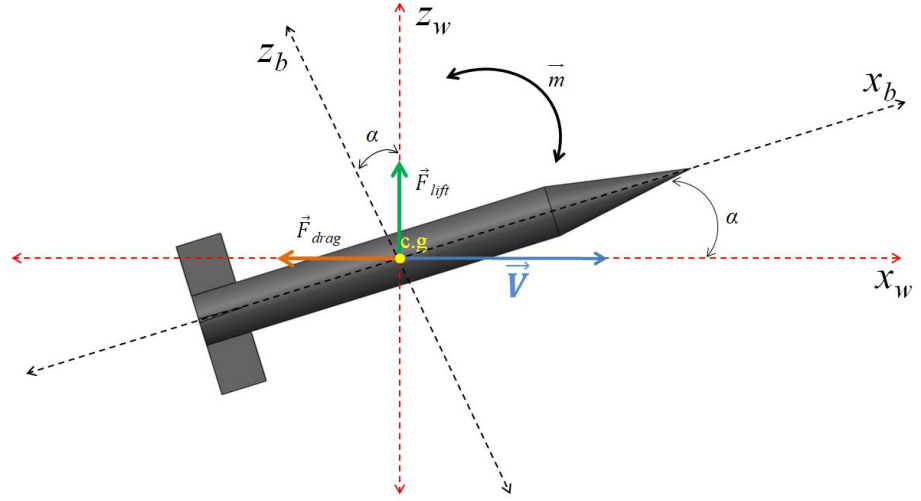


Figure 2.2. Longitudinal Forces and Moment.

$$F_{drag} = -F_{drag}\cos\alpha - F_{drag}\sin\alpha$$

Then, aerodynamic forces in body axis can be written as follows (Beard and McLain, 2012; Cook, 2007).

$$f_x = -F_{drag}\cos\alpha + F_{lift}\sin\alpha$$

$$f_y = -F_{drag}\sin\alpha - F_{lift}\cos\alpha$$

$$\begin{aligned} \begin{pmatrix} f_x \\ f_y \end{pmatrix} &= \begin{pmatrix} \cos\alpha & -\sin\alpha \\ \sin\alpha & \cos\alpha \end{pmatrix} \begin{pmatrix} -F_{drag} \\ -F_{lift} \end{pmatrix} \\ \begin{pmatrix} f_x \\ f_y \end{pmatrix} &= \begin{pmatrix} \cos\alpha & -\sin\alpha \\ \sin\alpha & \cos\alpha \end{pmatrix} \begin{pmatrix} -\frac{1}{2}\rho V^2 S C_D \\ -\frac{1}{2}\rho V^2 S C_L \end{pmatrix} \end{aligned} \quad (2.4)$$

The critical part in the equation 2.4 is the lift and drag coefficients. Lift, drag and pitching moment coefficients are a function of α, q, δ_e (Beard and McLain, 2012; Cook, 2007).

$$C_L(\alpha, q, \delta_e)$$

$$C_D(\alpha, q, \delta_e)$$

$$C_m(\alpha, q, \delta_e)$$

Except for small changes in angle of attack the coefficients are nonlinear. Hence they have to be approximated. Taylor series approximation of the lift coefficient can be written as follows (Beard and McLain, 2012; Cook, 2007).

$$C_L = C_{L0} + \frac{\partial C_L}{\partial \alpha} \alpha + \frac{\partial C_L}{\partial q} q + \frac{\partial C_L}{\partial \delta_e} \delta_e$$

C_{L0} is the lift coefficient when $\alpha = 0, q = 0, \delta_e = 0$, $\frac{\partial C_L}{\partial \alpha}$ is the lift coefficient due to angle of attack, $\frac{\partial C_L}{\partial q}$ is the lift coefficient due to pitch rate and $\frac{\partial C_L}{\partial \delta_e}$ is the lift coefficient due to elevator deflection (Beard and McLain, 2012; Cook, 2007).

$\frac{\partial C_L}{\partial \alpha}, \frac{\partial C_L}{\partial q}$ and $\frac{\partial C_L}{\partial \delta_e}$ are abbreviated as $C_{L\alpha}, C_{Lq}, C_{L\delta_e}$ (Beard and McLain, 2012; Cook, 2007).

Lift coefficient linear approximation with terms of longitudinal stability derivatives can be written as follows (Beard and McLain, 2012; Cook, 2007).

$$C_L = C_{L0} + C_{L\alpha} \alpha + C_{Lq} \frac{c}{2V} q + C_{L\delta_e} \delta_e \quad (2.5)$$

Drag and pitching moment coefficients linear approximation can be also written as in the lift coefficient, with the terms of longitudinal stability derivatives as follows (Beard and McLain, 2012; Cook, 2007).

$$C_D = C_{D0} + C_{D\alpha} \alpha + C_{Dq} \frac{c}{2V} q + C_{D\delta_e} \delta_e \quad (2.6)$$

$$C_m = C_{m0} + C_{m\alpha} \alpha + C_{mq} \frac{c}{2V} q + C_{m\delta_e} \delta_e \quad (2.7)$$

Longitudinal forces and moment can be written as substituting the the equations 2.5, 2.6, 2.7 in 2.1, 2.2, 2.3 as follows.

$$F_{lift} = \frac{1}{2} \rho V^2 S \left(C_{L0} + C_{L\alpha} \alpha + C_{Lq} \frac{c}{2V} q + C_{L\delta_e} \delta_e \right) \quad (2.8)$$

$$F_{drag} = \frac{1}{2} \rho V^2 S \left(C_{D0} + C_{D\alpha} \alpha + C_{Dq} \frac{c}{2V} q + C_{D\delta_e} \delta_e \right) \quad (2.9)$$

$$m = \frac{1}{2} \rho V^2 S c \left(C_{m0} + C_{m\alpha} \alpha + C_{mq} \frac{c}{2V} q + C_{m\delta_e} \delta_e \right) \quad (2.10)$$

However at high α , the coefficients C_L , C_D and C_m do not change linearly, due to abrupt change in lift when the stall condition occurs since, the coefficients C_L , C_D and C_m are the function of α for nonlinear conditions. Therefore, these coefficients are specifically determined for each aircraft in wind tunnel experiments, computer simulations and live flight tests (Cook, 2007; Zipfel, 2007; Beard and McLain, 2012; Zarchan, 2012). Forces and moment for longitudinal motion can be summarized as follows (Beard and McLain, 2012).

$$F_{lift} = \frac{1}{2} \rho V^2 S \left(C_L(\alpha) + C_{Lq} \frac{c}{2V} q + C_{L\delta_e} \delta_e \right) \quad (2.11)$$

$$F_{drag} = \frac{1}{2} \rho V^2 S \left(C_D(\alpha) + C_{Dq} \frac{c}{2V} q + C_{D\delta_e} \delta_e \right) \quad (2.12)$$

$$m = \frac{1}{2} \rho V^2 S c \left(C_m(\alpha) + C_{mq} \frac{c}{2V} q + C_{m\delta_e} \delta_e \right) \quad (2.13)$$

Gravitational force also have to be transformed to the body axis and can be written as follows (Beard and McLain, 2012; Cook, 2007). Since the gravitational force directly is applied to the *c.g*, no moment is generated, hence moment equation is not written for gravitational force.

$$F_{gw} = \begin{pmatrix} 0 \\ 0 \\ mg \end{pmatrix}$$

$$F_{gb} = \begin{pmatrix} -mg \sin \theta \\ mg \cos \theta \sin \phi \\ mg \cos \theta \cos \phi \end{pmatrix} \quad (2.14)$$

2.2.2. Lateral Forces and Moments

Lateral force, roll and yaw moment are defined similar to the longitudinal terms as below (Beard and McLain, 2012; Cook, 2007).

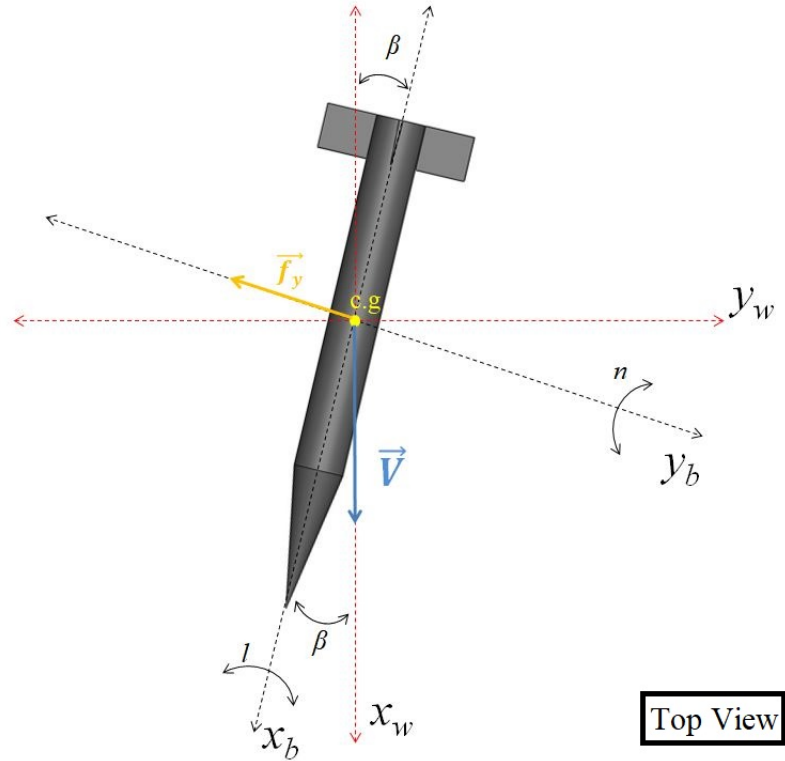


Figure 2.3. Lateral Force and Moments.

$$f_y = \frac{1}{2} \rho V^2 S C_Y \quad (2.15)$$

$$l = \frac{1}{2} \rho V^2 S b C_l \quad (2.16)$$

$$n = \frac{1}{2} \rho V^2 S b C_n \quad (2.17)$$

where C_Y , C_l and C_n are β , p , r , δ_a and δ_r dependent non-dimensional aerodynamic coefficients. These coefficients can be also defined as below, using the same methodology as in the longitudinal coefficients (Beard and McLain, 2012; Cook, 2007).

$$C_Y = C_{Y_0} + C_{Y\beta}\beta + C_{Yp}\frac{b}{2V}p + C_{Yr}\frac{b}{2V}r + C_{Y\delta_a}\delta_a + C_{Y\delta_r}\delta_r \quad (2.18)$$

$$C_l = C_{l_0} + C_{l\beta}\beta + C_{lp}\frac{b}{2V}p + C_{lr}\frac{b}{2V}r + C_{l\delta_a}\delta_a + C_{l\delta_r}\delta_r \quad (2.19)$$

$$C_n = C_{n_0} + C_{n\beta}\beta + C_{np}\frac{b}{2V}p + C_{nr}\frac{b}{2V}r + C_{n\delta_a}\delta_a + C_{n\delta_r}\delta_r \quad (2.20)$$

Lateral force and moment can be expanded as below, substituting the coefficients C_Y, C_l, C_n in equation 2.18, 2.19, 2.20 to the equations 2.15, 2.16, 2.17 (Beard and McLain, 2012).

$$f_y = \frac{1}{2}\rho V^2 S \left[C_{Y_0} + C_{Y\beta}\beta + C_{Yp}\frac{b}{2V}p + C_{Yr}\frac{b}{2V}r + C_{Y\delta_a}\delta_a + C_{Y\delta_r}\delta_r \right] \quad (2.21)$$

$$l = \frac{1}{2}\rho V^2 S b \left[C_{l_0} + C_{l\beta}\beta + C_{lp}\frac{b}{2V}p + C_{lr}\frac{b}{2V}r + C_{l\delta_a}\delta_a + C_{l\delta_r}\delta_r \right] \quad (2.22)$$

$$n = \frac{1}{2}\rho V^2 S b \left[C_{n_0} + C_{n\beta}\beta + C_{np}\frac{b}{2V}p + C_{nr}\frac{b}{2V}r + C_{n\delta_a}\delta_a + C_{n\delta_r}\delta_r \right] \quad (2.23)$$

All force equations f_x, f_y and f_z can be summarized as below.

$$f_x = \left(-mg\sin\theta \right) + \frac{1}{2}\rho V^2 S \left(C_X(\alpha) + C_{Xq}(\alpha)\frac{c}{2V}q + C_{X\delta_e}(\alpha)\delta_e \right) \quad (2.24)$$

$$f_y = \left(mg\cos\theta \sin\phi \right) + \frac{1}{2}\rho V^2 S \left(C_{Y_0} + C_{Y\beta}\beta + C_{Yp}\frac{b}{2V}p + C_{Yr}\frac{b}{2V}r + C_{Y\delta_a}\delta_a + C_{Y\delta_r}\delta_r \right) \quad (2.25)$$

$$f_z = \left(mg\cos\theta \cos\phi \right) + \frac{1}{2}\rho V^2 S \left(C_Z(\alpha) + C_{Zq}(\alpha)\frac{c}{2V}q + C_{Z\delta_e}(\alpha)\delta_e \right) \quad (2.26)$$

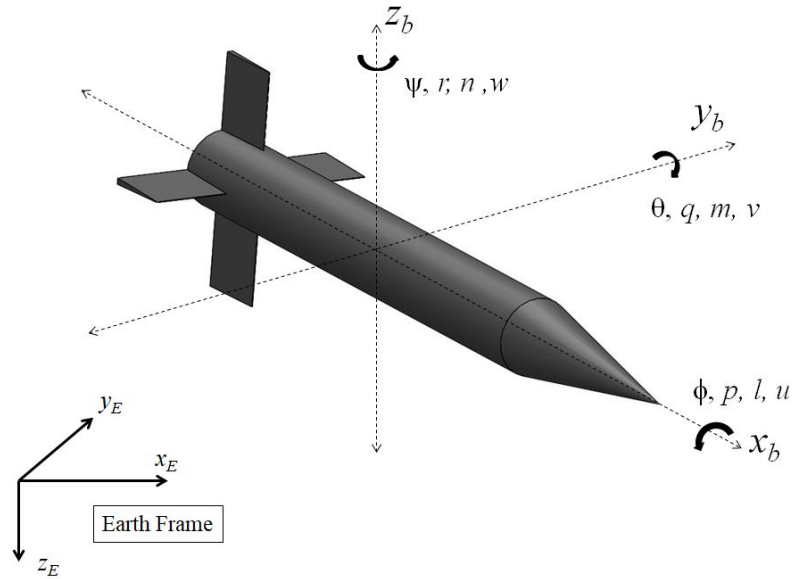


Figure 2.4. Six Degree of Freedom Variables.

2.2.3. Six Degree of Freedom Equations of Motion

Six degree of freedom (6-DoF) equations of motion include position (x_E, y_E, z_E), rotation angles (ϕ, θ, ψ), rotation angle rates (p, q, r) and velocity components (u, v, w) in three dimensions.

2.2.3.1. Earth Axis Position Equations

The position of a guided projectile can be defined using the body frame velocity components u, v and w . However body frame velocity components have to be rotated to the earth frame (Beard and McLain, 2012; Cook, 2007).

$$\frac{d}{dt} \begin{pmatrix} x_E \\ y_E \\ z_E \end{pmatrix} = (R_w^b)^{-1} \begin{pmatrix} u \\ v \\ w \end{pmatrix}$$

$$\begin{pmatrix} \dot{x}_E \\ \dot{y}_E \\ \dot{z}_E \end{pmatrix} = (R_w^b)^{-1} \begin{pmatrix} u \\ v \\ w \end{pmatrix} \quad (2.27)$$

Inverse of the rotation matrix $(R_w^b)^{-1}$ from wind axis to body axis is also defined as below (Beard and McLain, 2012; Cook, 2007).

$$(R_w^b)^{-1} = \begin{pmatrix} \cos\theta \cos\psi & \sin\phi \sin\theta \cos\psi - \cos\phi \sin\psi & \cos\phi \sin\theta \cos\psi + \sin\phi \sin\psi \\ \cos\theta \sin\psi & \sin\phi \sin\theta \sin\psi + \cos\phi \cos\psi & \cos\phi \sin\theta \sin\psi - \sin\phi \cos\psi \\ -\sin\theta & \sin\phi \cos\theta & \cos\phi \cos\theta \end{pmatrix} \quad (2.28)$$

Position terms can be found substituting the equation 2.28 to equation 2.27 as below (Beard and McLain, 2012; Cook, 2007).

$$\begin{pmatrix} \dot{x}_E \\ \dot{y}_E \\ \dot{z}_E \end{pmatrix} = \begin{pmatrix} \cos\theta \cos\psi & \sin\phi \sin\theta \cos\psi - \cos\phi \sin\psi & \cos\phi \sin\theta \cos\psi + \sin\phi \sin\psi \\ \cos\theta \sin\psi & \sin\phi \sin\theta \sin\psi + \cos\phi \cos\psi & \cos\phi \sin\theta \sin\psi - \sin\phi \cos\psi \\ -\sin\theta & \sin\phi \cos\theta & \cos\phi \cos\theta \end{pmatrix} \begin{pmatrix} u \\ v \\ w \end{pmatrix} \quad (2.29)$$

Position in z-axis defines the altitude. However the negative direction is used more commonly to represent the altitude $h = -z_E$. The equation 2.29 can be also expanded as below.

$$\dot{x}_E = u(\cos\theta \cos\psi) + v(\sin\phi \sin\theta \cos\psi - \cos\phi \sin\psi) + w(\cos\phi \sin\theta \cos\psi + \sin\phi \sin\psi) \quad (2.30)$$

$$\dot{y}_E = u(\cos\theta \sin\psi) + v(\sin\phi \sin\theta \sin\psi - \cos\phi \cos\psi) + w(\cos\phi \sin\theta \sin\psi + \sin\phi \cos\psi) \quad (2.31)$$

$$\dot{h} = u \sin\theta - v \sin\phi \cos\theta - w \cos\phi \cos\theta \quad (2.32)$$

2.2.3.2. Body Axis Rotation Angle Equations

Derivatives of rotation angles can be also defined using the rotation angle rates. Therefore rotation angle rates have to be converted from wind axis to body axis as below (Beard and McLain, 2012; Cook, 2007).

$$\begin{aligned}
 \begin{pmatrix} p \\ q \\ r \end{pmatrix} &= \begin{pmatrix} \dot{\phi} \\ \dot{\theta} \\ \dot{\psi} \end{pmatrix} + \begin{pmatrix} 1 & 0 & 0 \\ 0 & \cos\phi & \sin\phi \\ 0 & -\sin\phi & \cos\phi \end{pmatrix} \begin{pmatrix} 0 \\ \dot{\theta} \\ 0 \end{pmatrix} + \begin{pmatrix} 1 & 0 & 0 \\ 0 & \cos\phi & \sin\phi \\ 0 & -\sin\phi & \cos\phi \end{pmatrix} \begin{pmatrix} \cos\theta & 0 & -\sin\theta \\ 0 & 1 & 0 \\ \sin\theta & 0 & \cos\theta \end{pmatrix} \begin{pmatrix} 0 \\ 0 \\ \dot{\psi} \end{pmatrix} \\
 \begin{pmatrix} p \\ q \\ r \end{pmatrix} &= \begin{pmatrix} 1 & 0 & -\sin\theta \\ 0 & \cos\phi & \sin\phi \cos\theta \\ 0 & -\sin\phi & \cos\phi \cos\theta \end{pmatrix} \begin{pmatrix} \dot{\phi} \\ \dot{\theta} \\ \dot{\psi} \end{pmatrix} \\
 \begin{pmatrix} \dot{\phi} \\ \dot{\theta} \\ \dot{\psi} \end{pmatrix} &= \begin{pmatrix} 1 & \sin\phi \tan\theta & \cos\phi \tan\theta \\ 0 & \cos\phi & -\sin\phi \\ 0 & \sin\phi \sec\theta & \cos\phi \sec\theta \end{pmatrix} \begin{pmatrix} p \\ q \\ r \end{pmatrix}
 \end{aligned} \tag{2.33}$$

Body axis rotation angle equation can be expanded as below.

$$\dot{\phi} = p + q\sin\phi \tan\theta + r\cos\phi \tan\theta \tag{2.34}$$

$$\dot{\theta} = q\cos\phi - r\sin\phi \tag{2.35}$$

$$\dot{\psi} = q\sin\phi \sec\theta + r\cos\phi \sec\theta \tag{2.36}$$

2.2.3.3. Body Axis Translational Velocity Equations

Applying Newton's second law, velocity components can be expressed in the terms of the forces that are acting on guided projectiles.

Newton's second law states that total net force equals to multiplication of mass and acceleration of the object.

$$\sum F = m a$$

Acceleration term can be also written as time derivative of velocity in earth frame as below (Beard and McLain, 2012).

$$\sum F = m \frac{dV}{dt_E}$$

Time derivative of the velocity in earth frame is defined by the velocity time derivative in body frame and cross product of angular velocity and velocity in body frame as below in (Beard and McLain, 2012).

$$\sum F = m \left(\frac{dV}{dt_b} + \underbrace{\omega \times V}_{a_r} \right) \quad (2.37)$$

Where F is the applied forces $F = \begin{pmatrix} f_x \\ f_y \\ f_z \end{pmatrix}$, V is the velocities in body frame $V = \begin{pmatrix} u \\ v \\ w \end{pmatrix}$ and ω is the angular velocities in body frame also $\omega = \begin{pmatrix} p \\ q \\ r \end{pmatrix}$ (Beard and McLain, 2012).

By substituting the vectors in equation 2.37, translational motion state variables can be expressed as below (Beard and McLain, 2012).

$$\begin{pmatrix} \dot{u} \\ \dot{v} \\ \dot{w} \end{pmatrix} = \begin{pmatrix} rv - qw \\ pw - ru \\ qu - pv \end{pmatrix} + \frac{1}{m} \begin{pmatrix} f_x \\ f_y \\ f_z \end{pmatrix} \quad (2.38)$$

Translational motion variables in equation 2.38 can be expanded, using the defined force equations 2.24, 2.25, 2.26 as below.

$$\dot{u} = rv - qw - g\sin\theta + \frac{\rho V^2 S}{2m} \left[C_X(\alpha) + C_{Xq}(\alpha) \frac{cq}{2V} + C_{X\delta_e}(\alpha) \delta_e \right] \quad (2.39)$$

$$\dot{v} = pw - ru + g\cos\theta\sin\phi + \frac{\rho V^2 S}{2m} \left[C_{Y0} + C_{Y\beta}\beta + C_{Yp} \frac{bp}{2V} + C_{Yr} \frac{br}{2V} + C_{Y\delta_a}\delta_a + C_{Y\delta_r}\delta_r \right] \quad (2.40)$$

$$\dot{w} = qu - pv + g\cos\theta\cos\phi + \frac{\rho V^2 S}{2m} \left[C_Z(\alpha) + C_{Zq}(\alpha) \frac{cq}{2V} + C_{Z\delta_e}(\alpha) \delta_e \right] \quad (2.41)$$

2.2.3.4. Body Axis Angular Velocity Equations

Rotational state variable can be defined using conservation of angular momentum principle (Beard and McLain, 2012; Matthew, Matthew).

$$\sum M = \frac{d H}{dt}$$

where H is the angular momentum and defined as,

$$H = I \omega_E \quad (2.42)$$

where I is the moment of inertia matrix and ω_E is the rotation vector.

Moment of inertia matrix is defined as below (Zipfel, 2007; Beard and McLain, 2012; Matthew, Matthew; Cook, 2007).

$$I = \begin{pmatrix} I_{xx} & -I_{xy} & -I_{xz} \\ I_{yx} & I_{yy} & -I_{yz} \\ -I_{zx} & -I_{zy} & I_{zz} \end{pmatrix}$$

However earth frame conservation of angular momentum have to be expressed in body frame as below.

$$\sum M = \frac{d}{dt} H + \omega \times H \quad (2.43)$$

and substitute the defined angular momentum in equation 2.42 to the equation 2.43.

$$\sum M = I \frac{d\omega}{dt} + \omega \times I \omega \quad (2.44)$$

The moment and angular velocity vectors are defined as $M = \begin{pmatrix} l \\ m \\ n \end{pmatrix}$ and

$\omega = \begin{pmatrix} p \\ q \\ r \end{pmatrix}$ respectively (Zipfel, 2007; Beard and McLain, 2012; Matthew, Matthew; Cook, 2007).

Expand equation 2.44 by substituting moment of inertia matrix, moment and angular velocity vectors as below.

$$\begin{pmatrix} l \\ m \\ n \end{pmatrix} = \begin{pmatrix} I_{xx} & -I_{xy} & -I_{xz} \\ I_{yx} & I_{yy} & -I_{yz} \\ -I_{zx} & -I_{zy} & I_{zz} \end{pmatrix} \begin{pmatrix} \dot{p} \\ \dot{q} \\ \dot{r} \end{pmatrix} + \begin{pmatrix} p \\ q \\ r \end{pmatrix} \times \begin{pmatrix} I_{xx} & -I_{xy} & -I_{xz} \\ I_{yx} & I_{yy} & -I_{yz} \\ -I_{zx} & -I_{zy} & I_{zz} \end{pmatrix} \begin{pmatrix} p \\ q \\ r \end{pmatrix} \quad (2.45)$$

For symmetric projectiles $I_{xy} = I_{yz} = 0$ and inverse of moment of inertia matrix can be defined as below.

$$I^{-1} = \frac{\begin{pmatrix} I_y I_z & 0 & I_y I_{xz} \\ 0 & I_x I_z - I_{xz}^2 & 0 \\ I_{xz} I_y & 0 & I_x I_y \end{pmatrix}}{I_x I_y I_z - I_{xz}^2 I_y} \quad (2.46)$$

$$I^{-1} = \begin{pmatrix} \frac{I_z}{\Gamma} & 0 & \frac{I_{xz}}{\Gamma} \\ 0 & \frac{1}{I_y} & 0 \\ \frac{I_{xz}}{\Gamma} & 0 & \frac{I_x}{\Gamma} \end{pmatrix} \quad (2.47)$$

where $\Gamma = I_x I_z - I_{xz}$.

Therefore, derivatives of angular velocities can be defined as below, rewriting the equation 2.44, using the equation 2.47.

$$\begin{aligned}
\begin{pmatrix} \dot{p} \\ \dot{q} \\ \dot{r} \end{pmatrix} &= I^{-1} \left[\begin{pmatrix} -p \\ -q \\ -r \end{pmatrix} \times I \begin{pmatrix} p \\ q \\ r \end{pmatrix} + \begin{pmatrix} l \\ m \\ n \end{pmatrix} \right] \\
\begin{pmatrix} \dot{p} \\ \dot{q} \\ \dot{r} \end{pmatrix} &= \begin{pmatrix} \frac{I_z}{\Gamma} & 0 & \frac{I_{xz}}{\Gamma} \\ 0 & \frac{1}{I_y} & 0 \\ \frac{I_{xz}}{\Gamma} & 0 & \frac{I_x}{\Gamma} \end{pmatrix} \left[\begin{pmatrix} 0 & r & -q \\ -r & 0 & p \\ q & -p & 0 \end{pmatrix} \begin{pmatrix} I_x & 0 & -I_{xz} \\ 0 & I_y & 0 \\ -I_{xz} & 0 & I_z \end{pmatrix} \begin{pmatrix} p \\ q \\ r \end{pmatrix} + \begin{pmatrix} l \\ m \\ n \end{pmatrix} \right] \\
\begin{pmatrix} \dot{p} \\ \dot{q} \\ \dot{r} \end{pmatrix} &= \begin{pmatrix} \Gamma_1 pq - \Gamma_2 qr \\ \Gamma_5 pr - \Gamma_6(p^2 - r^2) \\ \Gamma_7 pq - \Gamma_1 qr \end{pmatrix} + \begin{pmatrix} \Gamma_3 l + \Gamma_4 n \\ \frac{1}{I_y} m \\ \Gamma_4 l + \Gamma_8 n \end{pmatrix} \quad (2.48)
\end{aligned}$$

Longitudinal and lateral moment equations are defined in the equations 2.13, 2.22, 2.23. Body axis angular velocity equations can be expanded using the moment equations as below (Beard and McLain, 2012).

$$\dot{p} = \Gamma_1 pq - \Gamma_2 qr + \frac{1}{2} \rho V^2 Sb \times \left[C_{p_0} + C_{p_\beta} \beta + C_{p_p} \frac{bp}{2V} + C_{p_r} \frac{br}{2V} + C_{p_{\delta_a}} \delta_a + C_{p_{\delta_r}} \delta_r \right] \quad (2.49)$$

$$\dot{q} = \Gamma_5 pr - \Gamma_6(p^2 - r^2) + \frac{\rho V^2 Sc}{2I_y} \times \left[C_{m_0} + C_{m_\alpha} \alpha + C_{m_q} \frac{cq}{2V} + C_{m_{\delta_e}} \delta_e \right] \quad (2.50)$$

$$\dot{r} = \Gamma_7 pq - \Gamma_1 qr + \frac{1}{2} \rho V^2 Sb \times \left[C_{r_0} + C_{r_\beta} \beta + C_{r_p} \frac{bp}{2V} + C_{r_r} \frac{br}{2V} + C_{r_{\delta_a}} \delta_a + C_{r_{\delta_r}} \delta_r \right] \quad (2.51)$$

Definitions of the coefficients such as C_{p_0}, C_{r_0}, \dots and moment of inertia terms such as $\Gamma_1, \Gamma_2, \dots$ in the equations 2.49, 2.50 and 2.51 are given in the appendix E.

2.3. Control Input Combination

The Basic Finner Reference Projectile has four fin to alter the course of the munition. However, 6-DoF equation of motions are defined for standard rudder, elevator and aileron deflection angles. Therefore, δ_r , δ_e and δ_a have to be defined in terms of reference projectile fin combination. Standard rudder, elevator and aileron deflection angles in 6-DoF equations of motion can be rewritten in terms of reference projectile fin deflections δ_1 , δ_2 , δ_3 and δ_4 as follows.

$$\delta_a = \delta_2 + \delta_4$$

$$\delta_r = \delta_1 - \delta_3 \quad (2.52)$$

$$\delta_e = \delta_2 - \delta_4$$

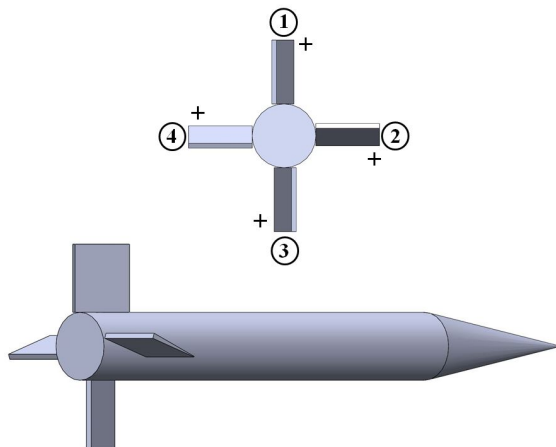


Figure 2.5. Fin Deflection Directions.

2.4. Summary of Six Degree of Freedom Equations of Motions

All of the six degree of freedom equations of motion can be summarized as below. In the equations below, there is 12 equations and variable in total.

Earth Axis Position Equations:

$$\begin{aligned} \dot{x}_E &= u(\cos\theta \cos\psi) + v(\sin\phi \sin\theta \cos\psi - \cos\phi \sin\psi) + w(\cos\phi \sin\theta \cos\psi + \sin\phi \sin\psi) \\ \dot{y}_E &= u(\cos\theta \sin\psi) + v(\sin\phi \sin\theta \sin\psi - \cos\phi \cos\psi) + w(\cos\phi \sin\theta \sin\psi + \sin\phi \cos\psi) \\ \dot{h} &= usin\theta - vsin\phi cos\theta - wcos\phi cos\theta \end{aligned}$$

Body Axis Rotation Angle Equations:

$$\begin{aligned} \dot{\phi} &= p + q\sin\phi \tan\theta + r\cos\phi \tan\theta \\ \dot{\theta} &= q\cos\phi - r\sin\phi \\ \dot{\psi} &= q\sin\phi \sec\theta + r\cos\phi \sec\theta \end{aligned}$$

Body Axis Translational Velocity Equations:

$$\begin{aligned} \dot{u} &= rv - qw - g\sin\theta + \frac{\rho V^2 S}{2m} \left[C_X(\alpha) + C_{Xq}(\alpha) \frac{cq}{2V} + C_{X\delta_e}(\alpha) \delta_e \right] \\ \dot{v} &= pw - ru + g\cos\theta \sin\phi + \frac{\rho V^2 S}{2m} \left[C_{Y_0} + C_{Y\beta}\beta + C_{Yp} \frac{bp}{2V} + C_{Yr} \frac{br}{2V} + \dots \right. \\ &\quad \left. \dots + C_{Y\delta_a} \delta_a + C_{Y\delta_r} \delta_r \right] \\ \dot{w} &= qu - pv + g\cos\theta \cos\phi + \frac{\rho V^2 S}{2m} \left[C_Z(\alpha) + C_{Zq}(\alpha) \frac{cq}{2V} + C_{Z\delta_e}(\alpha) \delta_e \right] \end{aligned}$$

Body Axis Angular Velocity Equations:

$$\begin{aligned} \dot{p} &= \Gamma_1 pq - \Gamma_2 qr + \frac{1}{2} \rho V^2 S b \times \left[C_{p_0} + C_{p\beta}\beta + C_{pp} \frac{bp}{2V} + C_{pr} \frac{br}{2V} + C_{p\delta_a} \delta_a + C_{p\delta_r} \delta_r \right] \\ \dot{q} &= \Gamma_5 pr - \Gamma_6 (p^2 - r^2) + \frac{\rho V^2 Sc}{2I_y} \times \left[C_{m_0} + C_{m\alpha}\alpha + C_{mq} \frac{cq}{2V} + C_{m\delta_e} \delta_e \right] \\ \dot{r} &= \Gamma_7 pq - \Gamma_1 qr + \frac{1}{2} \rho V^2 S b \times \left[C_{r_0} + C_{r\beta}\beta + C_{rp} \frac{bp}{2V} + C_{rr} \frac{br}{2V} + C_{r\delta_a} \delta_a + C_{r\delta_r} \delta_r \right] \end{aligned}$$

CHAPTER 3

CONTROL SYSTEM DESIGN OF GUIDED PROJECTILES

Control system of a plant can be defined using both transfer functions and state-space models, for the given requirements such as rise time, percent overshoot etc. However, sophisticated multi-input multi-output (MIMO) systems such as aircraft autopilots and autonomous cars inherently are evaluated better in state space models. Therefore, in this chapter a navigation system will be designed in a state space model for a guided projectile control system to reach a given set of waypoints, satisfying the design criteria.

The 6-DoF equations of motion are explained in the chapter 2. In 6-DoF equations, the aerodynamic parameters such as $C_L(\alpha)$ and $C_m(\alpha)$ are unique coefficients that are determined in wind tunnel tests or computer analyses for each aircraft or munition. As it can be inferred, such as key aerodynamic parameters for a state-of-the-art smart munition are confidential.

Even though several comprehensive studies carried out and some of the aerodynamic parameters are given for the most known experimental fin controlled projectile, the Basic Finner Reference Model, many critical coefficients such as pitch moment coefficient due to fin deflection $C_{m\delta}$ are not available (Albisser, 2015; Dupuis, 2002; Dupuis and Hathaway, 1997). Therefore, a published guided missile state space model (Mracek and Ridgely, 2005) instead of the basic finner reference model is used during the control system design and simulations. Although the dimensions of the published guided missile does not match up with basic finner reference model, due to similar flight regime such as total velocity and altitude, the published guided missile state space model is chosen.

3.1. State Space Model

Longitudinal motion of a missile dynamics are given in the study (Mracek and Ridgely, 2005) as below for the states, angle of attack and pitch rate.

$$\dot{x} = Ax + Bu$$

$$y = Cx + Du$$

where, x is the state vector $x = \begin{bmatrix} \alpha \\ q \end{bmatrix}$, y is the output vector $y = \begin{bmatrix} A_z \\ q \end{bmatrix}$ and the input u is the fin deflection, δ_p (Mracek and Ridgely, 2005). The matrices A , B , C and D are defined in (Mracek and Ridgely, 2005) as below.

$$A = \begin{bmatrix} \frac{1}{V_{m0}} \left[\frac{\bar{Q} S C_{z\alpha_0}}{m} - A_{x0} \right] & 1 \\ \frac{\bar{Q} S d C_{m\alpha_0}}{I_y} & 0 \end{bmatrix} \quad B = \begin{bmatrix} \frac{\bar{Q} S C_{z\delta p_0}}{m V_{m0}} \\ \frac{\bar{Q} S d C_{m\delta p_0}}{I_y} \end{bmatrix}$$

$$C = \begin{bmatrix} \frac{\bar{Q} S C_{z\alpha_0}}{m g} - \frac{\bar{Q} S d C_{m\alpha_0}}{g I_y} \bar{x} & 0 \\ 0 & 1 \end{bmatrix} \quad D = \begin{bmatrix} \frac{\bar{Q} S C_{z\delta p_0}}{m g} - \frac{\bar{Q} S d C_{m\delta p_0}}{g I_y} \bar{x} \\ 0 \end{bmatrix}$$

After substituting the numerical values of the variables given in (Mracek and Ridgely, 2005), The matrices A , B , C and D are evaluated as below.

$$A = \begin{bmatrix} -1.064 & 1 \\ 290.26 & 0 \end{bmatrix} \quad B = \begin{bmatrix} -0.25 \\ -331.4 \end{bmatrix}$$

$$C = \begin{bmatrix} -123.34 & 0 \\ 0 & 1 \end{bmatrix} \quad D = \begin{bmatrix} -13.51 \\ 0 \end{bmatrix}$$

The state space equation can be also written as below.

$$\begin{bmatrix} \dot{\alpha} \\ \dot{q} \end{bmatrix} = \begin{bmatrix} -1.064 & 1 \\ 290.26 & 0 \end{bmatrix} \begin{bmatrix} \alpha \\ q \end{bmatrix} + \begin{bmatrix} -0.25 \\ -331.4 \end{bmatrix} \delta_p \quad (3.1)$$

$$y = \begin{bmatrix} -123.34 & 0 \\ 0 & 1 \end{bmatrix} \begin{bmatrix} \alpha \\ q \end{bmatrix} + \begin{bmatrix} -13.51 \\ 0 \end{bmatrix} \delta_p$$

The state space equations which is defined in 3.1 is used for the navigation system design and model based simulations in the posterior sections.

Following assumptions are considered for the navigation system design.

- The state space model is linearized.
- Effect of lateral forces and moments are neglected.
- Body of the projectile is rigid.
- Weather conditions are constant.

3.1.0.1. Step Response of the Open-Loop Model

Open-loop model of the aforementioned state space model in the equations 3.1 is created as in the figure 3.4 and step response of the open loop model is shown in the figure 3.2.

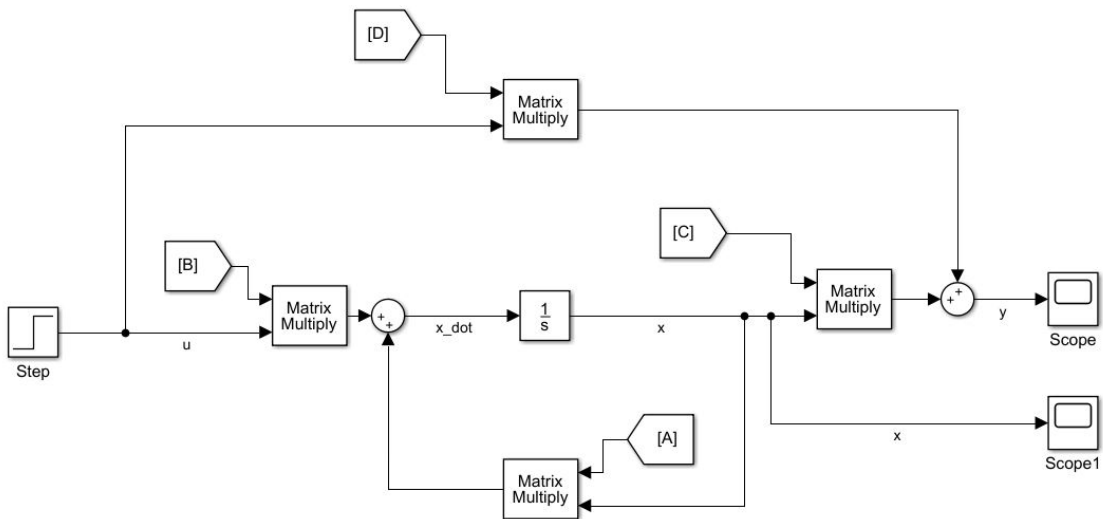


Figure 3.1. Open Loop Model

The open loop step response figures actually explain the underlying dynamics of the longitudinal motion of the system. The damping out, up and down motion is named as “phugoid mode” and it is the result of the negative pitch moment coefficient (Cook, 2007). When the positive fin deflection is applied, nose of the munition goes down and

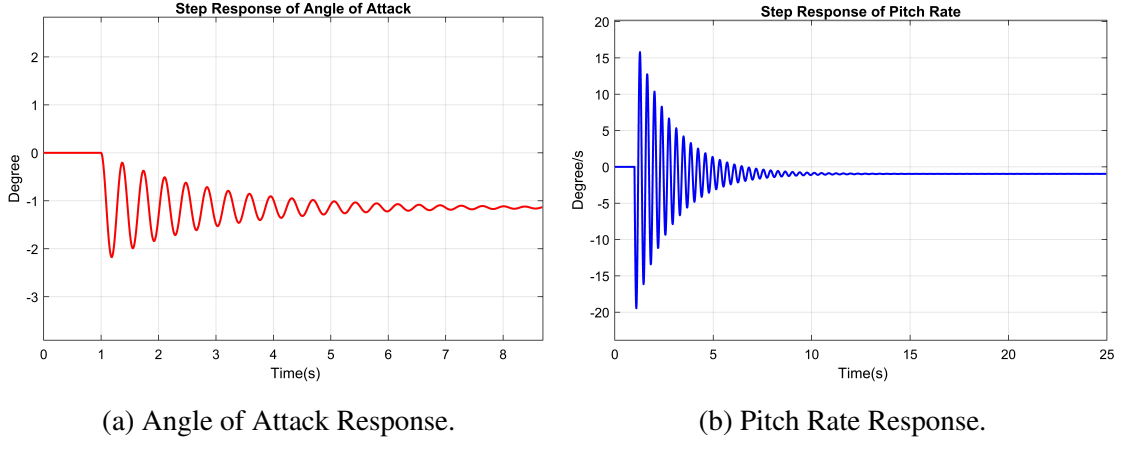


Figure 3.2. Open Loop Responses.

the total speed increases. After a while later, the lift force increase as a result of increased speed and the nose of the munition starts to ascend. Thereafter, the munition climbs for a certain altitude until gravitational force surpasses the lift force. This motion continues as damping out by time until a certain angle of attack and altitude.

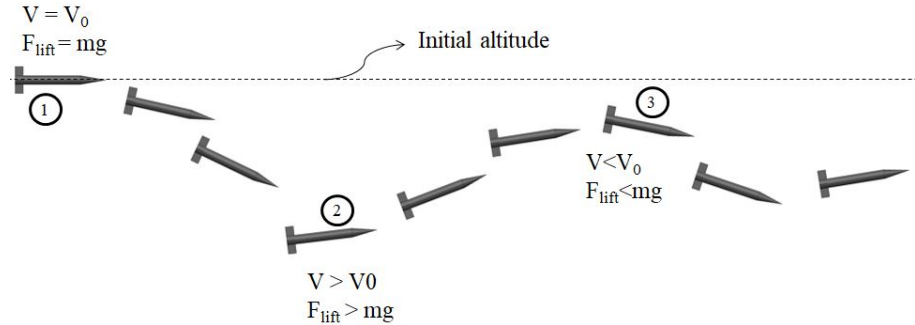


Figure 3.3. Phugoid Mode.

3.2. Navigation System Design

A control system for a plant have to be designed according the performance requirements while considering the physical limitations such as actuator bandwidth. Therefore, in this section a guided projectile navigation system performance requirements are determined referencing the similar previous studies in the field of guided munitions. Summary of the design criteria for different types of experimental guided projectiles and other

studies are shown in the table 3.1. Even though there is no unvarying natural frequency ω_n , it can be inferred from the table 3.1 that the damping ration is determined in overall such as between $0.66 < \zeta < 0.78$ for diffrent types of munition. Moreover, the bandwidth of the actuators always have to be considered during the parameter decision. It is stated that bandwidth of the actuators have to be five times larger than the phase margin crossover frequency or vice versa in (Bryson et al., 2020).

Depending on the munition type and operational requirements the bandwidth of the control surface actuators may change up to 250 rad/s ($\approx 40\text{Hz}$) (Tsourdos and White, 2005). Therefore, the performance criteria for the navigation system to be designed are determined as below, considering the studies that are shown in the table 3.1.

- $\zeta = 0.65$
- $T_s < 0.5\text{s}$
- $\omega_n > 10 \text{ rad/s}$
- P.O. $< 10\%$

It is aimed that the designed navigation system will maintain the given course for the projectile while satisfying the defined requirements. A guidance path is defined for the navigation system of the munition. According to that, the munition will maintain initial course for 5 seconds and then pitch up for 5 seconds at 5 degree flight path angle, then cruise in zero pitch for 10 seconds and finally pitch down for 5 seconds at -5 degree flight path angle.

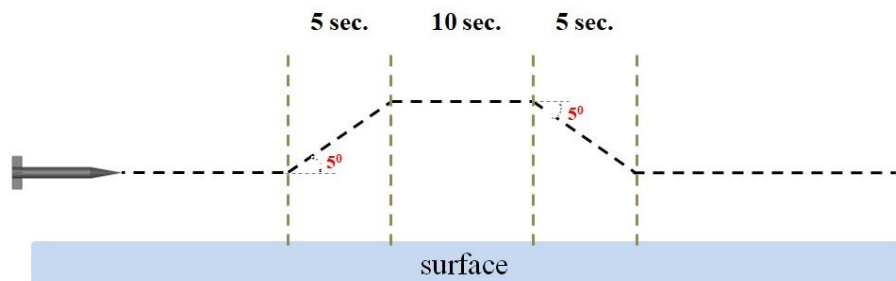


Figure 3.4. Guidance Path for Simulation.

Preset guidance method is performed in this navigation system. The target data and calculated flight path for munition are loaded into the control system just before

Table 3.1. Design Criteria for Guided Munitions in Reference Studies.

| Reference Study | Design Criteria | Plant (Munition Type) |
|------------------------------|---|--|
| (Gruenwald et al., 2018) | 65.4 phase margin at 7.95 Hz crossover frequency | Generic Hypersonic Vehicle |
| (Gruenwald and Bryson, 2020) | 62.3 phase margin at 4.35 rad/s crossover frequency 25Hz bandwidth actuator | Basic Finner Reference Model |
| (Gruenwald et al., 2020) | 10 rad/s actuator bandwidth 65.4 phase margin 7.95 crossover frequency | Hypersonic Vehicle |
| (Xu et al., 2018) | $\zeta = 0.7$ damping | Gun-Launched Gliding Projectile |
| (Thai et al., 2019) | $\zeta = 0.781$ Phase margin >35 Gain margin $> 6\text{dB}$ | Canard Guided Dual-Spin Projectile |
| (Bryson and Fresconi, 2018b) | $\zeta = 0.781$ $\omega_n = 39.525 \text{ rad/s}$ | High-Maneuverability Airframe (HMA) |
| (Bryson and Fresconi, 2018a) | $\zeta = 0.66$ $\omega_n = 193 \text{ rad/s}$ $T_r = 0.01067\text{s}$ $T_s = 0.0314\text{s}$ | High-Maneuverability Airframe (HMA) |

the launch. Therefore, highly maneuverable targets such as aircraft may easily dodge incoming munitions that are using preset guidance. However, the flight time and the range of a guided projectile and the maneuverability of naval vessels are considered, it can be concluded that guided projectiles can be highly precise and lethal option against naval surface platforms and stationary land targets.

Before establishing control system, controllability and observability analyses will be carried out for the aforementioned state space equation in the following sections.

3.2.1. Controllability Analysis

A system can be defined as controllable if all of outputs can be manipulated by the inputs, in very brief. In the control system books controllability is defined as,

“A system is completely controllable if there exists an unconstrained control $u(t)$ that can transfer any initial state $x(t_0)$ to any other desired location $x(t)$ in a finite time, $t_0 \leq t \leq T$.” (Dorf and Bishop, 2011).

The controllability matrix is defined in (Ogata, 2010; Dorf and Bishop, 2011; Nise, 2020) as below.

$$P_c = \begin{bmatrix} B & AB & A^2B & \dots & A^{n-1}B \end{bmatrix} \quad (3.2)$$

where, A is a $n \times n$ matrix and B is $n \times m$ matrix (m number of inputs). If the rank of P_c is n , the system is complete controllable (Ogata, 2010; Dorf and Bishop, 2011; Nise, 2020). Controllability is an important aspect to replace the poles and zeros of the system for reaching given requirements. Otherwise, the feedback gain of the close loop controller could not be determined. Therefore, controllability of the state space equations in the equation 3.1 have to be checked.

Substitute the state space matrices which are defined in 3.1 to controllability matrix, then P_c becomes,

$$P_c = \begin{bmatrix} -0.25 & -331.124 \\ -331.39 & 72.565 \end{bmatrix}$$

Determinant of P_c equals to,

$$\det(P_c) = -109749.32$$

and rank of P_c is,

$$\text{rank}(P_c) = 2$$

Hence it is showed that the defined state-space model is completely controllable.

3.2.2. Observability Analysis

Observability term can be expressed as if all state variables are effecting the output, then the system can be defined as complete observable. In the book definition observability is defined as,

“A system is completely observable if and only if there exists a finite time T such that the initial state $x(0)$ can be determined from the observation history $y(t)$ given the control $u(t)$, $0 \leq t \leq T$ ”.

The observability matrix is defined in (Dorf and Bishop, 2011) as below.

$$P_O = \begin{bmatrix} C \\ CA \\ \vdots \\ CA^{n-1} \end{bmatrix} \quad (3.3)$$

where, A is a $n \times n$ matrix and C is a $m \times n$ matrix. If the rank of P_O is n , then it can be said that the system is completely observable (Nise, 2020).

Observability matrix of the system can be formed, substituting the state space matrices which are defined in the equations 3.1 to the observability matrix as below.

$$P_O = \begin{bmatrix} -123.34 & 0 \\ 0 & 1 \\ 131.2338 & -123.34 \\ -290.26 & 0 \end{bmatrix} \quad (3.4)$$

Rank of the P_O is,

$$\text{rank}(P_O) = 2$$

Therefore it is showed that the state space model is completely observable.

3.2.3. Navigation System with Pole Placement Method

In this section a navigation system will be designed with pole placement method while satisfying the requirements which are defined in the 3.2. Previously, it is showed in the sections 3.2.1 and 3.2.2 that the state space equation of the system is completely controllable and observable. Therefore, the poles of the state space equation can be placed in the desired location. Open loop and desired close loop poles of the system are shown in the figure 3.5.

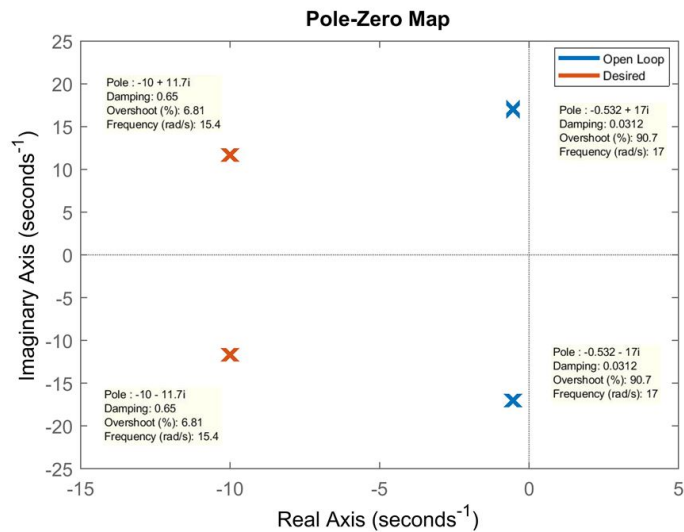


Figure 3.5. Poles of Open Loop and Desired Close Loop

Desired poles of the close loop system is defined choosing the damping ratio of the system as $\zeta = 0.65$ and settling time as $T_s = 0.4s$. After adjusting that parameters, natural frequency is calculated from the formula below (Dorf and Bishop, 2011).

$$T_s = \frac{4}{\zeta \omega_n}$$

$$0.4 = \frac{4}{0.65 \omega_n}$$

$$\omega_n = 15.38 \text{ rad/s}$$

The locations of the desired poles are,

$$s_1 = -9.997 + 11.687i$$

$$s_2 = -9.997 - 11.687i$$

It is seen that the calculated natural frequency and damping ratio meet the defined performance criteria.

Block diagram of the full state feedback controller with pole placement method is shown in the figure 3.6.

The desired characteristic equation for the determined poles is,

$$\Delta = s^2 + 19.994s + 236.526$$

The full state feedback controller gain \mathbf{K} is calculated using Ackerman's formula as below (Ogata, 2010).

$$\mathbf{K} = \begin{bmatrix} 0 & 1 \end{bmatrix} \begin{bmatrix} B & AB \end{bmatrix}^{-1} \phi(\mathbf{A}) \quad (3.5)$$

where, $\phi(\mathbf{A}) = A^2 + \alpha_1 A + \alpha_2$ and α_1, α_2 are the coefficients of the desired characteristic equation. Substitute the coefficients of the desired characteristic equation to $\phi(\mathbf{A})$.

$$\phi(\mathbf{A}) = A^2 + 19.994A + 236.526I$$

State space matrices and $\phi(\mathbf{A})$ can be substituted in the equation 3.5 as below (Ogata, 2010).

$$\mathbf{K} = \begin{bmatrix} 0 & 1 \end{bmatrix} \left[\begin{bmatrix} -0.25 \\ -331.4 \end{bmatrix} : \begin{bmatrix} -1.064 & 1 \\ 290.26 & 0 \end{bmatrix} \begin{bmatrix} -0.25 \\ -331.4 \end{bmatrix} \right]^{-1} \phi(\mathbf{A})$$

$$\mathbf{K} = \begin{bmatrix} 0 & 1 \end{bmatrix} \begin{bmatrix} -0.25 & -331.66 \\ -331.4 & 72.565 \end{bmatrix}^{-1} \left(A^2 + 19.994A + 236.526I \right)$$

$$\begin{aligned}
\mathbf{K} &= \begin{bmatrix} 0 & 1 \end{bmatrix} \begin{bmatrix} -0.0007 & -0.003 \\ -0.003 & 0 \end{bmatrix} \left(\begin{bmatrix} -289.1279 & -1.064 \\ 308.8366 & -290.26 \end{bmatrix} + \begin{bmatrix} -21.3 & 20 \\ -5803.5 & 0 \end{bmatrix} + 236.526I \right) \\
\mathbf{K} &= \begin{bmatrix} 0 & 1 \end{bmatrix} \begin{bmatrix} -0.0007 & -0.003 \\ -0.003 & 0 \end{bmatrix} \begin{bmatrix} -73.9 & 18.9 \\ -5494.6 & -53.7 \end{bmatrix} \\
\mathbf{K} &= \begin{bmatrix} 0 & 1 \end{bmatrix} \begin{bmatrix} 16.6261 & 0.1496 \\ 0.2105 & -0.0573 \end{bmatrix} \\
\mathbf{K} &= \begin{bmatrix} 0.2105 & -0.0573 \end{bmatrix}
\end{aligned} \tag{3.6}$$

The full state feedback gain \mathbf{K} found as in equation 3.6. Outputs of the full state feedback controller with pole placement method is shown in the figure 3.7.

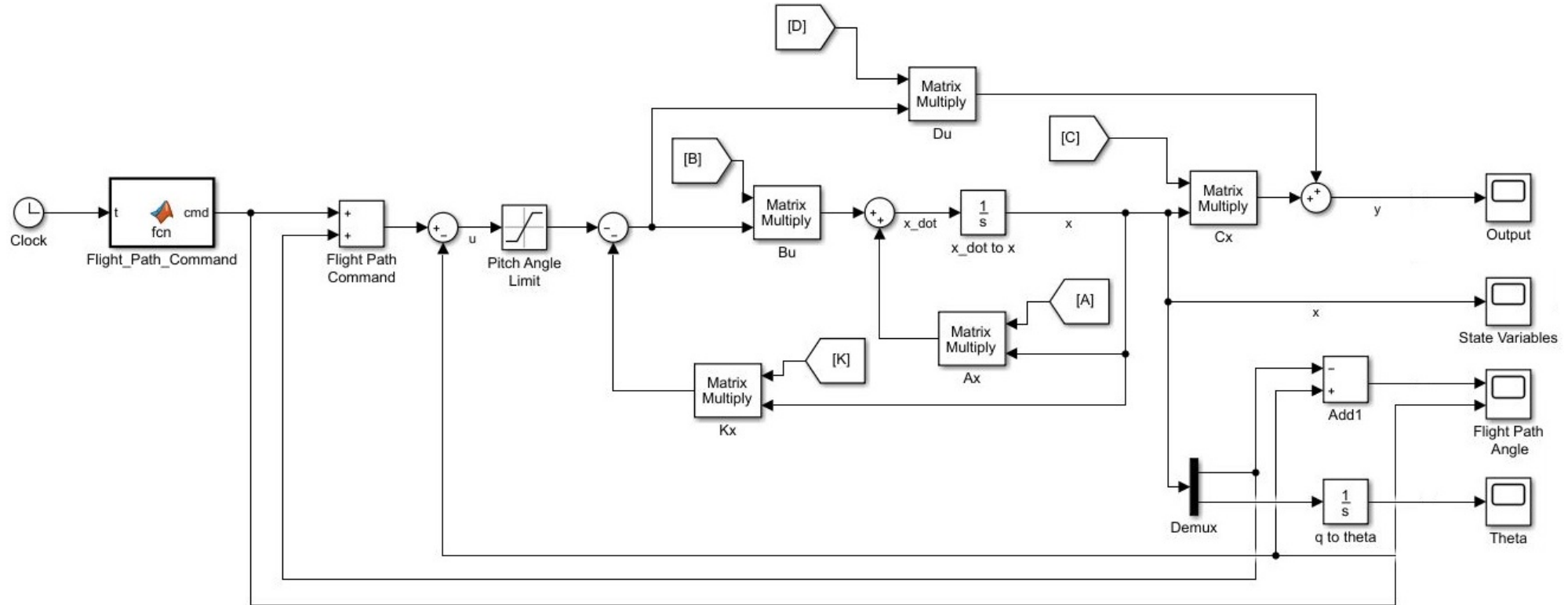
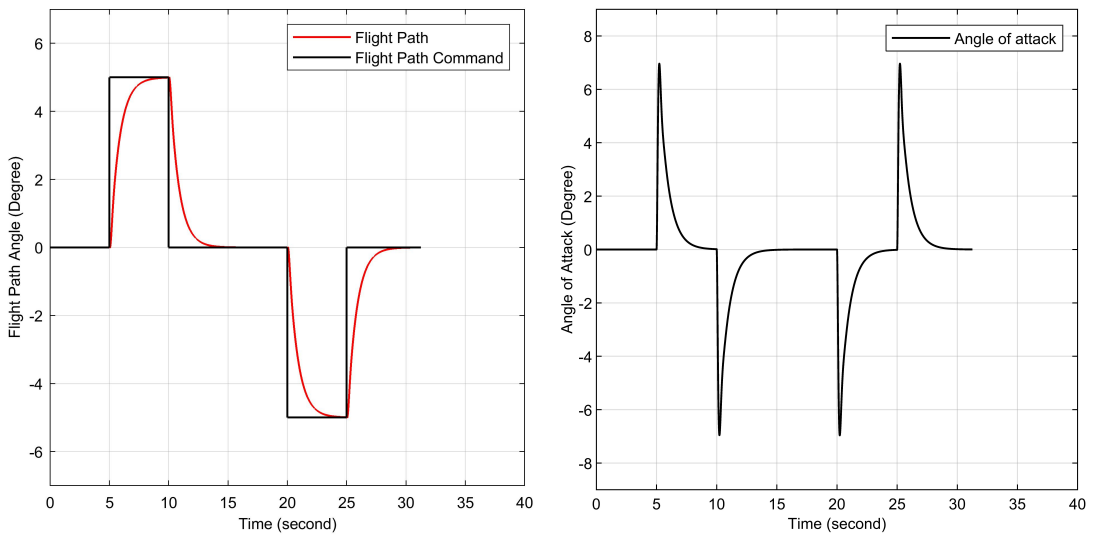
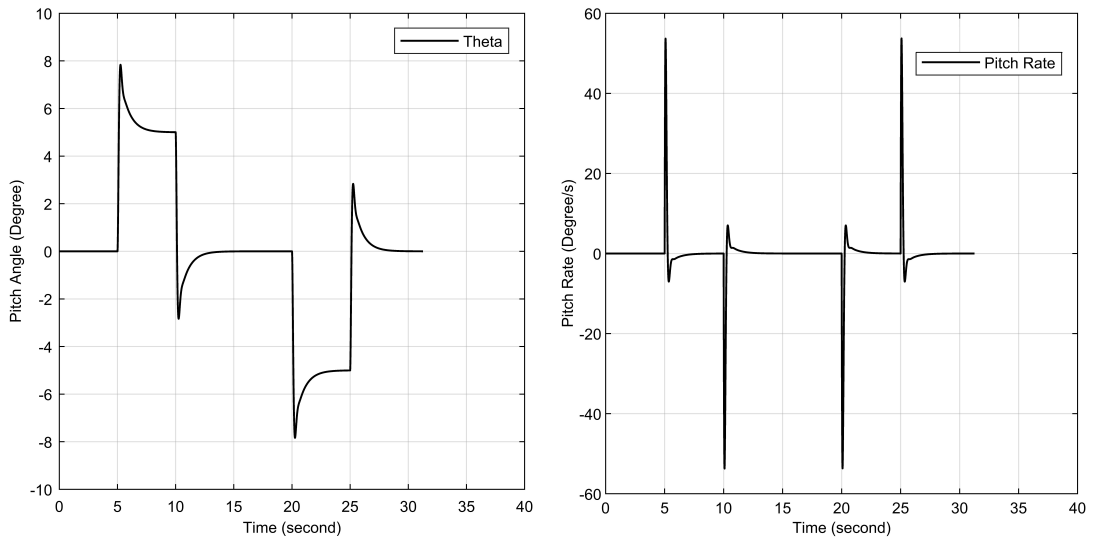


Figure 3.6. Full State Feedback Controller Block Diagram.



(a) Flight Path Output.

(b) Angle of Attack Output.



(c) Pitch Angle Output

(d) Pitch Rate Output.

Figure 3.7. Responses of Pole Placement Method.

3.2.4. Navigation System with Linear Quadratic Regulator

In this section a navigation system is proposed for the state space equation which is defined in equation 3.1 using linear quadratic regulator (LQR) methodology. If a controller has zero or a constant input, that system is defined as a regulator (Ogata, 2010). Despite pole placement method, the effort or the cost of control energy is aimed to be minimized in LQR controller. The performance index or the cost function for a LQR controller is defined as below (Ogata, 2010).

$$J = \int_0^{\infty} \left(x^T Q x + u^T R u \right) dt \quad (3.7)$$

where $u(t) = -\mathbf{K}x(t)$ is the control input and \mathbf{Q} and \mathbf{R} positive definite Hermitian or real symmetric matrices, penalizing the error in the state vectors and the control effort respectively (Ogata, 2010).

The close loop feedback gain \mathbf{K} is calculated using the formula below (Ogata, 2010).

$$K = R^{-1} B^T P \quad (3.8)$$

where, matrix \mathbf{P} is a positive definite matrix and calculated from the equation below (Ogata, 2010).

$$A^T P + P A - P B R^{-1} B^T P + Q = 0 \quad (3.9)$$

The equation 3.9 is also named as Riccati equation. The solution of Riccati equation have to satisfy a constraint that eigenvalues of $(\mathbf{A}-\mathbf{B}\mathbf{K})$ must have negative parts or by other words $(\mathbf{A}-\mathbf{B}\mathbf{K})$ must be a stable matrix (Ogata, 2010).

Since there is no rule for how to determine the penalizing matrices \mathbf{Q} and \mathbf{R} , the most preferred method is to start with diagonal identity or known predefined matrices for both of them. After that \mathbf{Q} and \mathbf{R} are tweaked until desired output is achieved.

The full state feedback gain \mathbf{K} can be calculated as below for $\mathbf{Q} = \begin{bmatrix} 1 & 0 \\ 0 & 1 \end{bmatrix}$ and $\mathbf{R} = 10$. The state space matrices \mathbf{A} and \mathbf{B} are substituted into the equation 3.9 to find the matrix \mathbf{P} .

$$\begin{bmatrix} -1.064 & -290.26 \\ 1 & 0 \end{bmatrix} \begin{bmatrix} p_{11} & p_{12} \\ p_{21} & p_{22} \end{bmatrix} + \begin{bmatrix} p_{11} & p_{12} \\ p_{21} & p_{22} \end{bmatrix} \begin{bmatrix} -1.064 & 1 \\ -290.26 & 0 \end{bmatrix} - \dots$$

$$\dots \begin{bmatrix} p_{11} & p_{12} \\ p_{21} & p_{22} \end{bmatrix} \begin{bmatrix} -0.25 \\ -331.4 \end{bmatrix} \begin{bmatrix} 10 \end{bmatrix} \begin{bmatrix} p_{11} & p_{12} \\ p_{21} & p_{22} \end{bmatrix} + \begin{bmatrix} 1 & 0 \\ 0 & 1 \end{bmatrix} = 0$$

The matrix \mathbf{P} can be found as below.

$$P = \begin{bmatrix} 2.2032 & -0.0069 \\ -0.0069 & 0.0095 \end{bmatrix}$$

The full state feedback gain \mathbf{K} can be calculated, substituting the matrices \mathbf{P} , \mathbf{R} and \mathbf{B} into the equation 3.8 as below.

$$K = \begin{bmatrix} 10 \end{bmatrix} \begin{bmatrix} -0.25 & -331.4 \end{bmatrix} \begin{bmatrix} 2.2032 & -0.0069 \\ -0.0069 & 0.0095 \end{bmatrix}$$

The full state feedback gain \mathbf{K} can be found as below.

$$K = \begin{bmatrix} 0.1725 & -0.3140 \end{bmatrix}$$

Eigenvalues of $(A - BK)$ have to be checked whether have negative real parts.

$$eig \left\{ \begin{bmatrix} -1.064 & 1 \\ -290.26 & 0 \end{bmatrix} - \begin{bmatrix} -0.25 \\ -331.4 \end{bmatrix} \begin{bmatrix} 0.1725 & -0.3140 \end{bmatrix} \right\}$$

$$\lambda_1 = -3.1492$$

$$\lambda_2 = -101.9475$$

It is showed that eigenvalues of $(A - BK)$ have negative real parts.

Since the feedback, $u = -Kx$, is same for both method, calculated full state feedback gain \mathbf{K} can be used in the same block diagram with pole placement method which is in the figure 3.6.

Output of the navigation system with LQR controller using the penalizing matrices $Q = \begin{bmatrix} 1 & 0 \\ 0 & 1 \end{bmatrix}$ and $R = 10$ are shown in the figure 3.9.

The effect of different penalizing matrices can be shown in the figure 3.8 using the following values for the same 7 degree flight path input.

$$Q_1 = \begin{bmatrix} 1 & 0 \\ 0 & 1 \end{bmatrix}, R_1 = 1000$$

$$Q_2 = \begin{bmatrix} 1 & 0 \\ 0 & 100 \end{bmatrix}, R_2 = 1000$$

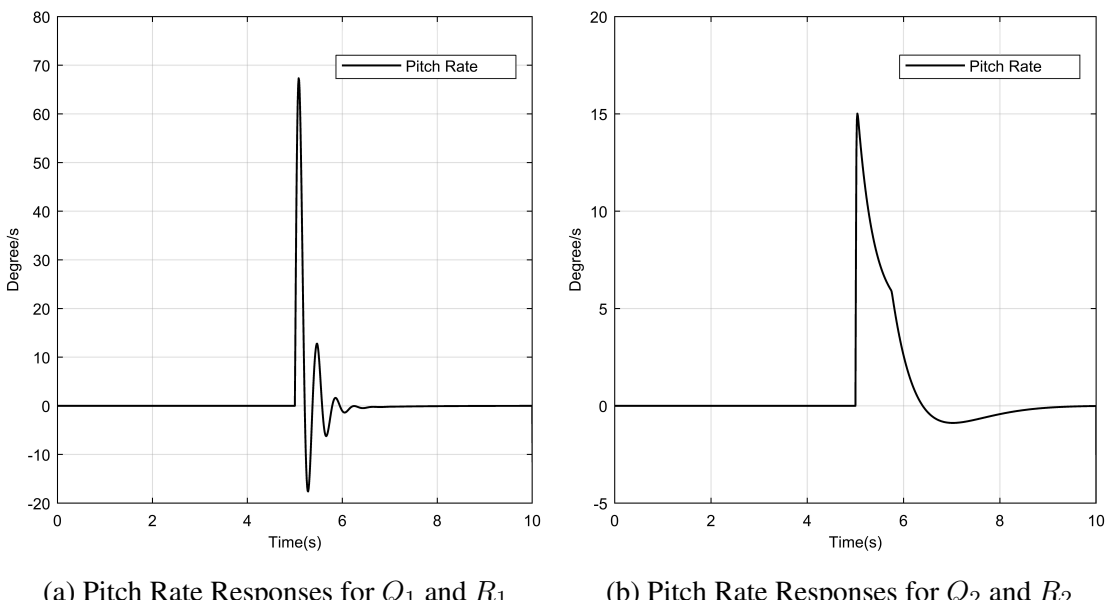


Figure 3.8. Pitch Rate Responses of Different Penalizing Matrices.

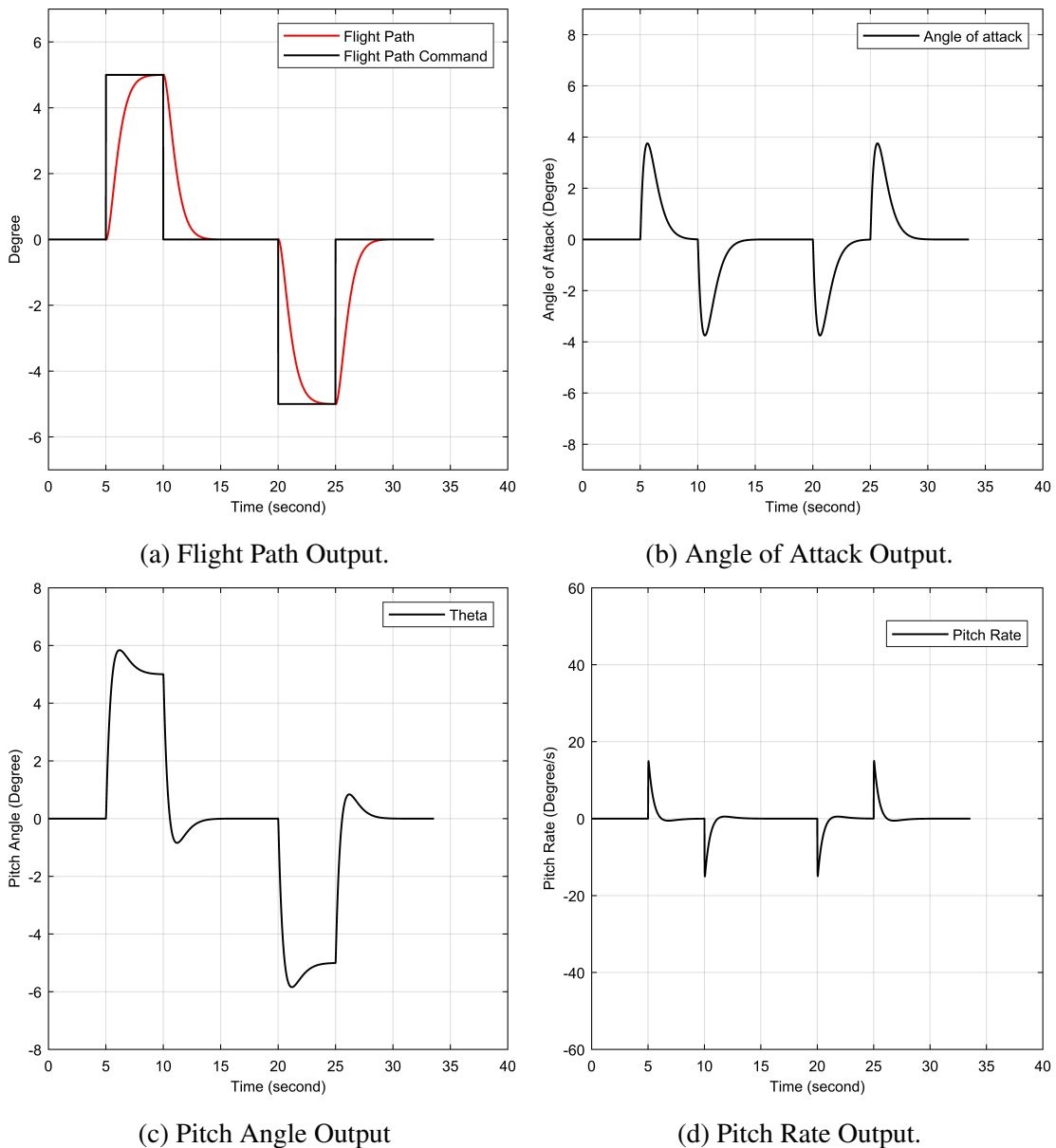


Figure 3.9. Responses of LQR.

3.2.5. Navigation System with Observer

In this section an observer for the states of the munition dynamic system is going to be established. The state variables of the dynamic systems are not always available due to noisy measurement environment, sensor expenses or inapplicability of the sensor placement. Therefore, it may be required that the state variables have to be estimated. The state space model of the munition in the equation 3.1 is modified to establish an observer since the observability matrix P_O is not an invertible matrix. The state space model that will be used in observer is modified as in the equation 3.10.

$$\dot{x} = Ax + Bu$$

$$y = Cx + Du$$

$$A = \begin{bmatrix} -1.064 & 1 \\ 290.26 & 0 \end{bmatrix} \quad B = \begin{bmatrix} -0.25 \\ -331.4 \end{bmatrix}$$

$$C = \begin{bmatrix} 0 & 1 \end{bmatrix} \quad D = \begin{bmatrix} 0 \end{bmatrix}$$

$$\begin{bmatrix} \dot{\alpha} \\ \dot{q} \end{bmatrix} = \begin{bmatrix} -1.064 & 1 \\ 290.26 & 0 \end{bmatrix} \begin{bmatrix} \alpha \\ q \end{bmatrix} + \begin{bmatrix} -0.25 \\ -331.4 \end{bmatrix} \delta_p$$

$$y = \begin{bmatrix} 0 & 1 \end{bmatrix} \begin{bmatrix} \alpha \\ q \end{bmatrix} \quad (3.10)$$

Modified state space model have to be checked for observability as follows.

$$P_{O_m} = \begin{bmatrix} C \\ CA \end{bmatrix}$$

$$P_{O_m} = \begin{bmatrix} 0 & 1 \\ -290.26 & 0 \end{bmatrix}$$

$$\text{rank}(P_{O_m}) = 2$$

It is showed that the modified state space model is also complete observable since observability matrix is a full rank matrix. Therefore, a full-state observer can be established for the defined state space model.

An observer of the system is actually a duplicate of the a priori model and estimated states are defined as below (Ogata, 2010).

$$\dot{\hat{x}} = A\hat{x} + Bu + Ke(y - C\hat{x}) \quad (3.11)$$

Simulink block diagram for the observer can be modeled as in the figure 3.10.

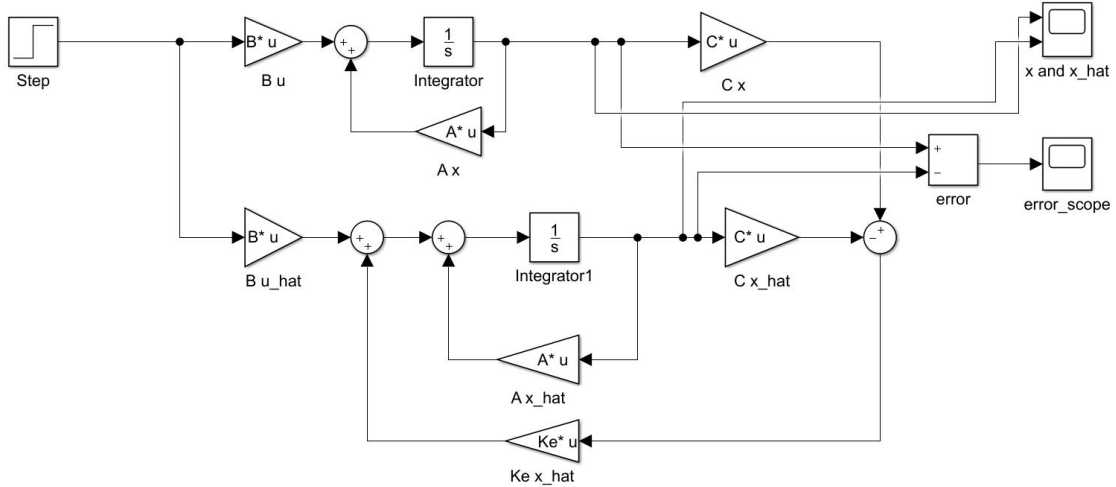


Figure 3.10. Full-state Observer Block Diagram

The one of the key parameters in observer design is to determine the observer gain Ke . The observer gain Ke is calculated similar to the pole placement method. Observer poles have to be placed as at least two times faster than the controller poles (Ogata, 2010). Hence, desired observer poles are determined as $s_1 = -19.994 + 23.37i$ and $s_2 = -19.994 - 23.37i$ and desired characteristic equation for observer becomes

$s^2 + 39,988s + 945.916$. The observer gain Ke can be calculated following formula as below (Ogata, 2010).

$$Ke = \phi(\mathbf{A}) \begin{bmatrix} \mathbf{C} \\ \mathbf{CA} \end{bmatrix}^{-1} \begin{bmatrix} 0 \\ 1 \end{bmatrix}$$

where, $\phi(\mathbf{A}) = \mathbf{A}^2 + 39.988\mathbf{A} + 945.916\mathbf{I}$

$$Ke = \phi(\mathbf{A}) \begin{bmatrix} 0 & 1 \\ -290.26 & 0 \end{bmatrix}^{-1} \begin{bmatrix} 0 \\ 1 \end{bmatrix}$$

$$Ke = \phi(\mathbf{A}) \begin{bmatrix} 0 & -0034 \\ 1 & 0 \end{bmatrix} \begin{bmatrix} 0 \\ 1 \end{bmatrix}$$

$$\begin{aligned} Ke &= \left\{ \begin{bmatrix} -1.064 & 1 \\ 290.26 & 0 \end{bmatrix}^2 + 39.988 \begin{bmatrix} -1.064 & 1 \\ 290.26 & 0 \end{bmatrix} + 945.916 \begin{bmatrix} 1 & 0 \\ 0 & 1 \end{bmatrix} \right\} \begin{bmatrix} -0034 \\ 0 \end{bmatrix} \\ Ke &= \begin{bmatrix} -2.1162 \\ 38.9240 \end{bmatrix} \end{aligned} \quad (3.12)$$

Finally the observer gain Ke is calculated as in the equation 3.12. Error convergence of the designed observer is shown as starting observer and the plant with different initial conditions.

- Plant initial conditions $x(0) = \begin{bmatrix} 0 \\ 0 \end{bmatrix} \begin{bmatrix} \alpha \\ q \end{bmatrix}$
- Observer initial conditions $\hat{x}(0) = \begin{bmatrix} 5 \\ 5 \end{bmatrix} \begin{bmatrix} \alpha \\ q \end{bmatrix}$

Results of designed observer are shown in the figure 3.11 and the error convergence of the states are shown in the figure 3.12. It is seen that both states converge in less than 0.4 seconds.

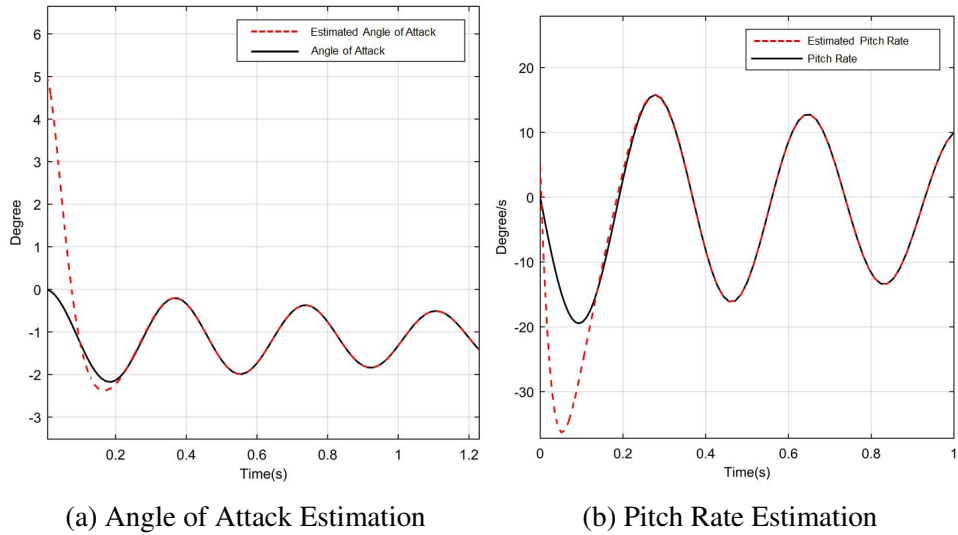


Figure 3.11. Results of Designed Observer

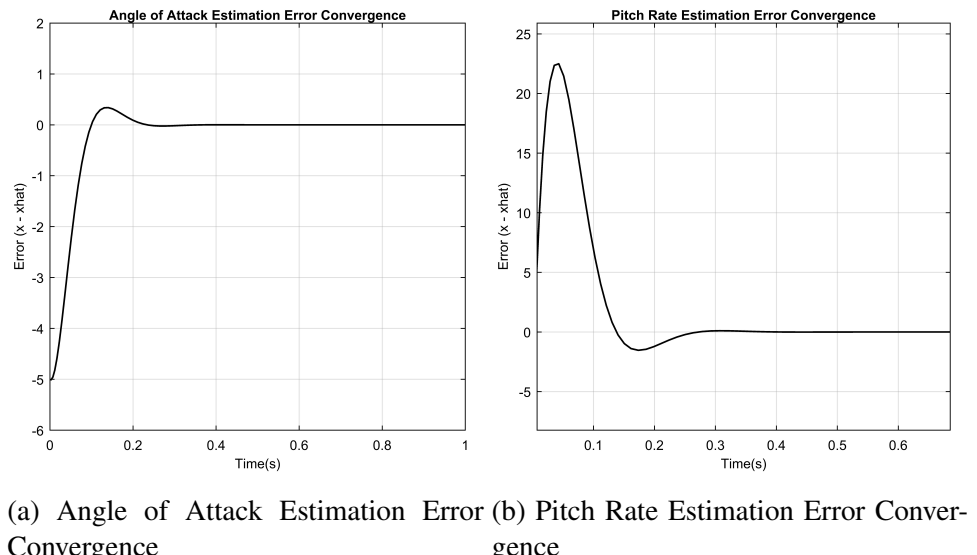


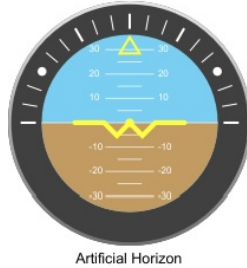
Figure 3.12. Error Convergence Designed Observer

3.2.6. Navigation System Simulation with FlightGear and Simulink

A navigation system simulation is generated using MATLAB & Simulink and a open source flight simulation software FlightGear v3.0. Indicators and simulation block for FlightGear from aerospace blockset are also used in the simulation block diagram.

The FlightGear simulation block requires six input latitude, longitude, altitude, roll, pitch and yaw. Since the munition state space is defined in body axis, latitude, longitude and altitude data have to be derived from the related velocity components of the state space equation.

For the reason that the state space for munition is defined only for longitudinal motion, position of the munition does not change in y-axis and roll and yaw angles are fixed to zero. Hence, x-axis position can be obtained using the integral of the velocity in the same axis with respect to flight path angle. The altitude can be also calculated from the double integrating z-axis acceleration data from the output of the state space. Flat earth to LLA block requires reference initial altitude also. Therefore, initial constant 1000ft is supplied to the block. Complete system block diagram and simulation block subsystem are shown in the figure 3.13 and 3.14 respectively. MATLAB code, Simulink model and FlightGear files are also attached to the appendix F.



Artificial Horizon



Altimeter

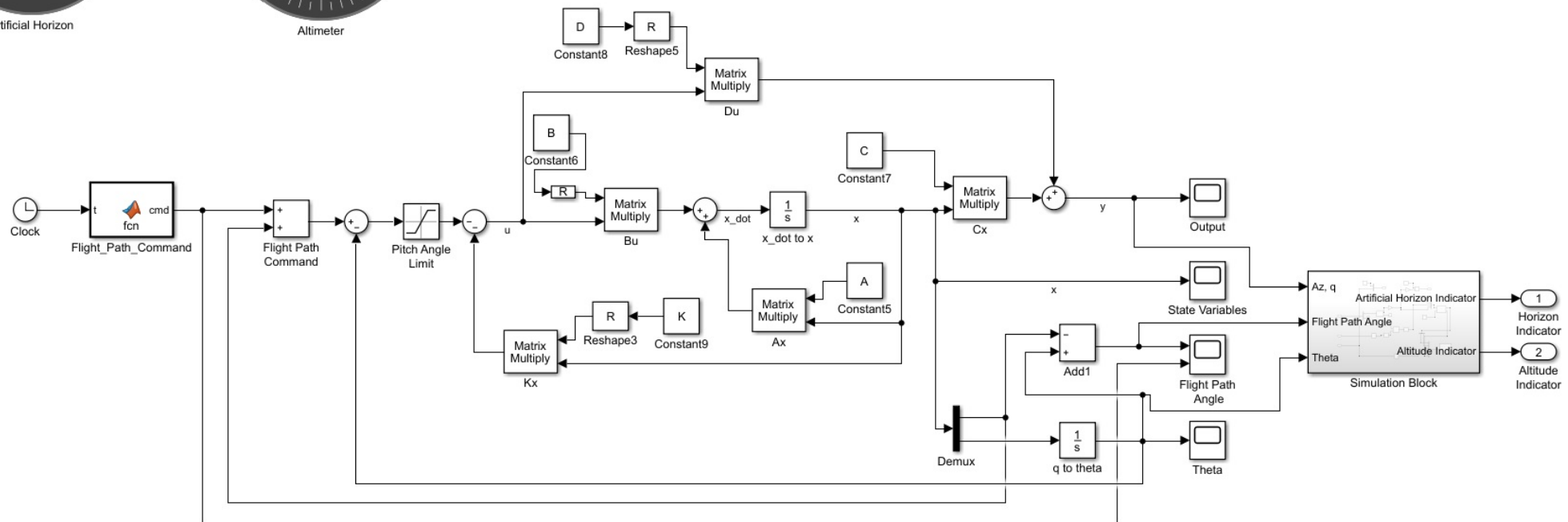


Figure 3.13. Complete System Block Diagram.

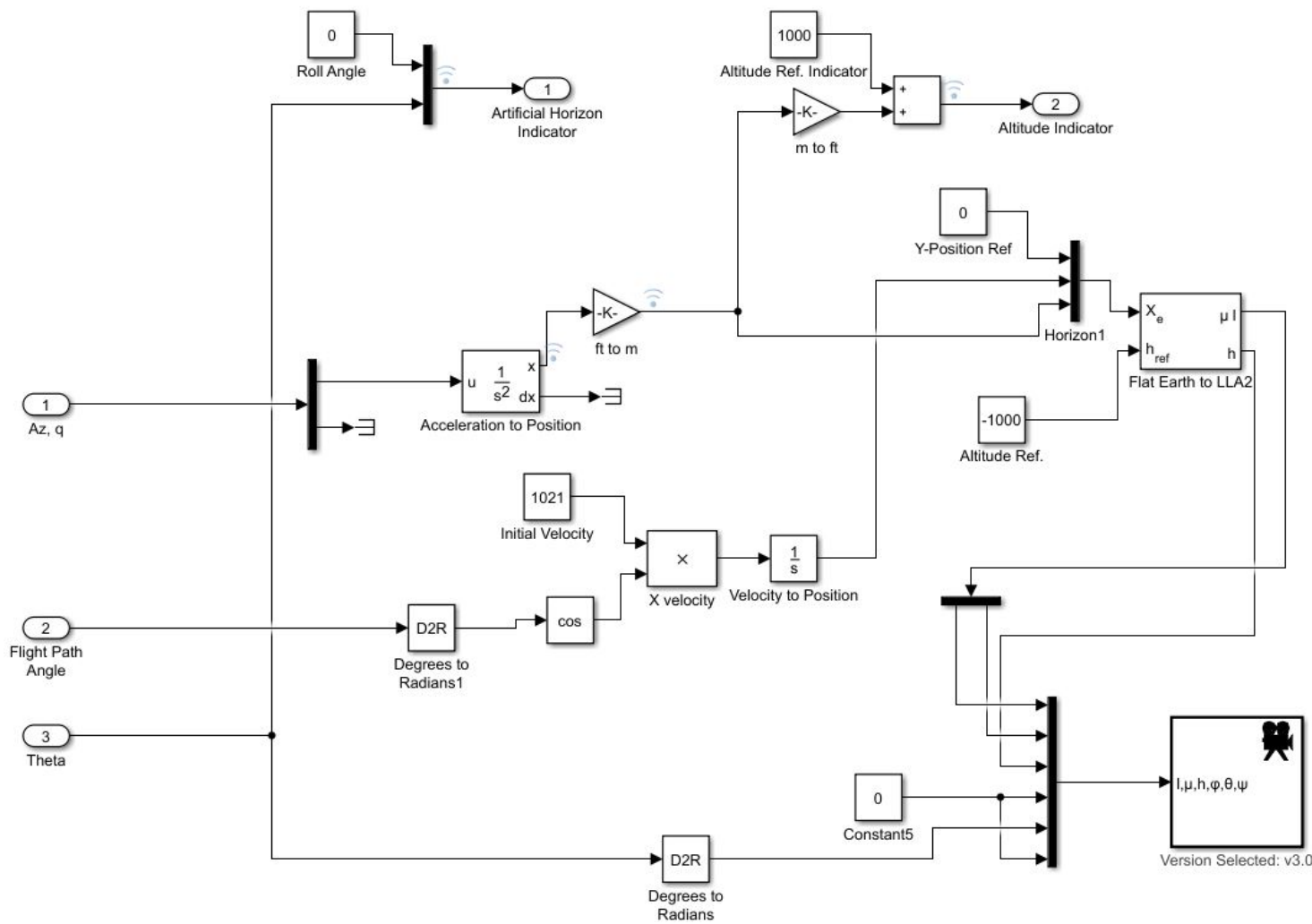


Figure 3.14. Simulation Block Subsystem

CHAPTER 4

COMPUTATIONAL FLUID ANALYSIS OF REFERENCE MODEL

In this chapter CFD analysis of the basic finner reference projectile model was carried out at lower launch velocities. Since some of the aerodynamic coefficients of the model have already published in the literature for supersonic flight velocities (Dupuis and Hathaway, 1997; Dupuis, 2002; Albisser, 2015), the aerodynamic characteristics of the lower launch velocity capable systems such as catapult or airguns have to be revealed for small size lab experiments. Therefore, the aerodynamic coefficients C_L , C_D and C_M were calculated at $40m/s$ flight velocity. RANS based $k - \epsilon$ model is selected because of the turbulence air flow and less computational time required for simulations.

The basic finner reference model is selected as reference geometry. Main reason of this selection is that this reference geometry is a commonly used model in many studies and all of its dimensions are already available (Dupuis and Hathaway, 1997). Besides, aerodynamic coefficients such as drag coefficient, lift coefficient and pitching moment are easy to calculate by using CFD software. In this chapter ANSYS Fluent 2019R3 (Academic) CFD software is used for simulations.

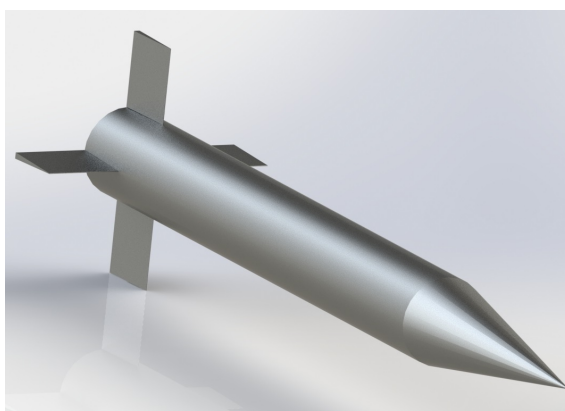


Figure 4.1. Basic Finner Reference Model (Source: Dupuis and Hathaway (1997)).

There are several approaches to analyze fluid dynamics of objects such as Direct Numerical Simulation (DNS), Large Eddy Simulation (LES) and Reynolds Averaged

Navier-Stokes Simulation (RANS). Because of less computational time required, RANS approach is preferred at the first step.

In the literature there is some related works on CFD analysis of guided munitions. Y. Chen et al. studied on a canard guided missile and investigated the effects of various canard configurations at 0.8 to 3.5 Mach numbers. Reynolds Averaged Navier Stokes (RANS) equations and SST $k-\omega$ two-equation model is used in their study (Chen et al., 2017). In another study, A. Akgül et al. carried out a study on NASA Tandem Control Missile (Akgül et al., 2012). They also compared solution methods which are $k-\epsilon$, SST $k-\omega$, Spallart-Allmaras. Drag coefficient, lift coefficient and pitching moment coefficient are calculated in their work. Results shows that although results are very close in each solution method, SST $k-\omega$ takes the most computing time and $k-\epsilon$ is the shortest solution method.

4.1. Geometry and Computational Domain

Dimensions of the basic finner reference projectile are shown in figure 4.2.

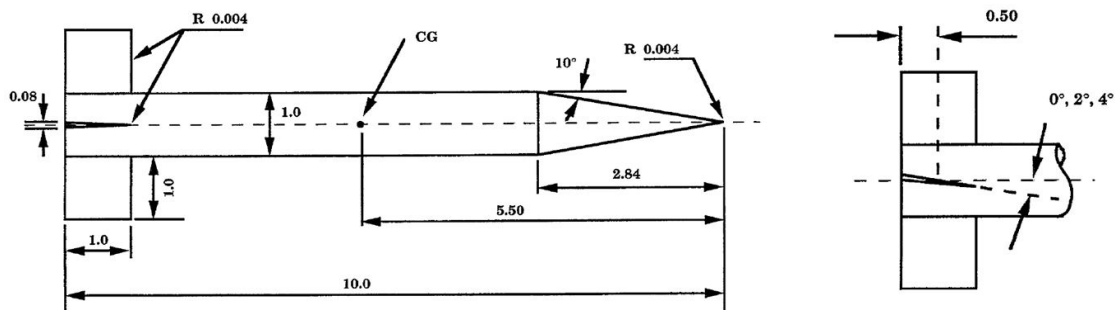


Figure 4.2. Geometry of Basic Finner Reference (Dimensions are inches)
(Source: Dupuis and Hathaway (1997)).

Although in the literature there is many various guided projectile geometry, The Basic Finner is intentionally selected as reference geometry due to simple airframe that enables possible future works on live firing tests. Properties of selected model are listed in table 4.1.

Boundary conditions and mesh domain are shown in figure 4.3.

Boundary conditions which are illustrated in figure 4.3, determined as follows.

Table 4.1. Properties of Basic Finner (Source: (Dupuis and Hathaway, 1997)).

| Property | Unit |
|----------------------|-----------------------|
| Length | 25.40 cm |
| Diameter | 2.54 cm |
| Cross Sectional Area | 22.33 cm ² |

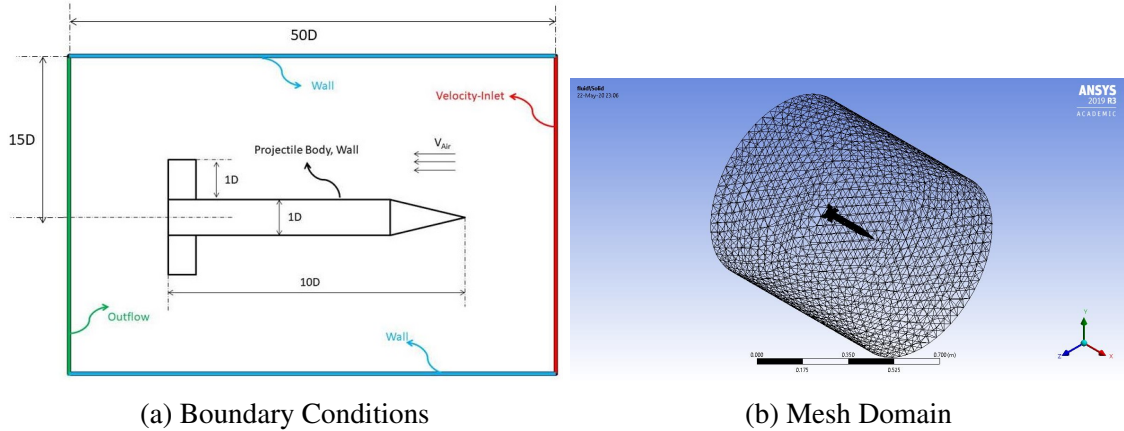


Figure 4.3. Boundary Conditions and Mesh Domain

Velocity inlet is fixed 40m/s, outflow is zero pressure outlet, projectile body and far-field are stationary wall and no-slip.

4.2. Theory

Reynolds number based on projectile length calculated as $6,91 \times 10^5$ at 40 m/s air flow, according to reynolds number formula in equation 4.1 as follows.

$$R_e = \frac{VL}{v} \quad (4.1)$$

$$R_e = \frac{40.0, 254}{1.470 \times 10^{-5}} = 6,91 \times 10^5 \quad (4.2)$$

For external flow, reynolds number bigger than can be classified as turbulent flow (Yunus

and John, 2010). Therefore Reynolds Averaged Navier-Stokes (RANS) based k- ϵ turbulence model is selected as solution method. Governing equations for fluid flow can be written as in equations 4.3 - 4.6 (Yunus and John, 2010).

$$\frac{\partial u}{\partial x} + \frac{\partial v}{\partial y} + \frac{\partial w}{\partial z} = 0 \quad (4.3)$$

$$u \frac{\partial u}{\partial x} + v \frac{\partial u}{\partial y} + w \frac{\partial u}{\partial z} = -\frac{1}{\rho} \frac{\partial P}{\partial x} + v \left(\frac{\partial^2 u}{\partial x^2} + \frac{\partial^2 u}{\partial y^2} + \frac{\partial^2 u}{\partial z^2} \right) \quad (4.4)$$

$$u \frac{\partial v}{\partial x} + v \frac{\partial v}{\partial y} + w \frac{\partial v}{\partial z} = -\frac{1}{\rho} \frac{\partial P}{\partial y} + v \left(\frac{\partial^2 v}{\partial x^2} + \frac{\partial^2 v}{\partial y^2} + \frac{\partial^2 v}{\partial z^2} \right) \quad (4.5)$$

$$u \frac{\partial w}{\partial x} + v \frac{\partial w}{\partial y} + w \frac{\partial w}{\partial z} = -\frac{1}{\rho} \frac{\partial P}{\partial z} + v \left(\frac{\partial^2 w}{\partial x^2} + \frac{\partial^2 w}{\partial y^2} + \frac{\partial^2 w}{\partial z^2} \right) \quad (4.6)$$

Transport equations for standard k- ϵ model can be also written as equation 4.7 and 4.8 (Versteege and Malalasekera, 2007).

$$\frac{\partial(pk)}{\partial t} + \operatorname{div}(p k \mathbf{U}) = \operatorname{div} \left[\left(\frac{\mu_t}{\sigma_k} \operatorname{grad} k \right) \right] + 2\mu_t S_{ij} S_{ij} - \rho\epsilon \quad (4.7)$$

$$\frac{\partial(\rho\epsilon)}{\partial t} + \operatorname{div}(p \epsilon \mathbf{U}) = \operatorname{div} \left[\left(\frac{\mu_t}{\sigma_\epsilon} \operatorname{grad} \epsilon \right) \right] + C_{1\epsilon} \frac{\epsilon}{k} 2\mu_t S_{ij} S_{ij} - C_{2\epsilon} \rho \frac{\epsilon^2}{k} \quad (4.8)$$

The constants C_μ , σ_k , σ_ϵ , $C_{1\epsilon}$ and $C_{2\epsilon}$ are determined as 0.09, 1.00, 1.30, 1.44 and 1.92 respectively for many cases of turbulent flows.

4.3. Meshing

ANSYS Fluent 2019R3 academic license allows maximum 512,000 elements. Hence, created maximum mesh element number in this simulation obtained as 511,139.

To obtain more accurate result, mesh density is increased around projectile body surfaces by using sizing and refinement methods.

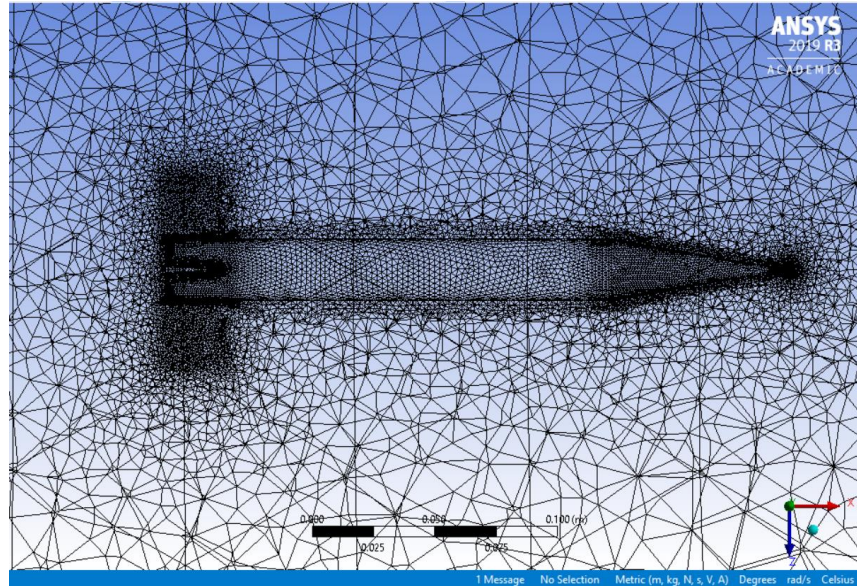


Figure 4.4. Meshing Around The Basic Finner (511,139 mesh element).

Table 4.2 shows mesh independency test for drag coefficient. As seen in the table 4.2 relative error is about 1% maximum. It can be inferred from table 4.2 that mesh number does not affect the solution seriously so it can be said that this is a mesh independent simulation.

Table 4.2. Mesh Independency Test

| | Mesh Element Number | Calculated C_D | Relative Error $ C_D^n - C_D^{n+1} /C_D^{n+1}$ |
|----|---------------------|------------------|--|
| 1. | 511,139 | 0.1444 | |
| 2. | 429,013 | 0.1449 | 0.00345 |
| 3. | 371,724 | 0.1458 | 0.00617 |
| 4. | 241,758 | 0.1477 | 0.01286 |

4.4. Solutions and Results

The main idea of the simulation is to obtain aerodynamic coefficients (C_D , C_L and C_M) of the basic finner reference model projectile at subsonic speed. Many aerodynamic parameters of the basic finner are already given in (Dupuis & Hathaway, 1997) for only supersonic speeds. Therefore, six different simulations are carried out to obtain these coefficients at low subsonic speed. Aerodynamic coefficients of the basic finner are calculated for zero-degree, 2-degree and 4-degree fin angles. Three more simulations are also carried out for mesh independency test.

Velocity contours and vectors of the basic finner for 0° , 2° and 4° fin angles at 40m/s air speed are shown in figure 4.5, 4.6 and 4.7.

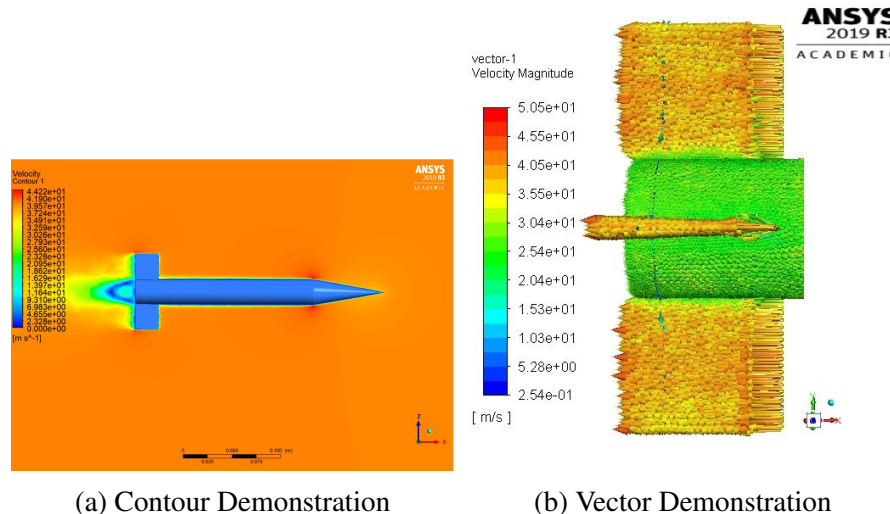
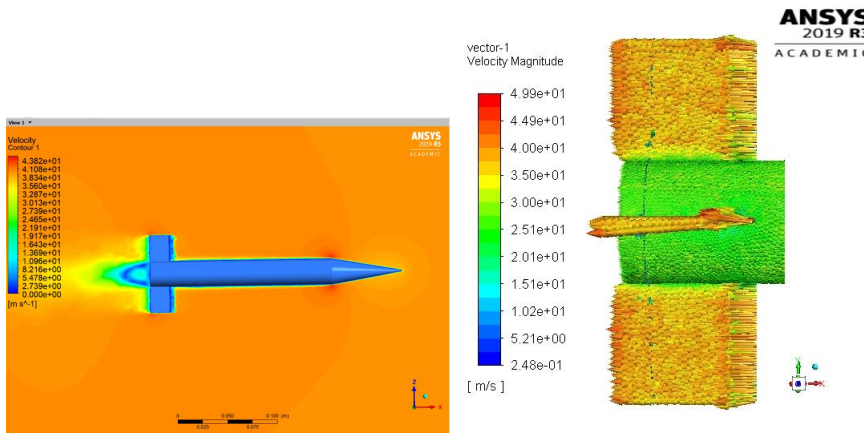


Figure 4.5. Velocity Contours and Vectors at 0° Fin Angle

Calculated aerodynamic coefficients of the basic finner (C_D , C_L and C_M) at 40m/s air speed are shown in table 4.3.

Table 4.3. Calculated Aerodynamic Coefficients.

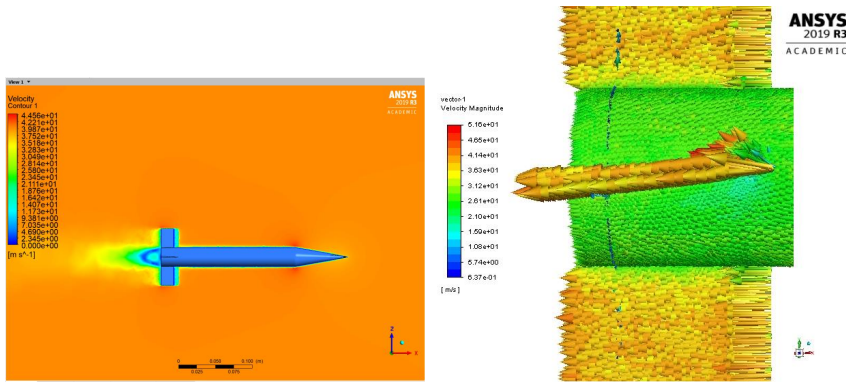
| Coefficient | Zero Degree Tail Angle | 2 Degree Tail Angle | 4 Degree Tail Angle |
|-------------|------------------------|---------------------|---------------------|
| C_D | 0.14440 | 0.14561 | 0.14804 |
| C_L | -0.000487 | 0.05938 | 0.11870 |
| C_M | 0.0000533 | 0.02214 | 0.04437 |



(a) Contour Demonstration

(b) Vector Demonstration

Figure 4.6. Velocity Contours and Vectors at 2° Fin Angle



(a) Contour Demonstration

(b) Vector Demonstration

Figure 4.7. Velocity Contours and Vectors at 4° Fin Angle

As seen in the table 4.3 drag coefficient, lift coefficient and pitching moment coefficient are increased by the tail fin deflection. When tail deflection angle increases, the cross-section area of the projectile, exposed area to the air flow, also increases. As a result of increased cross-section area, drag coefficient of projectile is also increases inherently. On the other hand, deflected tails creates lift force normal to air flow and generated lift force is also increases with respect to tail deflection angle. In addition to that, generated lift force produces moment which is named as pitching moment. Pitching moment also increases with increasing tail deflection angle inherently.

CHAPTER 5

SHOCK SURVIVABILITY CAPABILITY OF ELECTRONIC CIRCUITS

5.1. High-g Environment and Ruggedization

Extreme conditions of artillery firing is one of the main challenges for guided munition developer engineers. Firing environment of a projectile is presented in the aforementioned table 1.2. It can be inferred that under 10,000g acceleration, standard 1/4W THT resistor is exposed about 73N force. When a solder pad area about 0.8mm² is considered, stress applied to one solder pad is about 45MPa. Tensile strength of standard solder alloy (63Sn-37Pb) is given 30.6MPa in (Thomas et al., 2002). It is clear that, stress caused by acceleration is far beyond the breakaway point of solder. Consequently, high-g ruggedization methods have to be applied to gun-launched munitions. One of the major study in this field is (Burd, 1999). Burd explains methods and test procedures of high-g ruggedization.

Table 5.1. 1/4W THT Resistor Dimensions (Source:(Vishay, 2019)).

| Resistor Type | Dimensions (mm) | | | | Mass (g) |
|---------------|-----------------|-------------|-------------------|------|----------|
| | L | D | L _{1max} | d | |
| 1/4W (PTF65) | 9.53 ± 1.57 | 3.68 ± 0.41 | 12.07 | 0.64 | 0.75 |

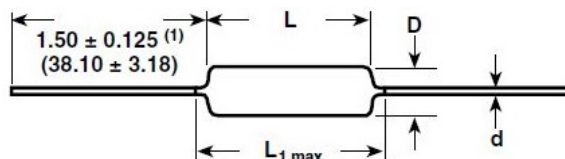


Figure 5.1. 1/4W THT Resistor Dimensions (Source:(Vishay, 2019)).

When a projectile is fired, four different acceleration forces are applied, setback, setforward, balloting and radial accelerations (Burd, 1999). These accelerations are shown in figure 5.2.

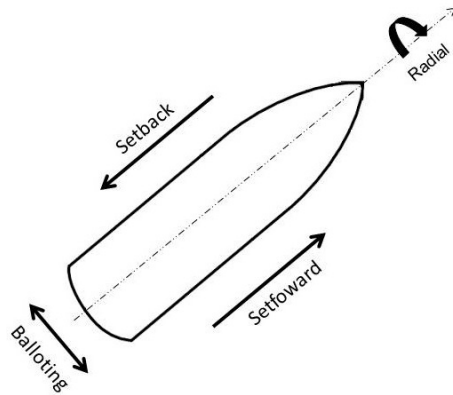
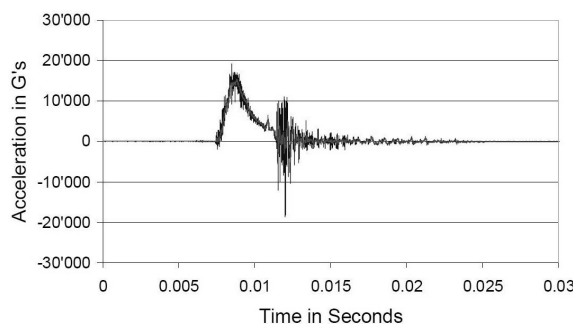


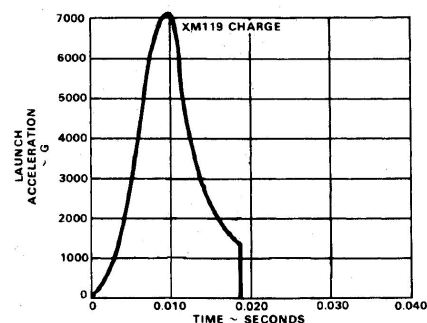
Figure 5.2. Firing Accelerations.

Setback acceleration is the compressive reaction of the projectile mass to forward acceleration and it is the highest magnitude acceleration of firing. Setforward acceleration is described as, the rapid unloading of the projectile as it leaves the muzzle. Balloting is the lateral acceleration of a projectile inside the muzzle and radial acceleration is outcome of a spinning projectile (Burd, 1999; Carlucci and Jacobson, 2018).

Example setback acceleration of projectiles are shown in figure 5.3.



(a) Typical Shock Profile of a Mortar Firing (Source:(Habibi et al., 2008)).



(b) Shock Profile of M109A1 155-mm Self-Propelled Howitzer (Source:(Morrison and Ambergton, 1977)).

Figure 5.3. Setback Acceleration of Projectiles.

Steps of high-g ruggedization can be listed as below (Burd, 1999).

- G-force requirement identification
- Component selection
- PCB design for gun hardening
- Component attachment
- Positioning the PCB
- Encapsulation and potting

First of all the g-force that projectile will be exposed must be determined. Typically, 1.25 or 1.5 times the expected acceleration is suitable for most cases (Burd, 1999).

After g-force requirements are determined, appropriate component may be selected at lowest possible cost. Air-gap capacitors, air-wound inductors, gull-wing lead ICs and commercial hybrid components are not suitable for firing environment. SMD resistors, capacitors and inductors at lowest possible size and weight, BGA package ICs and stress-compensated cut crystals must be first choice (Burd, 1999).

Stiffness of PCB is key point for ruggedization. Improper PCB may cause to lead separation and pop-off. Smaller and thicker PCBs must be preferred since they resist more deflection. Large components must be placed close to the edge of board, hence mass in the center of the board decreases (Burd, 1999).

Components must be soldered to PCB whenever it is possible. However, heavier parts may attached by using proper automated adhesive application dispenser. Mechanical fasteners such as bolts, screw, etc. can be used to increase robustness of device (Burd, 1999).

Designed PCB must placed parallel to firing direction. Therefore, deflection of board will be minimized (Burd, 1999).

Epoxy encapsulation may be the first and satisfying solution to ruggedization problem. However, components are not accessible and total mass of the device increases after encapsulation, these are the drawbacks that designers must pay attention (Burd, 1999).

After ruggedization methods applied, successive test procedures can be followed. Static test of PCB, constant acceleration load and dynamic tests are the steps of inspection (Burd, 1999). Shearing, pulling and bending of PCB are the static test of ruggedization.

Centrifuge testers are most preferable method to achieve long period constant acceleration. Therefore, components behavior can be examined under determined constant acceleration. Shock towers, airgun testers, hopkison-bar or live firing tests are the dynamic test options (Burd, 1999).

5.2. High-g Testing Methods

Hopkinson bar test method is one of the most popular experiment setup, because of capable of generating 100,000g just in micro seconds (Agnello et al., 2014). Many researches used hopkison bar to verify and calibrate novel high-g acclerometer or to observe the survivability of accelerometer packages (Agnello et al., 2014; Shi et al., 2010; Frew and Duong, 2009; Foster et al., 2011; Forrestal et al., 2003). Drop test methods are also used to examine the high-g effects on PCBs (Lall et al., 2016, 2019, 2017, 2016; Lall et al., 2015).

Other than these studies researches are also tested the high-g ruggedized PCBs and unsecured PCBs by using hopkinson bar test equipments and filmed the behaviour of the electronic components under high shocks in (Inel and Özdemir, 2021). Two classes PCBs which have same functionality but consist of different size components are produced to examine the high-g effect. As seen in the figure 5.4, one group of PCB has THT capacitor and resistors and the other has 0603 package SMD component on the board. Pin configuration of STM32L052K6 and schematic of designed PCBs are presented in the appendix A.

In addition to reducing the components size, one of the PCB moulded in epoxy to increase robustness of components. STM32L052K6, MPU6050 and HC-06 are the main components of the designed PCBs (Inel and Özdemir, 2021). Some of the features of the STM32L052K6 which is a MCU from low power family are listed in the table 5.3. The reason of selecting this MCU is nothing more than ease of soldering and compact size. MPU6050 is a popular MEMS accelerometer for many embedded system hobbyist and beginner level electronic students. MPU6050 is used in the designed PCB not for comparing the acceleration data from video analysis, it is chosen to evaluate the durability of hybrid circuit boards under extreme loads. Before testing each PCB, on board microcontroller is programmed to carry out following processes (Inel and Özdemir, 2021).



(a) PCB with THT components.



(b) PCB with SMD Components.

Figure 5.4. Prepared Specimens for Hopkinson Bar Experiment.

Therefore, in that study the functionality of the microcontrollers after exposing high accelerations are also tested.

- Reading acceleration data from MPU6050 via I2C
- Sending one-axis acceleration data by using HC-06 via UART-DMA
- Generating 100Hz sine wave
- Generating 1Hz PWM signal
- Toggling on-board LED every 500ms

5.2.1. High-g Test of PCBs at Hopkinson Bar

Hopkinson bar test equipment in IYTE Dynamic Test and Modelling Laboratory is used in the experiments. Prepared PCBs are attached to the end of the incident bar of and polystyrene recovery wall positioned 30cm away the flyaway. Hopkinson bar pressure level was set to 3 bar at each experiment 1 to 5. In the last experiment, pressure

Table 5.2. Specifications of STML052K6T6 (Source:(STMicroelectronics, 2021)).

| | |
|----------------------|---|
| CPU max. Clock Speed | 32MHz |
| Flash Memory | 32Kbyte |
| RAM | 8Kbyte |
| Package | LQFP32 |
| Connectivity | 1 x I2C 1 x SPI 2 x USART 1 x USB |
| Analog | 1 x ADC (12-bit) 1 x DAC (12-bit) 2 x Comparator |
| Other Features | Random Number Generation (RNG) Cyclic Redundancy Check (CRC) |

level increased to 6 bar to see the maximum possible effect and specimen-5 is used again in this experiment. Specimens were not powered while conducting the experiments and functionality of them tested after shock applied. All experiments recorded with 20,000 fps capable video camera and stress data of incident bar is obtained by strain gauges which are placed on (Inel and Özdemir, 2021) . Test apparatuses are shown in the figure 5.6. Acceleration of specimens are calculated by using an open source video analysis and modelling tool Tracker v.5.1.5.

5.2.1.1. Results of Hopkinson Bar Test and Discussion

In the result of experiments, a projectile firing environment is created and maximum acceleration is achieved close to 20,000g in experiment-6. It is seen in figure 5.8 that in the experiments 1 to 5, generated stress is identical and acceleration of each specimen is very close to each other. The last experiment distinguishes from the preceding experiments because of increased air gun pressure level. Frames of each specimen under thousands of g-force are shown in the appendix B.

After all experiments are carried out, specimens are tested for their functionality. It is known that MEMS based accelerometers and most of the other sensors have a

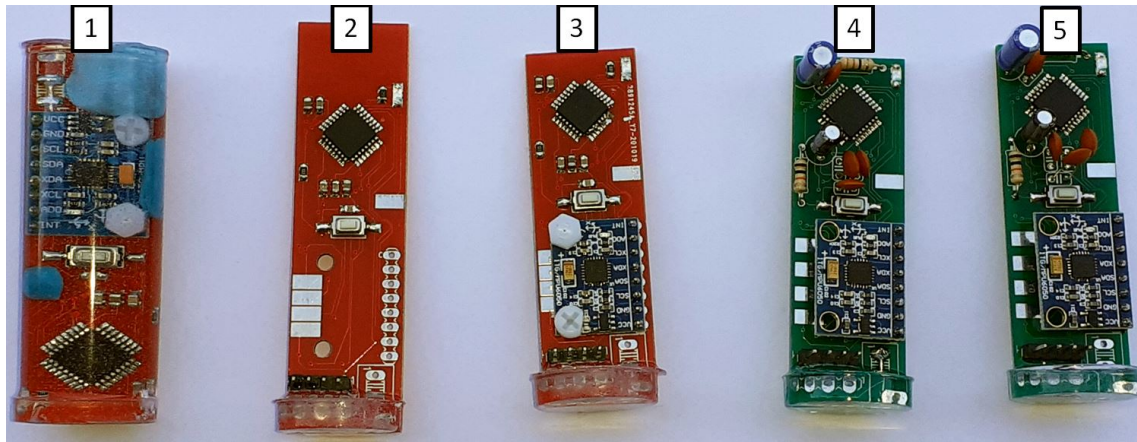


Figure 5.5. Prepared Specimens (Source: (Inel and Özdemir, 2021)).

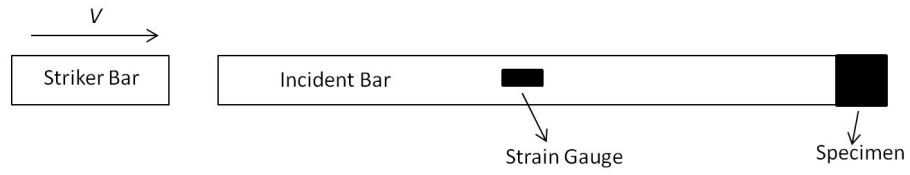
limit of maximum acceleration due to their comb-like MEMS structure. Manufacturer of MPU6050 is described the maximum unpowered acceleration to be exposed as 10,000g for 200 μ s (Ivensee, 2013). On the other hand, there is not any source for the durability of the microcontrollers and the other electronic components under high shocks. Therefore, these experiments are exclusively important to understand the endurance of electronic components under extreme conditions.

Functionality of specimens after shock applied are shown in the table 5.3. According the functionality results of the PCBs, except the last specimen, the rest passed all tests. Sine wave, PWM generation, LED toggling, data reading and sending are the same as pre-experiment results. Interestingly, although the manufacturer limits maximum acceleration limit for MPU6050 as 10,000g, it is seen that MPU6050s of specimen-1 to 4 are completely functional. However it must be considered that, the functionality results of this experiments are carried out after only one shock applied, except specimen-5. MPU6050 may be broken after multiple shock exposure.

Test results of specimen-5 are completely different from the others. Distorted output signals for sine wave and PWM are shown in the figure 5.8. Unexpectedly, despite the nonfunctionality after the experiment, specimen-5 still can be programmed.

Consequently, in the high-g durability experiments following issues are successfully tested.

- The effect of component size and weight
- Functionality of MCUs after shock exposure



(a) Hopkinson Bar Schematic.

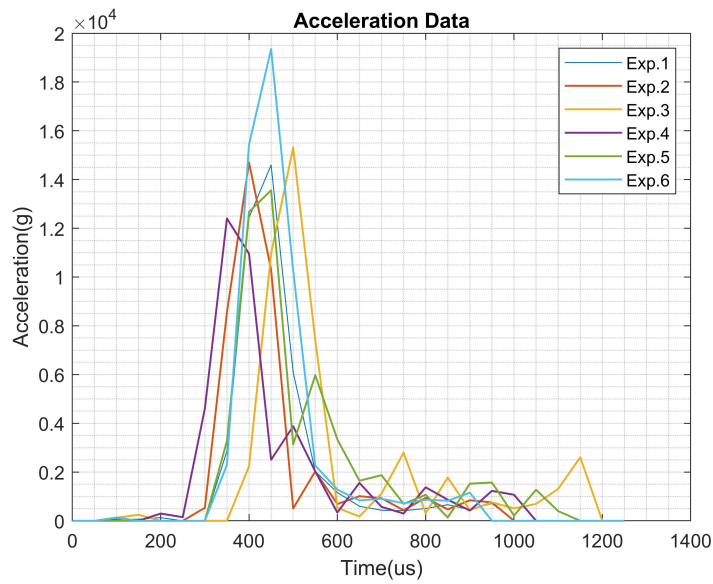


(b) Hopkinson Bar Experiment Setup.

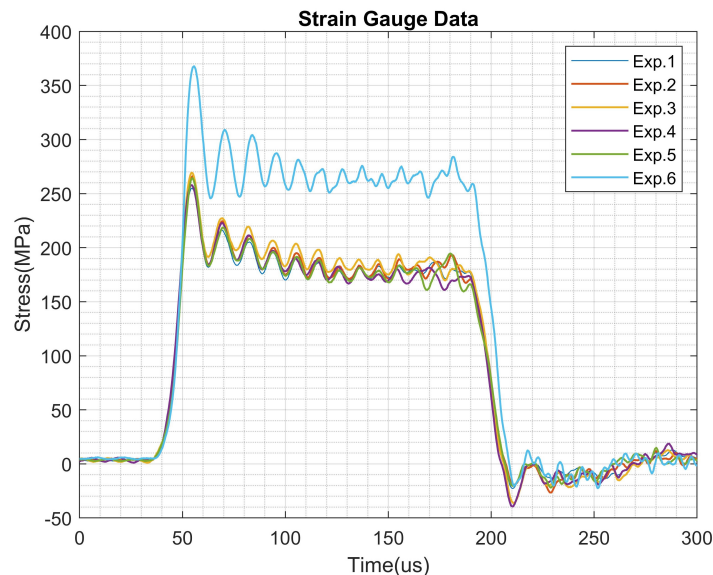
Figure 5.6. Experiment Setup (Source:(Inel and Özdemir, 2021)).

- Durability of epoxy molded and unsecured PCBs
- Behaviors of electronic components under high acceleration loads

As a result, it is seen that most of the regular off the shelf SMD components are suitable for high-g environment, while considering increased total weight, epoxy molding may be a good solution. Even though THT components did not break away during the experiment, due to large amount of swinging, it is not appropriate to use them because their characteristic features may change.



(a) Acceleration Data.



(b) Stress Data.

Figure 5.7. Acceleration and Stress Data (Source:(Inel and Özdemir, 2021)).

Table 5.3. Functionality of PCBs After Experiments.

| | Tested Feature | | | | | |
|------------|---|--|----------------------------|-------------------------------|------------|---------------------|
| | Reading Acceleration from MPU6050 (I2C) | Sending Acceleration Data via HC-06 (UART-DMA) | Generating Sine Wave (DAC) | Generating PWM signal (Timer) | Comparator | LED Toggling (GPIO) |
| Specimen-1 | ✓ | ✓ | ✓ | ✓ | ✓ | ✓ |
| Specimen-2 | - | - | ✓ | ✓ | ✓ | ✓ |
| Specimen-3 | - | - | - | - | - | - |
| Specimen-4 | ✓ | ✓ | ✓ | ✓ | ✓ | ✓ |
| Specimen-5 | FAILED | FAILED | FAILED | FAILED | FAILED | FAILED |

“✓”: Test Passed, “-”: Untested Feature, “FAILED”: Test Failed

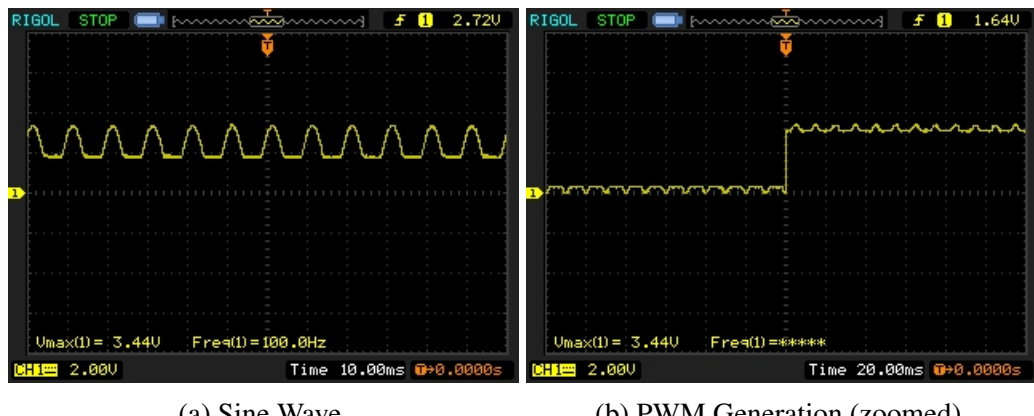


Figure 5.8. Distorted Output Signals of Specimen-5.

CHAPTER 6

CASE STUDIES, SIMULATION AND EXPERIMENTS

In this chapter supplementary studies and experiments for the thesis are presented. Inertial navigation car case study is an applied navigation design which simulates a stand-alone and GPS denied navigation example. The independent navigation systems are crucial for systems that have strategic and tactical importance such as unmanned combat aerial vehicles and guided munitions. The 6-DoF aircraft simulation case study was carried out to demonstrate the response of any aircraft. The designed simulation can be easily converted to a guidance simulation in case of, aerodynamic stability derivatives of any guided munition are obtained. In the last case study, another important issue for the guided munitions which is the analog-digital converters were studied in the aspect of conversion speed and noise vulnerability.

6.1. Inertial Navigation Car, Case Study-1

The main purpose of this case study is to demonstrate an applied GPS-denied, stand-alone navigation system performance. Therefore, only one 3-axis COTS magnetometer and a rotary encoder were used as main parts of the navigation system.

In addition to that basic inertial navigation method and microcontroller peripherals and sensors were involved. The given task in the case study is to reach a given coordinate by using inertial measurement sensors. Mainstream Performance line ARM Cortex-M3 microcontroller STM32F103C8T6, HMC5883L 3-axis magnetometer, HC-06 Bluetooth module and a rotary encoder were used as main components in the study. Image of designed vehicle is shown in the figure 6.2.

HMC5883L 3-axis magnetometer was used as main course direction finder. Therefore, magnetic flux density of the field has serious influence over the course determination. Magnetic flux density of the area was measured, using HMC5883L 3-axis magnetometer before the test runs were carried out. Measurements which were carried out at the landmark location, atrium of the İYTE Mechanical Engineering Department, on 04 November

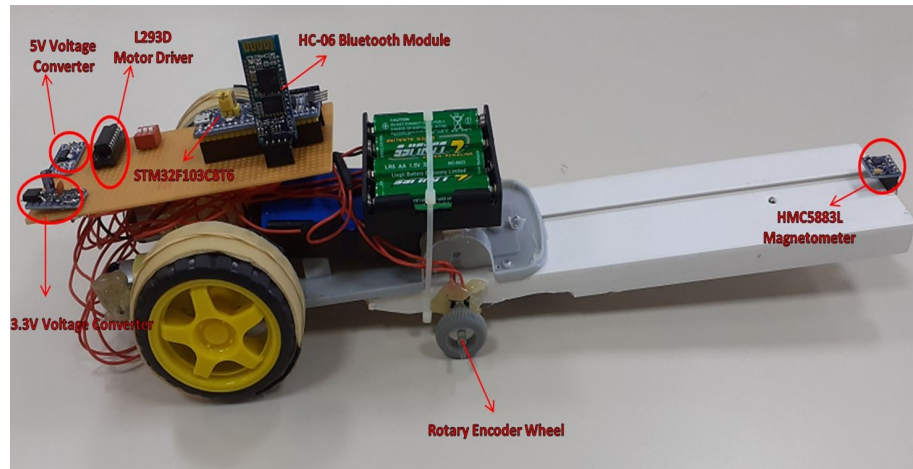


Figure 6.1. Designed Inertial Car.

2019 are shown in figure 6.3 below.



Figure 6.2. IYTE Mechanical Engineering Department Atrium (Source: Hükmü Peker A.Ş.).

As seen in the figure 6.3 magnetic flux density distribution is not equal at each measurement point. Therefore, while the vehicle travels on the test field, due to unequally dispersed magnetic flux, the vehicle veered off course.

Three navigation function “cruise”, “turnleft” and “turnright” are defined for navigation algorithm. If heading degree of vehicle is within $\pm 10^0$ of given course “cruise” function is activated. In case of the heading degree is more than 10^0 and less than 170^0 , “turnleft” function is activated. On the other hand, if heading degree is less than 10^0 and

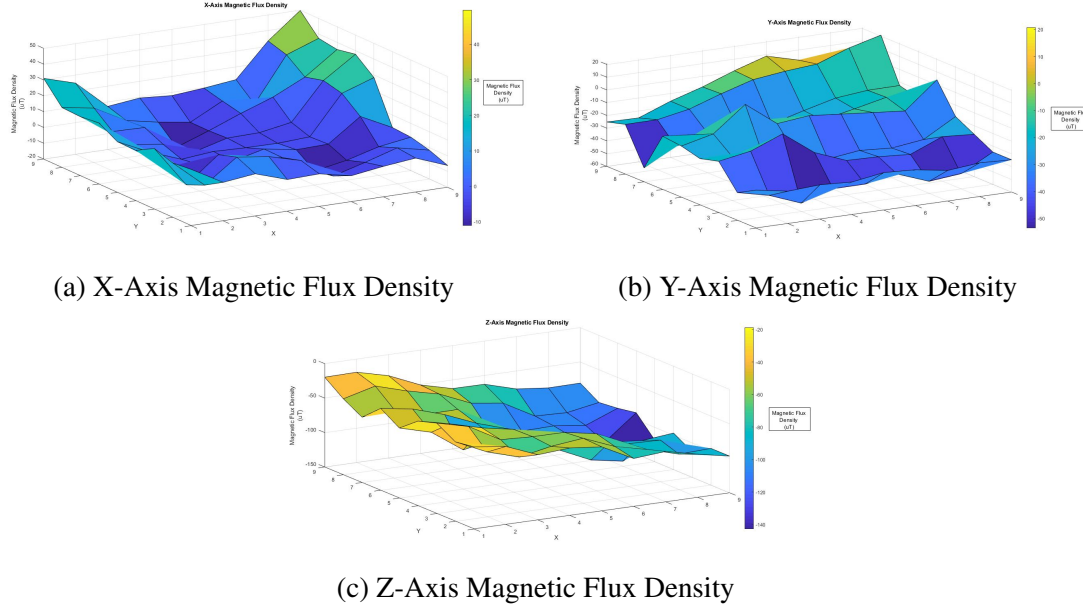


Figure 6.3. Magnetic Flux Density Measurements (Date: 04 November 2019).

more than 170^0 , “turnright” function is activated. Count of the encoder is also checked at every step. If encoder value is equal to distance, algorithm terminates the navigation. Working angles of navigation functions are shown in the figure 6.4.

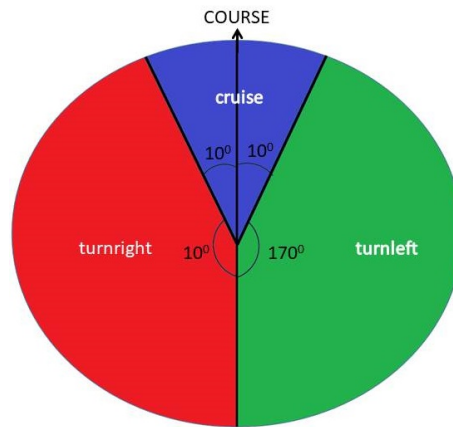


Figure 6.4. Working Angles of Navigation Functions.

At the end of this case study, designed car maintained heading $\pm 10^0$ of the given course and advanced the predetermined distance successfully.

6.2. Aircraft Autopilot Control System, Case Study-2

The objective of this case study is to establish a 6-DoF simulation for any aircraft. Therefore, aerodynamic coefficients and control inputs that are referenced by the literature were used in the state-space representation of the model.

Considering that any aircraft or munition aerodynamic parameters can be used, because of publicly availability aerodynamic coefficients of the decommissioned A-7A Corsair II aircraft was used in this case study.

In this case study, a LQR controller was aimed to be designed for lateral and longitudinal flight dynamics of an aircraft control system. Firstly, aerodynamic forces acting on aircrafts and aircraft dynamics such as longitudinal and lateral stability modes were studied. After that reference aircraft A7-A Corsair II was selected, since it is a decommissioned aircraft all of aerodynamic parameters are publicly available (Teper, 1969; Heffley and Jewell, 1972). Aircraft autopilot simulation was carried out by using MATLAB & Simulink and Flightgear 3D aircraft simulation software together. Besides, longitudinal stability comparison of A7-A Corsair II and CV-880M is extensively studied in (Tuna et al., 2020).

Longitudinal and lateral state equations are obtained from reference aircraft flight dynamics books (Cook, 2007; Nelson, 1998). The variables $x_u, z_u, y_v, \text{etc.}$ are defined as aerodynamic stability derivatives and a function of lift, drag, moment coefficients divided by mass and moments of inertia. These variables are determined for each aircraft specifically at different flight regimes, using CFD software, wind tunnel tests and live flight tests.

$$\begin{bmatrix} \dot{u} \\ \dot{v} \\ \dot{q} \\ \dot{\theta} \end{bmatrix} = \begin{bmatrix} x_u & x_w & x_q & x_\theta \\ z_u & z_w & z_q & z_\theta \\ m_u & m_w & m_q & m_\theta \\ 0 & 0 & 1 & 0 \end{bmatrix} \begin{bmatrix} u \\ w \\ q \\ \theta \end{bmatrix} + \begin{bmatrix} x_\eta \\ z_\eta \\ m_\eta \\ 0 \end{bmatrix}, y(t) = \begin{bmatrix} 0 & 0 & 0 & 1 \end{bmatrix} \begin{bmatrix} u \\ w \\ q \\ \theta \end{bmatrix} \quad (6.1)$$

$$\begin{bmatrix} \dot{v} \\ \dot{p} \\ \dot{r} \\ \dot{\phi} \\ \dot{\psi} \end{bmatrix} = \begin{bmatrix} y_v & y_p & y_r & y_\phi & y_\psi \\ l_v & l_p & l_r & l_\phi & l_\psi \\ n_v & n_p & n_r & n_\phi & n_\psi \\ 0 & 1 & 0 & 0 & 0 \\ 0 & 0 & 1 & 0 & 0 \end{bmatrix} \begin{bmatrix} v \\ p \\ r \\ \phi \\ \psi \end{bmatrix} + \begin{bmatrix} y_\xi & y_\eta \\ l_\xi & l_\eta \\ n_\xi & n_\eta \\ 0 & 0 \\ 0 & 0 \end{bmatrix} \begin{bmatrix} \xi \\ \zeta \end{bmatrix}, y(t) = \begin{bmatrix} 0 & 0 & 0 & 0 & 1 \end{bmatrix} \begin{bmatrix} v \\ p \\ r \\ \phi \\ \psi \end{bmatrix} \quad (6.2)$$

Aerodynamic parameters of A7-A Corsair II at 15,000ft altitude and 0.3 Mach velocity are obtained from (Teper, 1969) and coefficients are substituted in equations 6.1 and 6.2. Hence, complete equations of motion for A7-A Corsair II are obtained as in the equations 6.3 and 6.4.

$$\begin{bmatrix} \dot{u} \\ \dot{v} \\ \dot{q} \\ \dot{\theta} \end{bmatrix} = \begin{bmatrix} 0.00501 & 0.00464 & -72.9 & -31.34 \\ -0.0857 & -0.545 & 309 & -7.4 \\ 0.00185 & -0.00767 & -0.395 & 0.00132 \\ 0 & 0 & 1 & 0 \end{bmatrix} \begin{bmatrix} u \\ w \\ q \\ \theta \end{bmatrix} + \begin{bmatrix} 5.63 \\ -23.8 \\ -4.54576 \\ 0 \end{bmatrix} \begin{bmatrix} \eta \end{bmatrix} \quad (6.3)$$

$$\begin{bmatrix} \dot{\beta} \\ \dot{p} \\ \dot{r} \\ \dot{\phi} \\ \dot{\psi} \end{bmatrix} = \begin{bmatrix} -0.1220 & 0.2300 & -0.9748 & 0.0988 & 0.0234 \\ -8.79 & -1.38 & 0.857 & 0 & 0 \\ 0.948 & -0.0312 & -0.271 & 0 & 0 \\ 0 & 1 & 0 & 0 & 0 \\ 0 & 0 & 1 & 0 & 0 \end{bmatrix} \begin{bmatrix} \beta \\ p \\ r \\ \phi \\ \psi \end{bmatrix} + \begin{bmatrix} -0.0015 & 0.0307 \\ 3.750 & 1.820 \\ 0.280 & -1.560 \\ 0 & 0 \\ 0 & 0 \end{bmatrix} \begin{bmatrix} \xi \\ \zeta \end{bmatrix} \quad (6.4)$$

Flightgear aircraft simulation programs needs aircraft attitude angles in earth frame, and position of aircraft in geodetic position. Therefore, body frame orientations were converted to earth frame by using direct cosine matrix in the equation 6.5 and latitude, longitude and altitude of aircraft were obtained by using velocity perturbations in earth frame and the equation 6.6.

$$\begin{bmatrix} u_E \\ v_E \\ w_E \end{bmatrix} = \left(\begin{bmatrix} 1 & 0 & 0 \\ 0 & \cos\phi & \sin\phi \\ 0 & -\sin\phi & \cos\phi \end{bmatrix} \begin{bmatrix} \cos\theta & 0 & -\sin\theta \\ 0 & 1 & 0 \\ \sin\theta & 0 & \cos\theta \end{bmatrix} \begin{bmatrix} \cos\psi & \sin\psi & 0 \\ -\sin\psi & \cos\psi & 0 \\ 0 & 0 & 1 \end{bmatrix} \right)^{-1} \begin{bmatrix} u_b \\ v_b \\ w_b \end{bmatrix} \quad (6.5)$$

$$\dot{\mu} = \frac{u_E}{M + h}, \dot{\lambda} = \frac{v_E}{(N + h) \cos\mu}, \dot{h} = -w_E \quad (6.6)$$

,where M and N are the radii of the meridian and the prime vertical normal sections and defined as in equations 6.7 and 6.8 (Krakiwsky and Thomson, 1974).

$$M = \frac{a(1 - e^2)}{(1 - e^2 \sin^2 \mu)^{\frac{3}{2}}} \quad (6.7)$$

$$N = \frac{a}{(1 - e^2 \sin^2 \mu)^{\frac{3}{2}}} \quad (6.8)$$

,where “a” is the semi major axis and equals to 6,378,137m, “e” is the first eccentricity and equals to 0.081819190842622 (Krakiwsky and Thomson, 1974).

Designed full state feedback controller block diagram for A-7A aircraft is shown in the figure 6.5 and complete Simulink model and the code for LQR gain calculation are presented in appendices C and D respectively.

At the end of this case study, 6-DoF model of an aircraft was derived for a decommissioned aircraft and body frame state variables were converted to geodetic position variables (latitude, longitude and altitude). Since the formulated 6-DoF model was build up with standard aerodynamic coefficients the model can be easily converted to any aircraft or munition simulation. It is showed that for a 3D object simulation, FlightGear and Simulink model combination is an excellent example in the aspect of visuality. Finally the system output variables such as pitch rate, roll angle, etc. were monitored during the simulation successfully.

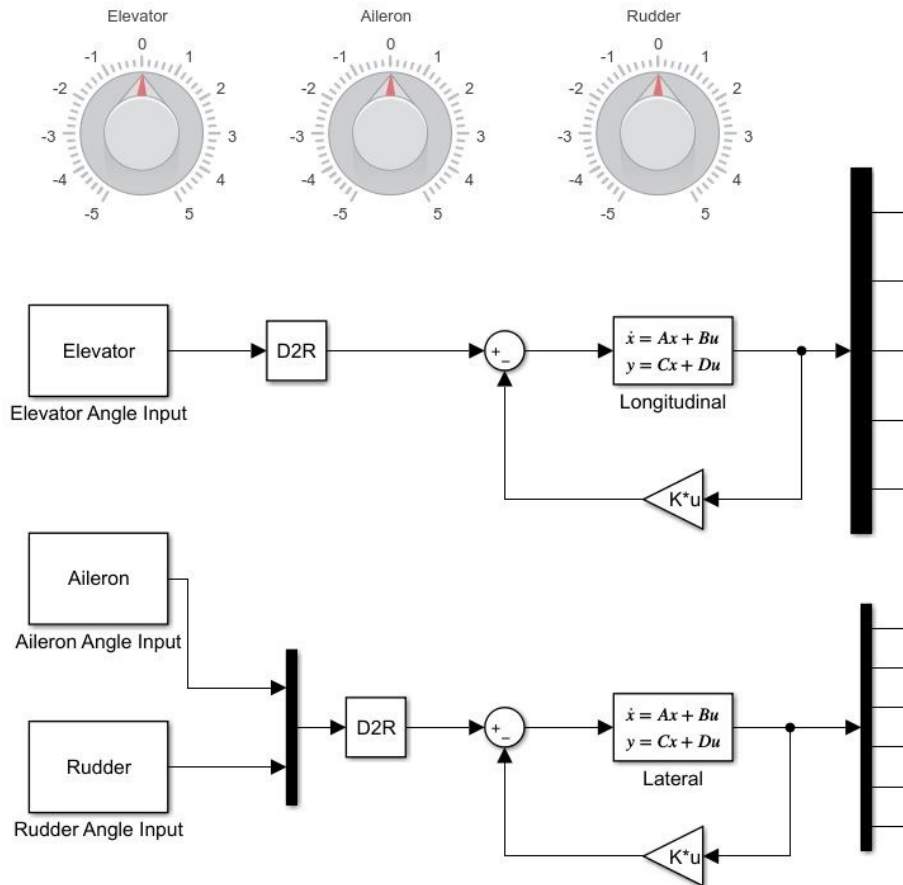


Figure 6.5. Full State Feedback Controller Block Diagram for A-7A Aircraft.

6.3. Analog-Digital Conversion (ADC), Case Study-3

In this case study another important subject of guided projectiles, the analog-digital conversion was studied in the aspects of conversion latency and noise susceptibility of internal and external ADCs. Therefore, internal ADC of the STM32F429ZIT and ADS8320, MCP3201 external ADCs were compared in this case study.

Analog to digital conversion (ADC) is the bridge between real world and computer language. Most of the sensors and actuators send out analog signal. Even if some sensors have capability of digital data output, before transmitting digital data, firstly analog signal must be converted to digital format inside the sensor, after that converted signal is sending to the processor unit.

For example, if accelerometers are considered, many types of them available for digital and analog output feature as off the shelf. MPU6050 is one of the most commonly

used sensors in the market for the reason of its price and reasonable performance for most DIY applications. MPU6050 sends out accelerometer and gyroscope data via I2C or alternatively SPI interface. However, it can be realized that the motion data is generated by comb-like MEMS structure of the sensor as analog signal and then built-in 16-bits ADC convert the signal to a digital value (Ivensee, 2013). Therefore accuracy of acceleration and gyroscope data highly depends on analog to digital conversion. MEMS structure of the sensor might measure acceleration precisely, however it may not be accurate if analog to digital conversion is not carried out properly.

ADCs can be divided into two groups, internal and external. Internal ADCs are built in features of many microcontrollers and external ADCs are stand-alone ICs that are designed just for analog digital conversion. At first glance, internal ADCs of many microcontrollers may seem advantageous, because they offer huge feature options such as many multiple channels, variable resolution, high sampling rate and compactness. However, when it comes to design high performance systems, engineers encounter many problems such as coupling between ADC channels and other peripherals. Some of the ADC errors can be listed as below (STMicroelectronics, 2020, 2003).

- Errors due to the ADC itself
 - Offset error
 - Gain error
 - Differential linearity error
 - Integral linearity error
 - Total unadjusted error
- Errors due to the ADC environment
 - Reference voltage noise
 - Reference voltage / power supply regulation
 - External reference voltage parameters
 - Analog input signal noise
 - ADC dynamic range bad match for maximum input signal amplitude
 - Effect of the analog signal source resistance

- Effect of source capacitance and parasitic capacitance of the PCB
- Injection current effect
- Temperature influence
- I/O pin crosstalk
- EMI-induced noise

Methods to improve accuracy are explained comprehensively in (STMicroelectronics, 2020, 2003). In this section, cross-talk among peripherals and ADC channels and comparison of internal and external ADCs will be presented and comparison of internal and external ADCs was carried out. STM32F429 Discovery board, ADS8320 and MCP3201 were used during the experiments.

6.3.1. Cross-talk Between SDIO and ADC Channels

Secure digital input/output interface (SDIO) feature enables to read and write data onto SD memory cards, multimedia cards and CE-ATA devices (STMicroelectronics, 2017, 2016).

As mentioned before, one of the ADC error reasons is CPU noise. It is recommended by microcontroller manufacturer that to reduce ADC error, CPU activity have to be minimized and toggling the same port I/O pins must be avoided (STMicroelectronics, 2020, 2003). However minimizing the CPU activity, widely tie down engineers and it is not possible every time. Therefore, the most effective solution is to move ADC unit outside the microcontroller. External ADCs are the best solution mostly.

CPU noise effect during the analog digital conversion is observed while recording ADC values to SD card. The output of the MMA2204 one-axis accelerometer is measured by internal ADC of STM32F429 via DMA and ADS1115 external ADC, meanwhile ADC values are recorded to SD card simultaneously. Results are shown in figure 6.6.

Expected value of MMA2204 accelerometer while stationary is $V_{DD}/2 \approx 2048$. As it can be seen in figure 6.6 measurements by ADS1115 external ADC are very close to the expected value. On the other hand, internal ADC measurement values have great offset and scatter widely.

The reason of this error may be explained by data buses of ADC channels and SDIO peripherals. As it can be seen in figure 6.7 that SDIO peripheral and ADC channels are both using APB2 data bus.

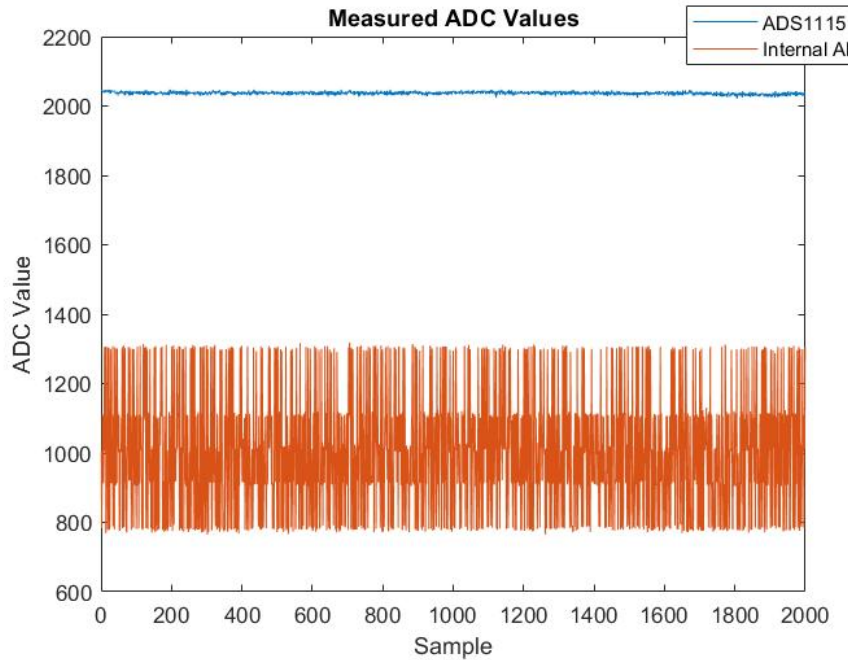


Figure 6.6. Measured ADC Values.

6.3.2. Comparison of ADCs

Analog digital converters have two main properties resolution and sampling time. Internal ADCs of microcontrollers has high sampling rate and because of embedded ADC structure additional place is not required. However, most low cost microcontroller has 10 or 12-bits ADC. In addition to that to isolate ADC channel from other microcontroller peripherals is almost impossible. On the other hand, external ADC has wide resolution range and sampling time options. Nevertheless, additional cost and extra space for IC are drawbacks of external ADCs.

Internal ADC of STM32F429, ADS8320 and MCP3201 are tested with reference sine and square signals. Main properties of tested ADCs are listed in the table 6.1.

Maximum ADC clock cycle for STM32F429 is defined as 45 MHz in (STMicroelectronics, 2016). Therefore, maximum sampling rate of STM32F429 at 12-bit resolu-

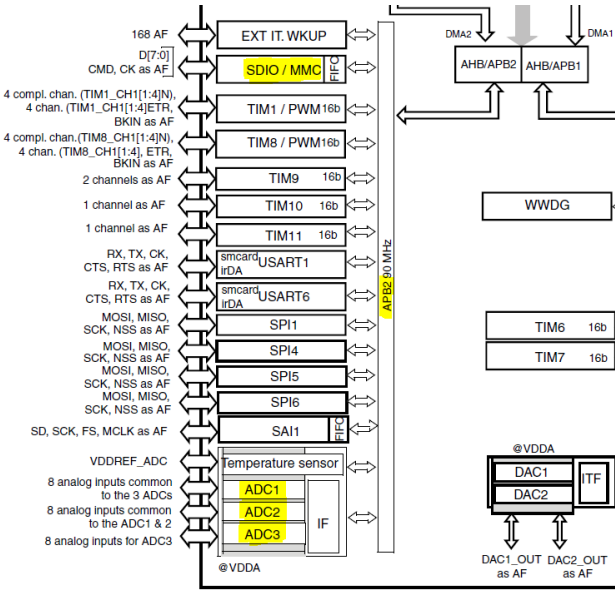


Figure 6.7. APB2 Data Bus of STM32F429 (Source:STMicroelectronics (2016))

tion can be calculated as 3 MSPS. Sampling rate of STM32F429 is far beyond its rivals. As it can be seen that ADC sampling rate of microcontroller can be increased more by boosting the CPU clock frequency. High sampling rate capable ADC and many other feature is wonderful for a low cost microcontroller. However as it is explained in section 6.3.1, interference between ADC channels and other MCU peripheral is inevitable. Therefore, it involves additional cost space, having an external ADC is the best choice.

Responses of ADCs which are listed in table 6.1 tested for high frequency and different waveform. All ADCs are tested in the same test condition. The test mission is defined as, first convert analog signal to digital value and then by using digital analog convertor (DAC) of STM32F429 display converted values on oscilloscope. Test mission is illustrated in figure 6.8.

In the test mission, everything except ADC was kept constant and CPU clock frequency of STM32F429 was set to 102.4 MHz to achieve best SPI bus frequency for ADS8320 and MCP3201. Therefore, DAC related and other computational latencies are minimized.

Sine wave test results are shown in following figures. Oscilloscope images of STM32F429 ADC, ADS8320 and MCP3201 for sine wave are shown in figures 6.9, 6.10, 6.11 respectively.

As expected STM32F429 ADC has the best performance at high frequencies, be-

Table 6.1. Comparison of ADCs.

| Analog Digital Convertor | Sampling Time | Resolution | Analog Voltage Input Range |
|--------------------------|---------------------------------|------------|--|
| STM32F429 | 15 ADC Clock Cycle | 12-bit | $V_{REF_-} \leq V_{in} \leq V_{REF_+}$ |
| | 13 ADC Clock Cycle | 10-bit | |
| | 11 ADC Clock Cycle | 8-bit | |
| | 9 ADC Clock Cycle | 6-bit | |
| ADS8320 | 100kSPS | 16-bit | $-0.3 < V_{in} < V_{CC} + 0.3$ |
| MCP3201 | 100kSPS at 5V 50kSPS at 2.7V | 12-bit | $IN_- < V_{in} < V_{REF} + IN_-$ |

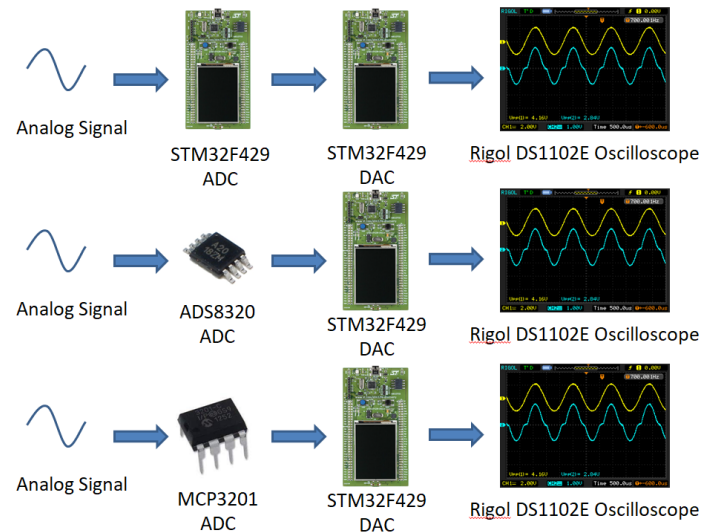
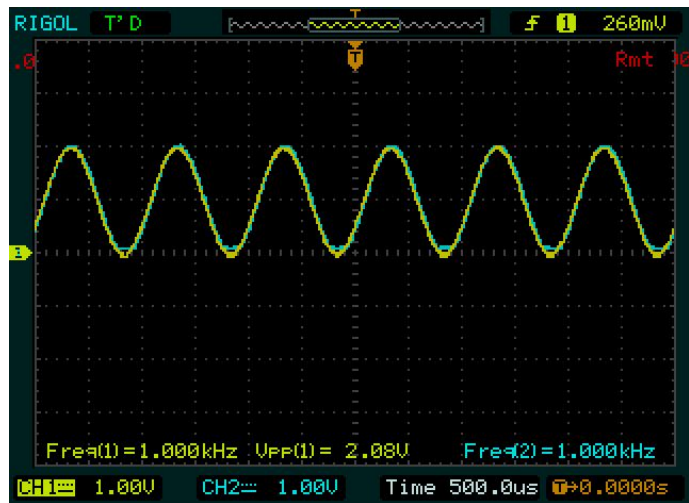


Figure 6.8. ADC Test Mission.

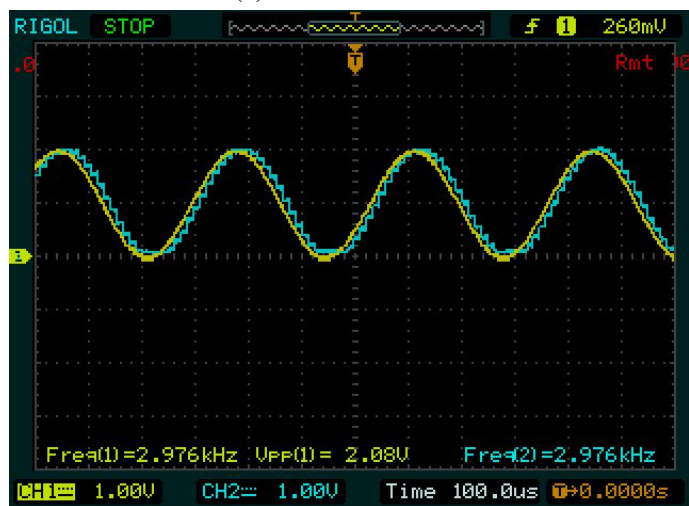
cause of high sampling rate. On the other hand, since ADS8320 and MCP3201 has same sampling rate, their results are close to each other.

Square wave test results are shown in figure 6.12. As frequency increased square waveform did not change considerably, therefore only the results of 1kHz square wave analog input are presented in the following figures. During the square wave tests for STM32F429 ADC, CPU clock frequency of microcontroller was set to 180MHz, for ADS8320 and MCP3201 to achieve maximum SPI bus speed CPU clock frequency was set to 76.8MHz and 102.4MHz respectively.

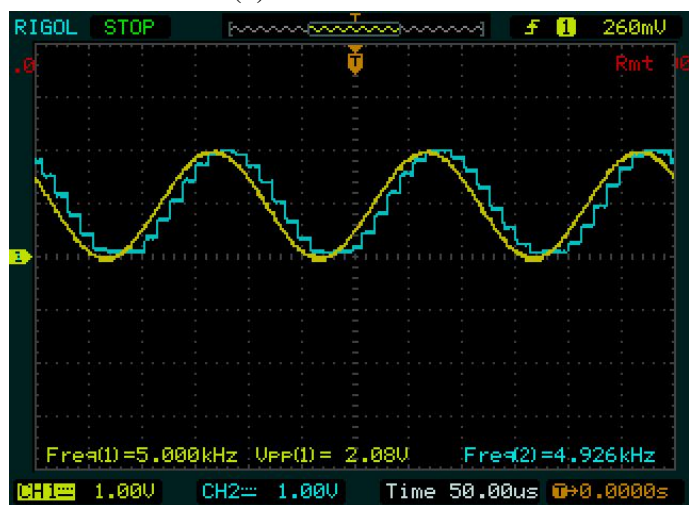
The results of square wave test in the figure 6.12 clearly explains that embedded ADC of STM32F429 is almost 10 times faster than ADS8320 and MCP3201.



(a) 1kHz Sine Wave

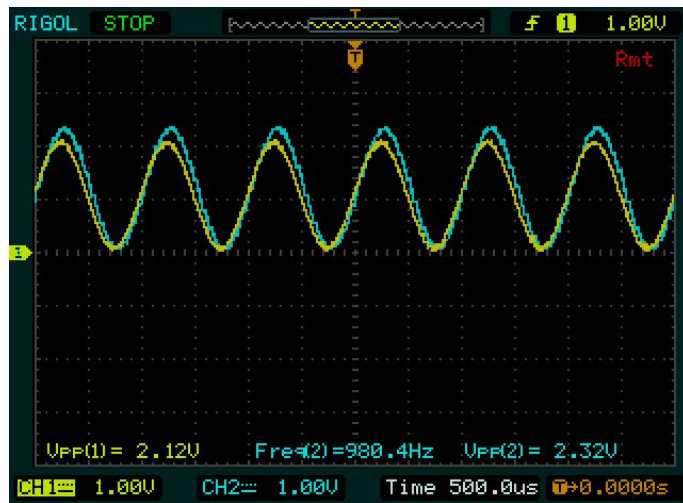


(b) 3kHz Sine Wave

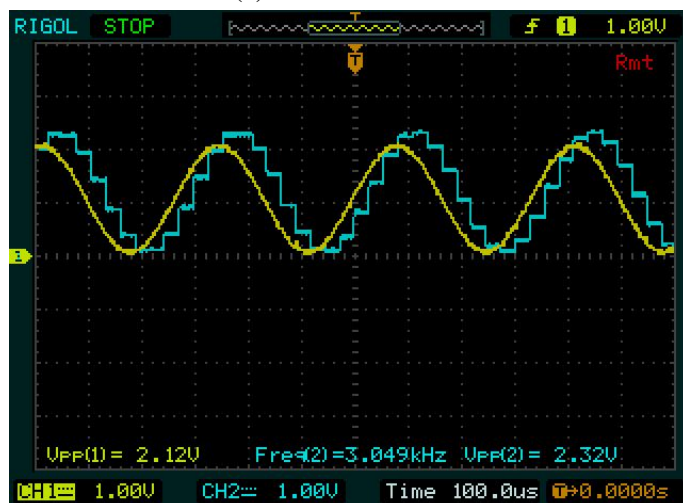


(c) 5kHz Sine Wave

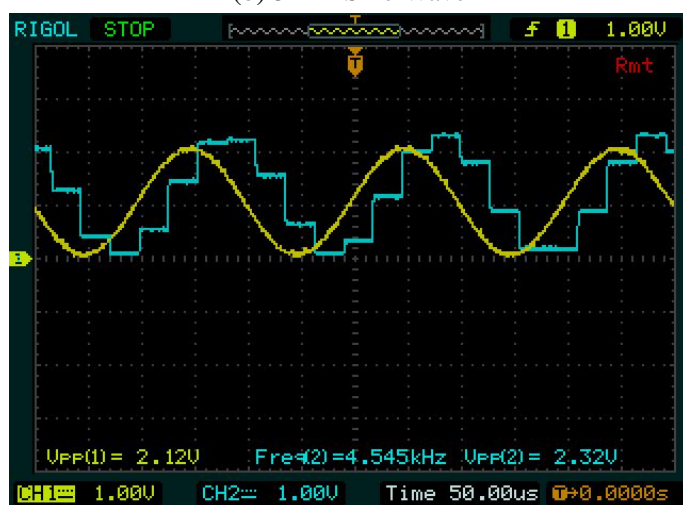
Figure 6.9. Test Results of STM32F429 ADC.



(a) 1kHz Sine Wave

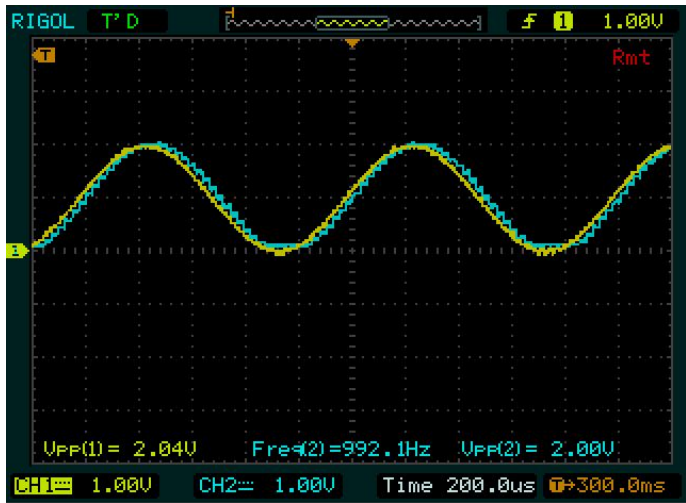


(b) 3kHz Sine Wave

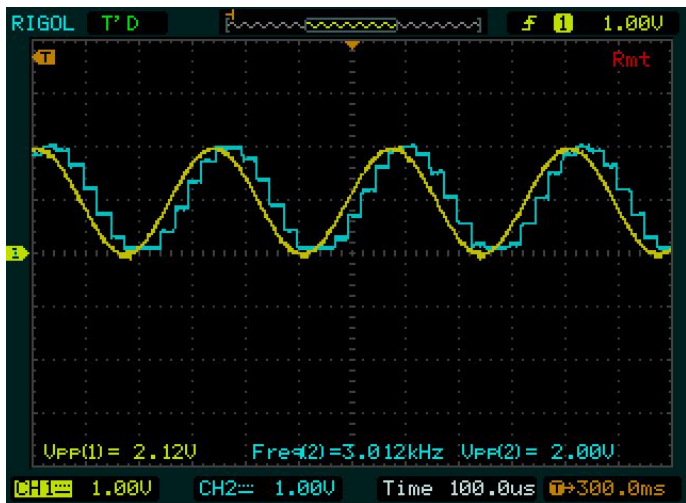


(c) 5kHz Sine Wave

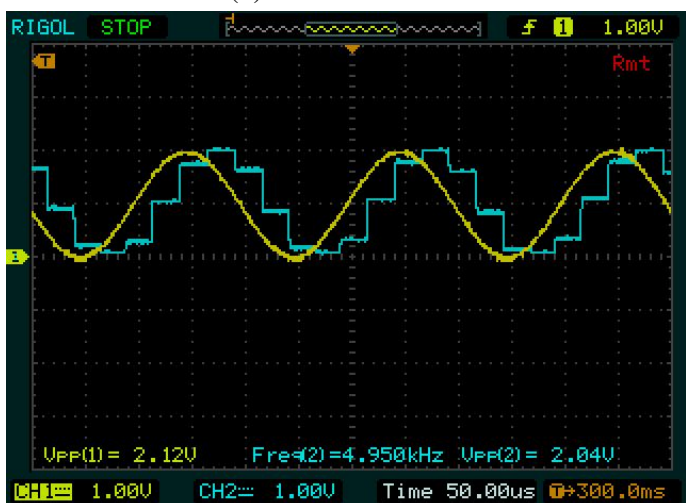
Figure 6.10. Test Results of ADS8320 ADC.



(a) 1kHz Sine Wave

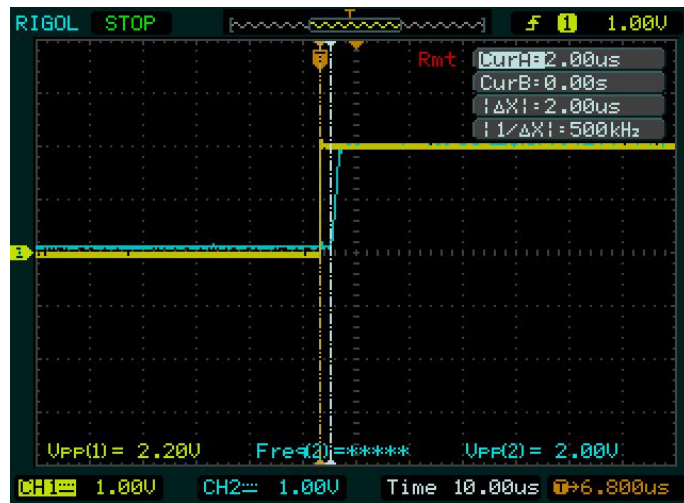


(b) 3kHz Sine Wave

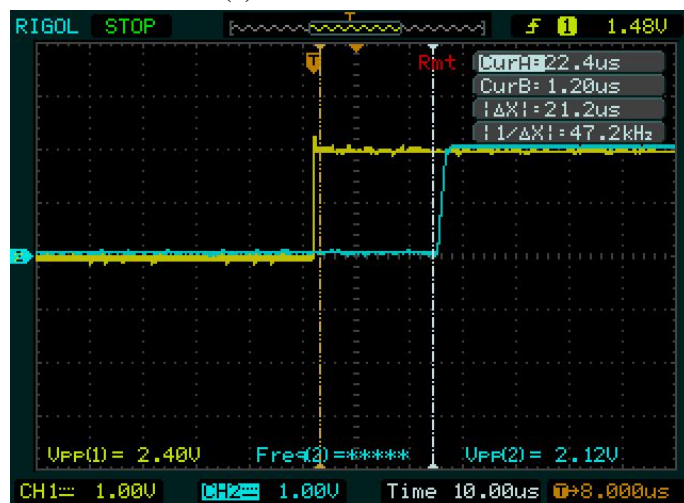


(c) 5kHz Sine Wave

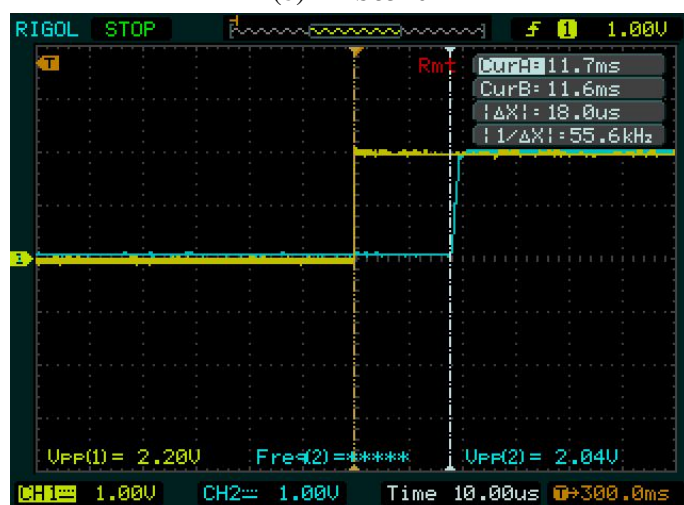
Figure 6.11. Test Results of MCP3201 ADC.



(a) STM32F429 ADC



(b) ADS8320



(c) MCP3201

Figure 6.12. Test Results of Square Wave Analog Input.

CHAPTER 7

CONCLUSIONS

In this thesis a navigation system for gun projectiles was developed with pre-set guidance principle using pole placement methodology and LQR controller. An observer for the munition state-space model was also evaluated. Design parameters for the controller and the observer, determined in reference to the foremost previous studies on guided projectile studies. A guided missile state-space model with similar flight regime was used instead of chosen Basic Finner Reference Projectile state-space model, due to inadequate open source aerodynamic parameters for 6-DoF equations of motion. An open source flight simulator FlightGear was combined with MATLAB & Simulink to visualize the navigation system.

In addition to that aerodynamic parameters of the Basic Finner Reference Projectile was also studied for subsonic launch velocities with different fin deflection angles. Considering the safety issues and experiment expenses, airgun and catapult launchers are more suitable than field live firing tests. Therefore, lift, drag and pitching moment coefficients were determined at 40m/s that simulates an airgun or catapult firing. CFD calculations were carried out using RANS based $k - \epsilon$ turbulence model with ANSYS Fluent 2019R3 (academic) software.

Another significant part of this thesis is the high-g ruggedization of PCBs and the behaviour of the common off the shelf electronic components under artillery firing environment. Hopkinson bar test equipment was used to simulate a projectile firing acceleration at maximum 20,000g. Test specimens were produced using different high-g ruggedization methods and tested under identical conditions to observe the durability of the common off the shelf electronic components with different protection levels. While secured PCBs stood robust and functional at the moment of impact, improper PCBs also remained functional at 14,000g despite violent shudder. However, due to intense vibration of unsecured electronic components, it is clear that non-ruggedized PCBs may break or change characteristics under a projectile firing environment.

Finally, several case studies were carried out to extend the knowledge in the navi-

gation and signal processing. Inertial navigation car case study is the experimental piece of research that operates a simple magnetic navigation system. Aircraft autopilot control system case study is a complete 6-DoF simulation of an decommissioned aircraft. Geodetic positioning is also included in this case study. Lastly, analog-digital conversion case study is an experimental analysis that shows the noise effects on ADCs and the performance comparison of common off the shelf external ADCs and internal ADC of STM32F4.

APPENDIX A

HIGH-G EXPERIMENT PCB PINOUTS AND SCHEMATIC

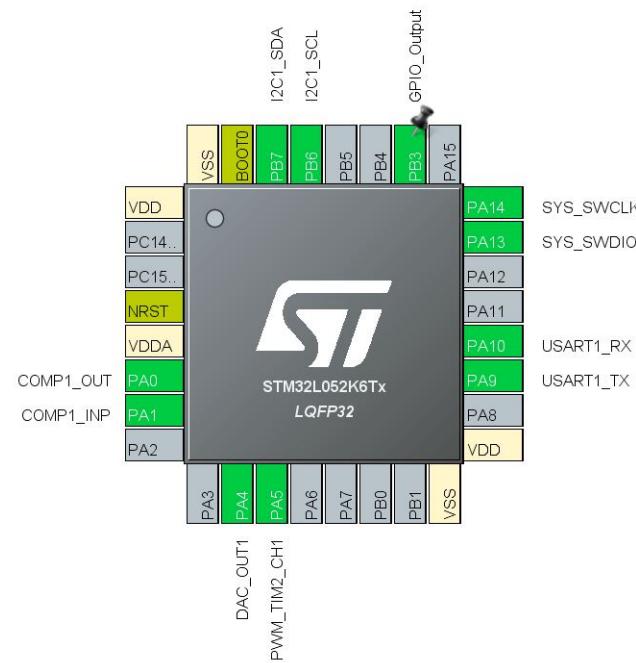


Figure A.1. Pin Configuration of STM32L052K6.

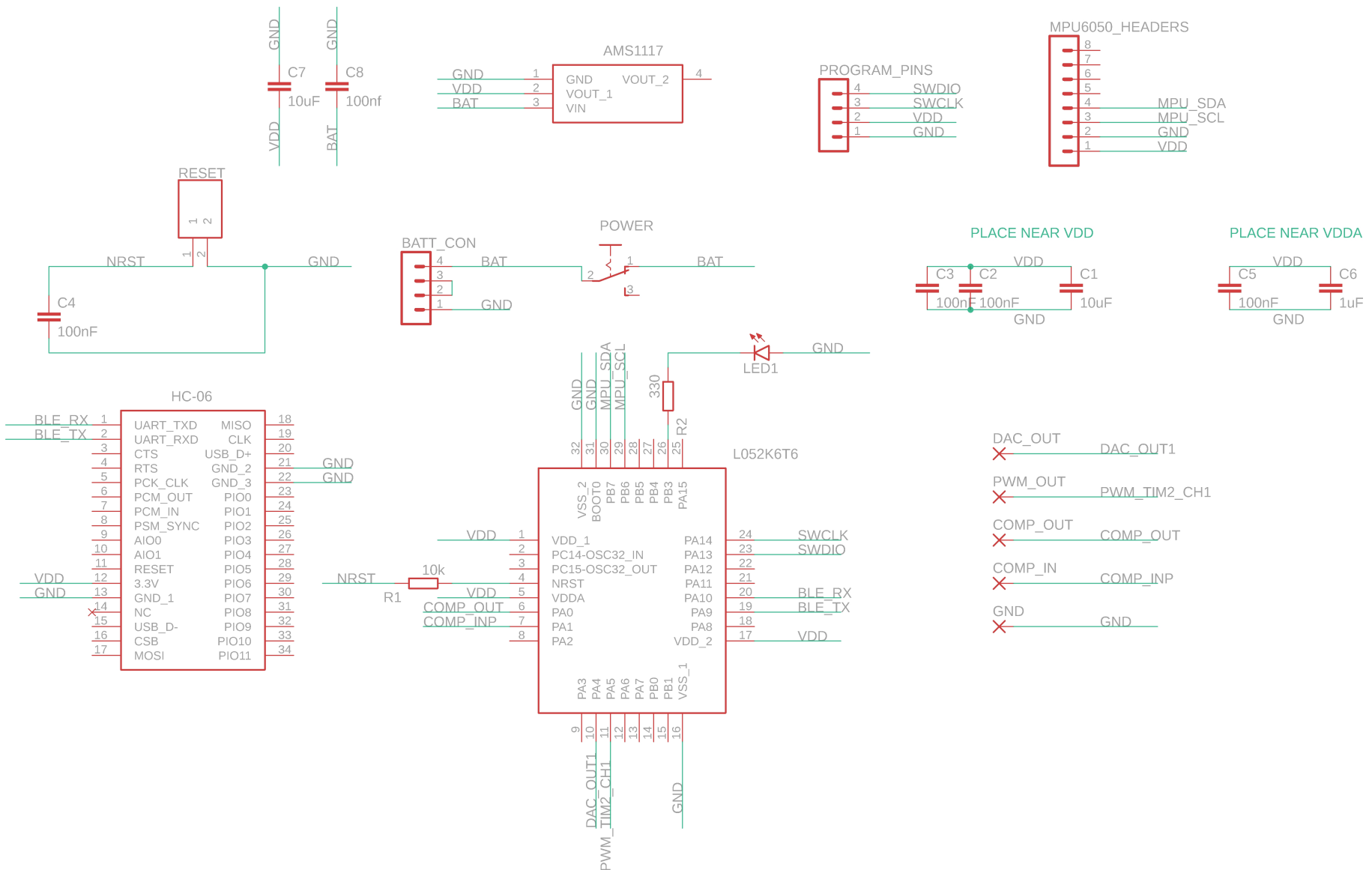


Figure A.2. Schematic of Designed PCBs for Hopkinson Bar Experiments.

APPENDIX B

HOPKINSON BAR EXPERIMENT IMAGES

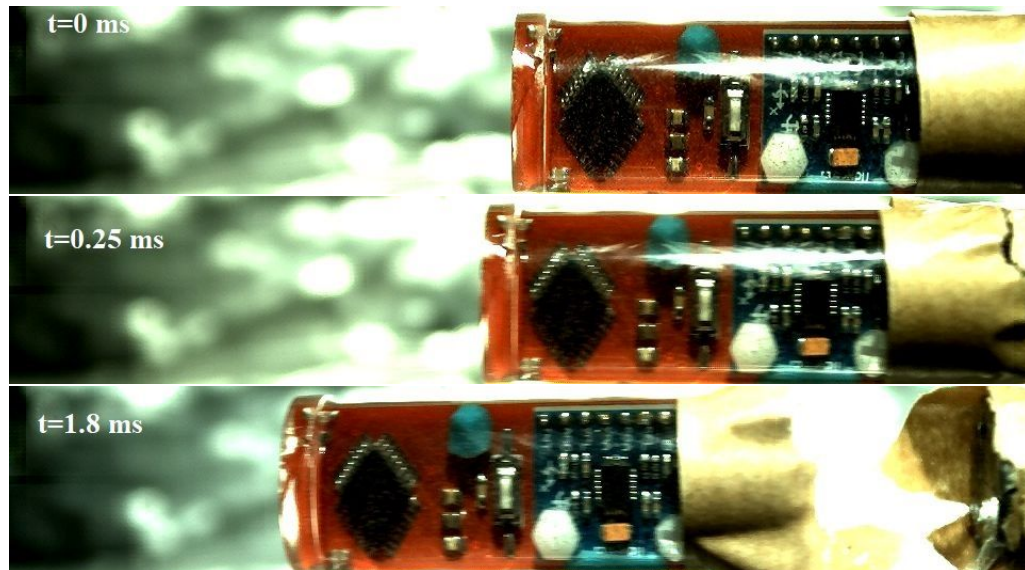


Figure B.1. Experiment Number-1 (Source:(Inel and Özdemir, 2021)).

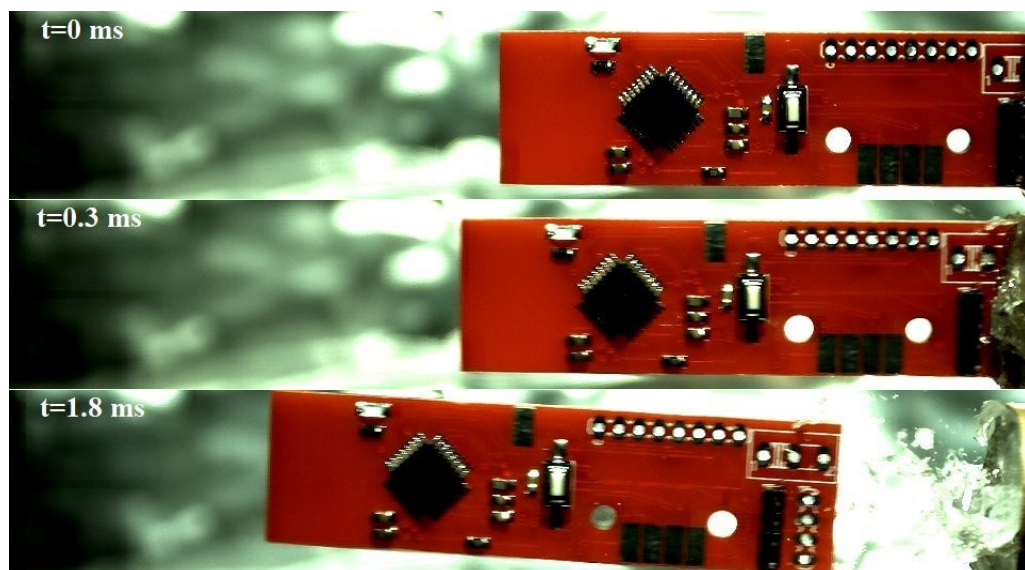


Figure B.2. Experiment Number-2 (Source:(Inel and Özdemir, 2021)).

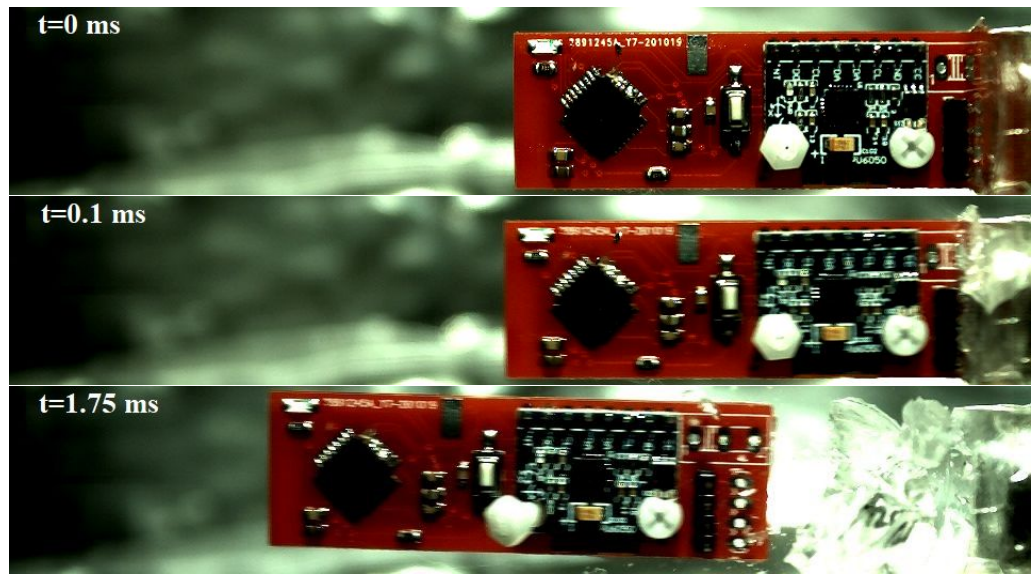


Figure B.3. Experiment Number-3 (Source:(Inel and Özdemir, 2021)).



Figure B.4. Experiment Number-4 (Source:(Inel and Özdemir, 2021)).

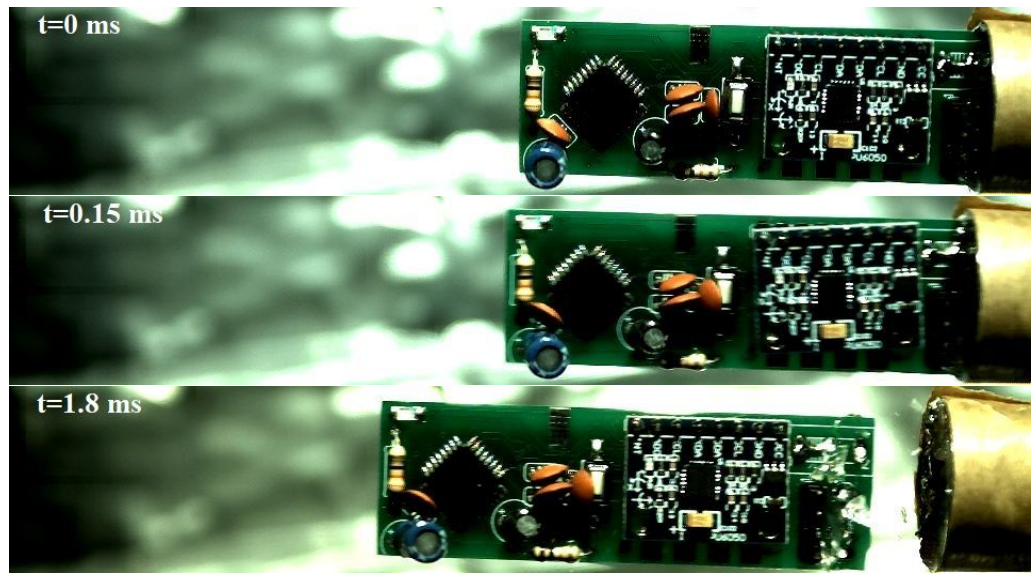


Figure B.5. Experiment Number-5 (Source:(Inel and Özdemir, 2021)).

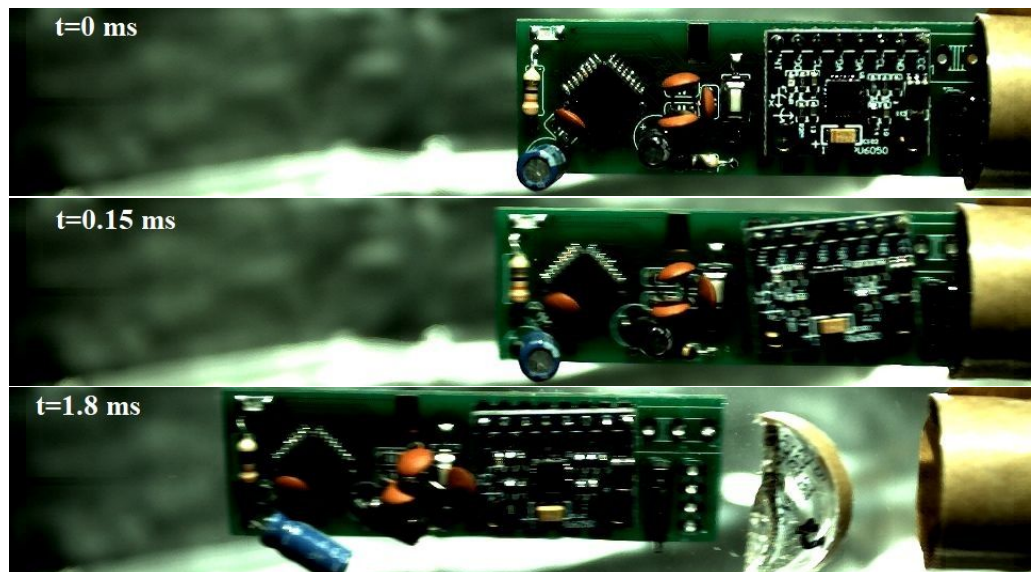


Figure B.6. Experiment Number-6 (Source:(Inel and Özdemir, 2021)).

APPENDIX C

SIMULINK BLOCK DIAGRAM FOR AIRCRAFT AUTOPILOT CONTROL SYSTEM

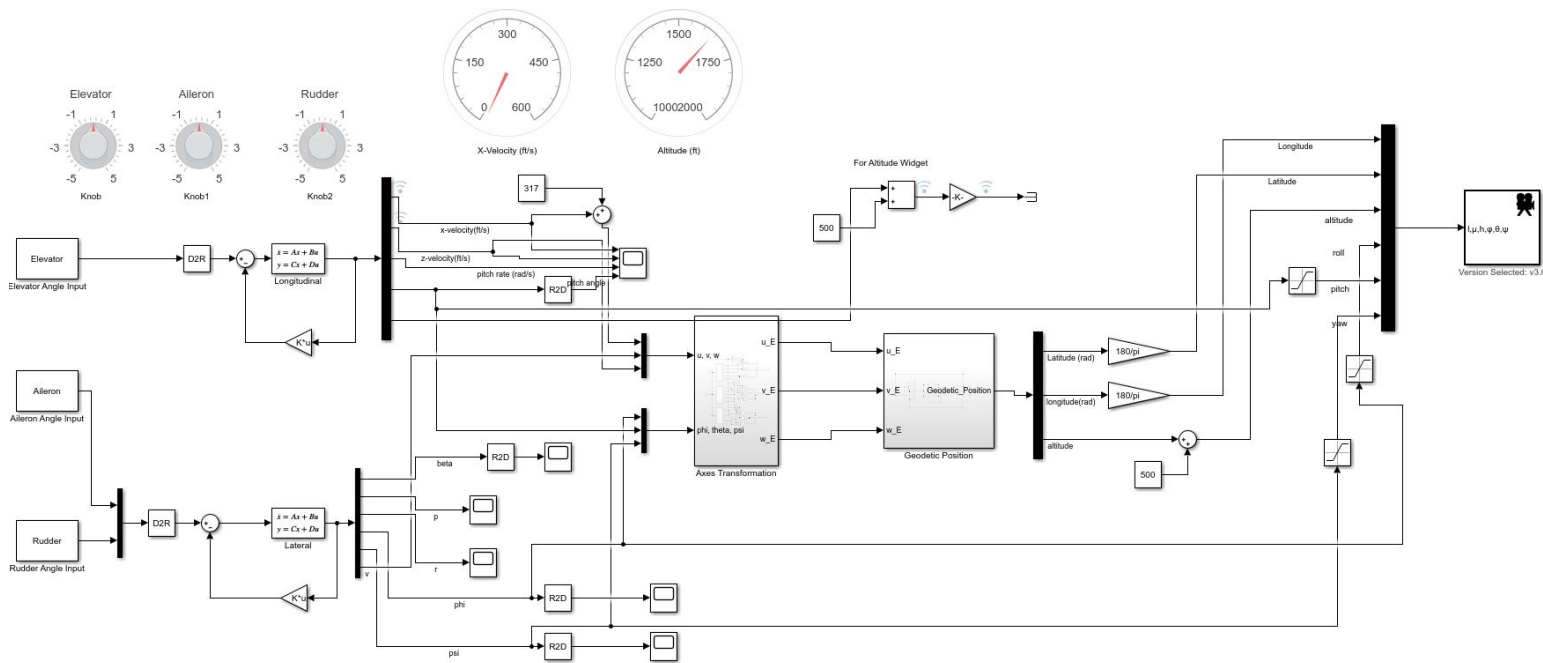


Figure C.1. Aircraft Autopilot Control System Block Diagram

APPENDIX D

CODE FOR LQR GAIN CALCULATION

Code for LQR Gain Calculation for Longitudinal Motion

```
A=[0.00501 0.00464 -72.9 -31.34 0;-0.0857 -0.545 309 -7.4 0;  
0.00185 -0.00767 -0.395 0.00132 0;0 0 1 0 0;  
0.23 -0.973179 0 314.482896 0];
```

```
B=[5.63;-23.8;-4.51576;0;0];  
C=[1 0 0 0 0;0 1 0 0 0;0 0 1 0 0;0 0 0 1 0;0 0 0 0 1];  
D=0;  
Q=[1 0 0 0 0;0 1 0 0 0;0 0 1 0 0;0 0 0 1 0;0 0 0 0 1];  
R=[1000000];
```

```
KLong=lqr(A,B,Q,R);
```

```
kL1=KLong(1);kL2=KLong(2);kL3=KLong(3);kL4=KLong(4);kL5=KLong(5);
```

Code for LQR Gain Calculation for Lateral Motion

```
A1 = [-0.122 0.23 -0.9748 0.0988 0.0234 0;-8.79 -1.38 0.857 0 0 0;  
0.948 -0.031 -0.271 0 0 0;0 1 0 0 0 0;0 0 0 1 0 0 0;  
38.647 72.9 -309 31.317 7.403 0];
```

```
B1 = [-0.0015 0.0307;3.75 1.82;0.28 -1.56;0 0;0 0;-0.476 9.732];  
C1 = [1 0 0 0 0 0;0 1 0 0 0 0;0 0 1 0 0 0;0 0 0 1 0 0;0 0 0 0 1 0;  
0 0 0 0 0 1];
```

```
D1 = 0;
```

```
Q1=[1 0 0 0 0 0;0 1 0 0 0 0;0 0 1 0 0 0;0 0 0 1 0 0;0 0 0 0 1 0;  
0 0 0 0 0 1];
```

```
R1=[100000 0;0 100000];
```

```
KLat=lqr(A1,B1,Q1,R1);  
k1=KLat(1);k2=KLat(2);k3=KLat(3);
```

APPENDIX E

COMBINED AERODYNAMIC COEFFICIENTS AND MOMENT OF INERTIA

Combined Aerodynamic Coefficients:

$$C_{p_0} = \Gamma_3 C_{l_0} + \Gamma_4 C_{n_0} \quad C_{r_0} = \Gamma_4 C_{l_0} + \Gamma_8 C_{n_0}$$

$$C_{p_\beta} = \Gamma_3 C_{l_\beta} + \Gamma_4 C_{n_\beta} \quad C_{r_\beta} = \Gamma_4 C_{l_\beta} + \Gamma_8 C_{n_\beta}$$

$$C_{p_p} = \Gamma_3 C_{l_p} + \Gamma_4 C_{n_p} \quad C_{r_p} = \Gamma_4 C_{l_p} + \Gamma_8 C_{n_p}$$

$$C_{p_r} = \Gamma_3 C_{l_r} + \Gamma_4 C_{n_r} \quad C_{r_r} = \Gamma_4 C_{l_r} + \Gamma_8 C_{n_r}$$

$$C_{p_{\delta_a}} = \Gamma_3 C_{l_{\delta_a}} + \Gamma_4 C_{n_{\delta_a}} \quad C_{r_{\delta_a}} = \Gamma_4 C_{l_{\delta_a}} + \Gamma_8 C_{n_{\delta_a}}$$

$$C_{p_{\delta_r}} = \Gamma_3 C_{l_{\delta_r}} + \Gamma_4 C_{n_{\delta_r}} \quad C_{r_{\delta_r}} = \Gamma_4 C_{l_{\delta_r}} + \Gamma_8 C_{n_{\delta_r}}$$

Combined Moment of Inertia:

$$\Gamma_1 = \frac{I_{xz}(I_x - I_y + I_z)}{I_x I_z - I_{xz}} \quad \Gamma_2 = \frac{I_z(I_z - I_y) + I^2_{xz}}{I_x I_z - I_{xz}} \quad \Gamma_3 = \frac{I_z}{I_x I_z - I_{xz}}$$

$$\Gamma_4 = \frac{I_{xz}}{I_x I_z - I_{xz}} \quad \Gamma_5 = \frac{(I_z - I_x)}{I_y} \quad \Gamma_6 = \frac{(I_{xz})}{I_y}$$

$$\Gamma_7 = \frac{I_x(I_x - I_y) + I^2_{xz}}{I_x I_z - I_{xz}} \quad \Gamma_8 = \frac{I_x}{I_x I_z - I_{xz}}$$

APPENDIX F

HOPKINSON BAR EXPERIMENT VIDEOS AND SIMULATION SOFTWARE

Following content for the Hopkinson Bar experiment videos and simulation files (MATLAB “.m” and Simulink block models “.slx”) and instructions to run the program can be found in the CD-1.

MATLAB & Simulink files were created under the licence number “40901578”.

1. Hopkinson Bar Experiment Videos

- (a) Experiment-1.avi
- (b) Experiment-2.avi
- (c) Experiment-3.avi
- (d) Experiment-4.avi
- (e) Experiment-5.avi
- (f) Experiment-6.avi
- (g) Readme.txt

2. MATLAB Simulink Files

- (a) Open Loop
 - i. Open Loop Model.slx
 - ii. Open Loop Model.m
- (b) Pole Placement
 - i. Pole placement model.slx
 - ii. Pole placement code.m

- (c) LQR Controller
 - i. LQR controller model.slx
 - ii. LQR controller code.m
- (d) Observer Model
 - i. Observer design state observer.slx
 - ii. Observer code.m
- (e) FlightGear
 - i. HL21
 - ii. runfg.bat
 - iii. Readme (FlightGear instructions).txt
- (f) Readme.txt

REFERENCES

- Agnello, A., J. Dosch, B. Metz, R. Sill, and P. Walter (2014, 02). Acceleration Sensing Technologies for Severe Mechanical Shock. *Sound & Vibration* 48, 8–19.
- Akgül, A., H. Y. Akargün, B. Atak, A. E. Çetiner, and O. Göker (2012). Numerical Investigation of NASA Tandem Control Missile and Experimental Comparison. *Scientific Technical Review* 62(1), 3–9.
- Albisser, M. (2015). *Identification of Aerodynamic Coefficients from Free Flight Data*. Ph. D. thesis, Université de Lorraine.
- ANSYS (2014). Lecture 7: Turbulence Modeling. Technical report.
- BAE Systems (2020). VULCANO [<https://www.baesystems.com/en/product/vulcano-precision-guided-munitions>]. Accessed on 2020-09-11.
- Beard, R. W. and T. W. McLain (2012). *Small Unmanned Aircraft: Theory and Practice*. Princeton university press.
- Bernhard, H. W., K. Legat, and M. Wieser (2003). *Navigation: Principles of Positioning and Guidance*. Springer.
- Brown, T. G., B. Davis, D. Hepner, J. Faust, C. Myers, P. Muller, T. Harkins, M. Hollis, C. Miller, and B. Placzankis (2001). Strap-Down Microelectromechanical (mems) Sensors for High-G Munition Applications. *IEEE Transactions on Magnetics* 21(2), 117–125.
- Bryson, J., J. D. Vasile, B. C. Gruenwald, and F. Fresconi (2020). Control Surface Design Analysis and Actuation Requirements Development for Munitions. In *AIAA Scitech 2020 Forum*, pp. 0020.
- Bryson, J. T. and F. E. Fresconi (2018a). Actuator Dynamics and Aeroelasticity for Canard Control on a Subsonic, Gun-Launched Munition. Technical report, US Army Research Laboratory Aberdeen Proving Ground United States.
- Bryson, J. T. and F. E. Fresconi (2018b). Low-Cost Actuator Dynamic Model and Controller Development for Gun-Launched Munitions. Technical report, US Army Research Laboratory Aberdeen Proving Ground United States.
- Burd, J. (1999). High-G Ruggedization Methods for Gun Projectile Electronics. In *Proceedings of the 12th International Technical Meeting of the Satellite Division of The Institute of Navigation (ION GPS 1999)*, pp. 1133–1142.
- Bureau of Naval Personnel (1966). *Principles of Guided Missiles and Nuclear Weapons*, 106

NAVPERS 10784-A. Washington, DC.

- Carlucci, D. E. and S. S. Jacobson (2018). *Ballistics: Theory and Design of Guns and Ammunition* (3rd ed. ed.). Boca Raton, FL: CRC Press.
- Chen, Y.-C., X.-B. Gao, M. Gao, and H.-M. Lv (2017). Aerodynamic Characteristic of a Canard Guided Rocket. *International Journal of Modeling, Simulation, and Scientific Computing* 8(01), 1750001.
- Cook, M. V. (2007). *Flight Dynamics Principles* (2nd ed. ed.). Burlington, MA: Butterworth Heinemann.
- Digby, J. F. (1974). Precision-Guided Munitions: Capabilities and Consequences. Technical report, RAND CORP SANTA MONICA CA.
- Dorf, R. C. and R. H. Bishop (2011). *Modern Control Systems*. Pearson.
- Dupuis, A. (2002, October). Aeroballistic Range and Wind Tunnel Tests of the Basic Finner Reference Projectile from Subsonic to High Supersonic Velocities. Technical Report 518050, Defence R&D Canada Valcartier.
- Dupuis, A. and W. Hathaway (1997, August). Aeroballistic Range Tests of the Basic Finner Reference Projectile at Supersonic Velocities. Technical Report 505377, Defence R&D Canada Valcartier.
- Edelkamp, S. and S. Schrödl (2012). *Heuristic Search: Theory and Applications* (1st ed. ed.). Waltham, MA: Morgan Kaufmann/Elsevier.
- ESA (2018, October). The Reference for Global Navigation Satellite Systems [https://gssc.esa.int/navipedia/index.php/main_page]. Accessed on 2020-20-10.
- Farrar, C. and D. Leeming (1983). *Military Ballistics* (1st ed. ed.). Oxford, England: Brassey's Publisher.
- Forrestal, M., T. Togami, W. Baker, and D. Frew (2003, 01). Performance Evaluation of Accelerometers Used for Penetration Experiments. *Experimental Mechanics* 43, 90–96.
- Foster, J., D. Frew, M. Forrestal, E. Nishida, and W. Chen (2011, 05). Shock Testing Accelerometers with a Hopkinson Pressure Bar. *International Journal of Impact Engineering* 46, 56–61.
- Frew, D. and H. Duong (2009, 01). A Modified Hopkinson Pressure Bar Experiment to Evaluate a Damped Piezoresistive MEMS Accelerometer. *Society for Experimental Mechanics - SEM Annual Conference and Exposition on Experimental and Applied Mechanics 2009* 3.

- Frieden, D. R. (1985). *Principles of Naval Weapon Systems* (1st ed. ed.). Annapolis, MD: Naval Institute Press.
- Garousi, V., M. Felderer, Çağrı Murat Karapıçak, and U. Yılmaz (2018). Testing Embedded Software: A Survey of the Literature. *Information and Software Technology* 104, 14–45.
- Google-Maps (2020, October). Strait of Bab-el Mandep [<https://www.google.com/maps/@13.731059,42.1332268,529218m/data=!3m1!1e3>]. Accessed on 2020-20-10.
- Gruenwald, B. C. and J. Bryson (2020). Adaptive Control for a Guided Projectile Using an Expanded Reference Model. In *AIAA Scitech 2020 Forum*, pp. 1822.
- Gruenwald, B. C., T. Yucelen, K. M. Dogan, and J. A. Muse (2018). An Adaptive Architecture for Control of Uncertain Dynamical Systems with Unknown Actuator Bandwidths. *IFAC-PapersOnLine* 51(12), 130–135.
- Gruenwald, B. C., T. Yucelen, K. M. Dogan, and J. A. Muse (2020). Expanded Reference Models for Adaptive Control of Uncertain Systems with Actuator Dynamics. *Journal of Guidance, Control, and Dynamics* 43(3), 475–489.
- Habibi, S., S. J. Cooper, J. Stauffer, and B. Dutoit (2008). Gun Hard Inertial Measurement Unit Based on MEMS Capacitive Accelerometer and Rate Sensor. In *2008 IEEE/ION Position, Location and Navigation Symposium*, pp. 232–237.
- Heffley, K., R. and F. Jewell, Wayne (1972, December). Aircraft Handling Qualities Data. Technical Report NASA CR-2144, National Aeronautics and Space Administration, Washington, DC.
- IAC (2021, May). GLONASS History [<https://www.glonass-iac.ru>]. Accessed on 2021-05-19.
- Inel, S. C. and S. Özdemir (2021). An Application of High-G Ruggedization Methods and PCB Survivability Testing Using Hopkinson Bar (to be published).
- IvenseNSE (2013). *MPU-6000 and MPU-6050 Product Specification* (Revision 3.4 ed.).
- Kahveci, M. and F. Yıldız (2017). *GPS/GNSS Uydularla Konum Belirleme Sistemleri*. Nobel.
- Krakiwsky, E. and D. Thomson (1974). Geodetic Position Computations. Lecture Notes, Department of Geodesy and Geomatics Engineering University of New Brunswick, Fredericton, N.B., Canada.
- LaGrone, S. (2016, October). USS Mason Fired 3 Missiles to Defend from Yemen Cruise Missiles Attack [<https://news.usni.org/2016/10/11/uss-mason-fired-3-missiles-to-defend-from-yemen-cruise-missiles-attack>]

missiles-to-defend-from-yemen-cruise-missiles-attack/]. Accessed on 2020-05-11.

Lall, P., K. Dornala, J. Deep, and R. Lowe (2017, 05). Effectiveness of Potting Methods and Underfills on the Enhancement of Survivability of Fine Pitch Electronics at 25,000g Shock Loads. In *16th IEEE ITERM Conference*, pp. 1262–1275.

Lall, P., K. Dornala, R. Lowe, and J. Foley (2016, May). Survivability Assessment of Electronics Subjected to Mechanical Shock Up to 25,000g. In *15th IEEE ITERM Conference*, pp. 507–518.

Lall, P., K. Dornala, J. Suhling, J. Deep, and R. Lowe (2019, May). Effect of Dielectric Material on the Reliability of 3640 MLCC Capacitors under High-G Shock Loads. In *18th IEEE ITERM Conference*, pp. 1037–1046.

Lall, P., K. Dornala, J. Suhling, R. Lowe, and J. Foley (2016, 05). Life Prediction and RUL Assessment of Fine Pitch Solder Joint Fuze Electronics Under Mechanical Shock Loads up to 50,000g. In *IEEE 66th Electronic Components and Technology Conference*, pp. 232–243.

Lall, P., K. Dornala, J. Wei, R. Lowe, and J. Foley (2015). Prognostication of Solder-Joint Reliability of 0.4mm and 0.5mm Pitch BGAs Subjected to Mechanical Shocks up to 10,000g. In *2015 IEEE Conference on Prognostics and Health Management (PHM)*, pp. 1–14.

Leonardo Company (2020). DART [https://www.leonardocompany.com/documents/20142/3150920/brochure_2016_oto+strales +-+oto+dart+ hq%28mm08726%29.pdf?t=1553002078948]. Accessed on 2020-09-11.

Lockheed Martin (2020). Copperhead Figure [<https://www.lockheedmartin.com/en-us/news/features/history/copperhead.html>]. Accessed on 2020-09-11.

MathWorks. Code Verification and Validation with PIL [<https://www.mathworks.com/help/supportpkg/arduino/ref/code-verification-and-validation-with-pil.html>]. Accessed on 2021-02-15.

MathWorks. Code Verification and Validation with PIL [<https://www.mathworks.com/help/supportpkg/arduino/ref/code-verification-and-validation-with-pil.html>]. Accessed on 2021-02-15.

MathWorks. Hydraulic Actuator Configured for HIL Testing [<https://www.mathworks.com/help/physmod/simscape/ug/hydraulic-actuator-configured-for-hil-testing.html>]. Accessed on 2021-02-15.

MathWorks. SIL and PIL Simulations [https://www.mathworks.com/help/encoder/ug/about-sil-and-pil-simulations.html?s_tid=srchtitle]. Accessed on 2021-02-15.

MathWorks. SIL Verification for a Subsystem [<https://www.mathworks.com/help/sltest/ug/silpl-verification-for-a-subsystem.html>]. Accessed on 2021-02-15.

MathWorks. What is Hardware-In-The-Loop Simulation? [<https://www.mathworks.com/help/physmod/simscape/ug/what-is-hardware-in-the-loop-simulation.html>]. Accessed on 2021-02-15.

Matthew, P. Lecture Notes in Spacecraft and Aircraft Dynamics, Lecture 9: 6-DOF Equations of Motion [<http://control.asu.edu/classes/mmae441/aircraft/441lecture9.pdf>]. Accessed on 2021-02-24.

McCoy, R. L. (2009). *Modern Exterior Ballistics: The Launch and Flight Dynamics of Symmetric Projectiles* (2nd ed. ed.). Atglen, PA: Schiffer Publishing.

Mönch Publishing Group (2021). Northrop Grumman Details Precision Guidance Kit [<https://www.monch.com/mpg/news/land/5238-ng-precision-guidance-kit.html>]. Accessed on 2021-02-20.

Morrison, P. H. and D. S. Amberntson (1977). Guidance and Control of a Cannon-Launched Guided Projectile. *Journal of Spacecraft and Rockets* 14(6), 328–334.

Mracek, C. and D. Ridgely (2005). Missile Longitudinal Autopilots: Connections Between Optimal control and Classical Topologies. In *AIAA guidance, navigation, and control conference and exhibit*, pp. 6381.

Naval Sea Systems Command Office of Corporate Communication (2019, January). Evolved Seasparrow Missile Block 1 ESSM RIM 162D [<https://www.navy.mil/resources/fact-files/display-factfiles/article/2168978/evolved-seasparrow-missile-block-1-essm-rim-162d/>]. Accessed on 2020-09-11.

Nelson, R. C. (1998). *Flight Stability and Automatic Control* (2nd ed. ed.). Singapore: McGraw-Hill.

Nise, N. S. (2020). *Control Systems Engineering*. John Wiley & Sons.

NOAA (2021, May). The Global Positioning System [<https://www.gps.gov/systems/gps/>]. Accessed on 2021-05-19.

Ogata, K. (2010). *Modern Control Engineering*. Prentice hall.

Sheard, K., I. Scaysbrook, and D. Cox (2008). MEMS Sensor and Integrated Navigation Technology for Precision Guidance. In *Location and Navigation Symposium 2008 IEEE/ION Position*, pp. 1145–1151.

Shi, Y., Z. Zhu, P. Li, and W. Liu (2010, 01). The Packaging Effect on High g Accelerometer Test. *2010 IEEE 5th International Conference on Nano/Micro Engineered and*

Molecular Systems, NEMS 2010..

- STMicroelectronics (2003). *Understanding and Minimising ADC Conversion Errors, AN1636* (Revision 1.5 ed.).
- STMicroelectronics (2016). *STM32F427xx and STM32F429xx Datasheet* (Revision 9 ed.).
- STMicroelectronics (2017). *STM32F405/415, STM32F407/417, STM32F427/437 and STM32F429/439 Advanced ARM®-based 32-bit MCUs, Reference Manual RM0090* (Revision 17 ed.).
- STMicroelectronics (2020). *How to Get the Best ADC Accuracy in STM32 Microcontrollers, Application Note AN2834* (Revision 5 ed.).
- STMicroelectronics (2021). *STM32L052x6, STM32L052x6, Datasheet* (Revision 10 ed.).
- Teper, G. L. (1969). Aircraft Stability and Control Data. Technical Report NASA CR-96008, National Aeronautics and Space Administration, Springfield, VA.
- Thai, S., S. Theodoulis, C. Roos, and J.-M. Biannic (2019). Robust Design for the Roll-channel Autopilot of a Canard-Guided Dual-Spin projectile. *IFAC-PapersOnLine* 52(12), 232–237.
- Theodoulis, S. and P. Wernert (2017). Flight Dynamics & Control for Smart Munition: The ISL Contribution. In *IFAC-PapersOnLine*, Volume 50, pp. 15512–15517.
- Thomas, S., L. Stephen, S. David, R., and M. Juan, Carlos (2002). Database for Solder Properties with Emphasis on New Lead-free Solders. Technical report, National Institute of Standards and Technology and Colorado School of Mines.
- Tsourdos, A. and B. White (2005, 03). Adaptive Flight Control Design for Nonlinear Missile. *Control Engineering Practice - CONTROL ENG PRACTICE* 13, 373–382.
- Tuna, M., S. C. İnel, and S. Özdemir (2020). Longitudinal Stability Analysis of Aircrafts. *The Journal of Scientific and Engineering Research* 7(10), 45–51.
- Versteeg, H. K. and W. Malalasekera (2007). *An Introduction to Computational Fluid Dynamics: The Finite Volume Method*. Pearson education.
- Vishay (2019). *Metal Film Resistors, Axial, High Precision, High Stability*.
- Wells, L. L. (2000). The Projectile GRAM SAASM for ERGM and Excalibur. In *IEEE Position Location and Navigation Symposium*, pp. 106–111.

Xu, Q., S. Chang, and Z. Wang (2018). Acceleration Autopilot Design for Gliding Guided Projectiles with Less Measurement information. *Aerospace Science and Technology* 77, 256–264.

Yunus, e. and C. John (2010). *Fluid Mechanics: Fundamentals And Applications*. (3rd ed.). McGraw Hill.

Zarchan, P. (2012). *Tactical and Strategic Missile Guidance*. American Institute of Aeronautics and Astronautics, Inc.

Zipfel, P. H. (2007). *Modeling and Simulation of Aerospace Vehicle Dynamics* (2nd ed. ed.). American Institute of Aeronautics and Astronautics.